NGI Rapport / Report

SP2 - Damping properties of soil

Estimation of hysteretic soil damping from laboratory measurements including strain accumulation

20110087-01-R
12 May 2014
Revision: 0

Main office:
PO Box 3930 Ullevål Stadion
NO-0806 Oslo
Norway

Trondheim office:
PO Box 1230 Pirsenteret
NO-7462 Trondheim
Norway

T (+47) 22 02 30 00
F (+47) 22 23 04 48

BIC No. DNBANOKK
IBAN NO26 5096 0501 281
Company No.
958 254 318 MVA

ngi@ngi.no
www.ngi.no

Project

Project:	SP2 - Damping properties of soil
Document No.:	20110087-01-R
Document title:	Estimation of hysteretic soil damping from laboratory measurements including strain accumulation
Date:	12 May 2014
Revision:	0

Client

Client:	Norges forskningsråd
Client's contact person:	
Contract reference:	GBV - SP2 (Offshore wind turbines) 250 kNOK

For NGI

Project manager:	Finn Løvholt
Prepared by:	Finn Løvholt, Jörgen Johansson
Reviewed by:	Christian Madshus

Summary

The periodic forces due to wind, surface waves and swells on offshore installations such as offshore wind turbines lead to cyclic motion of the soil foundation. The damping properties of soils account for a part of the energy dissipation of the Offshore Wind Turbine (OWT) system. Understanding damping is therefore important with respect to the structural response and the cost-effective design of structures. Unfortunately, OWT foundation damping is sparsely studied, and the understanding of this parameter is therefore limited. The present results provide a step forwards towards a better understanding and interpretation of stiffness and damping parameters of soils, and focuses on basic concepts and on the effect of permanent strain accumulation in particular. Analyses of laboratory data have shown that the interpreted hysteretic soil damping becomes too large unless the permanent strain accumulation is filtered out. On the other hand, the strain

BS EN ISO 9001
Certified by BSI
Reg. No. FS 32989

accumulation contributes to hysteretic loss in addition to the material damping. The current study is a first step towards a better understanding and interpretation of damping parameters for soils, and focuses on basic concepts. A crucial next step would include methods for interpreting the damping correctly in models soil-structure interaction for realistic loads and structures, to clarify the importance of soil damping for offshore wind turbine foundations. Due to the industry's need for simple and efficient models used for large scale, it is essential that the damping formulation is kept simple.

Contents

1 Introduction

The periodic forces due to wind, surface waves and swells on offshore installations such as offshore wind turbines lead to cyclic motion of the soil foundation. The damping properties of soils account for energy dissipation. Understanding damping is therefore important with respect to the structural response and the cost-effective design of such structures. Unfortunately, offshore wind turbine foundation damping is sparsely studied, and the understanding of this parameter is therefore somewhat limited. The current study is a first step towards a better understanding and interpretation of damping parameters for soils and focuses on basic concepts. There exist also various damping parameters defined in different ways, which may be confusing to engineers and practitioners in soil science. This report reviews some basic aspects with respect to soil damping, and provides some correction to existing methods for estimating damping parameters from processing of laboratory data.

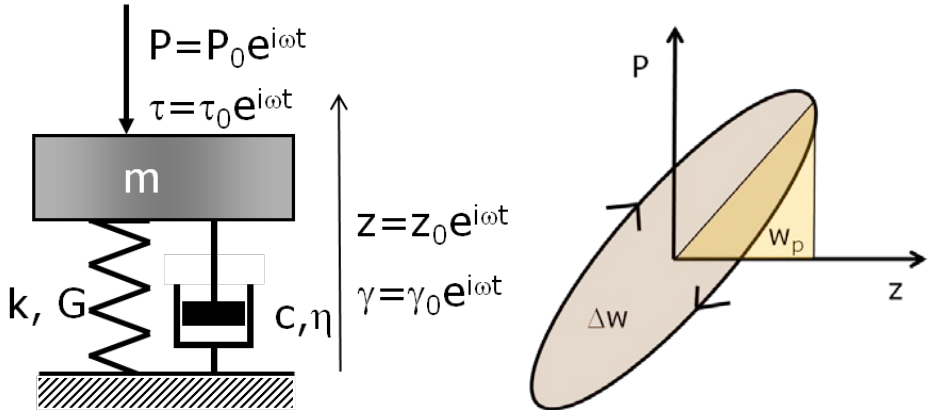

Figure 1.1 *Left panel: Sketch of a single degree of freedom spring-dashpot system subject to periodic loading (both force and stress). Right panel: Definition sketch showing the interpretation of potential energy and energy loss in a hysteretic loop.*

1.1 Basic definitions

Here, we review some basic properties soil damping. It is noted that a more detailed mathematical description of derivations etc is found in Appendix A. The damping parameters includes the hysteretic **loss factor** denoted η, the **damping factor** *D* which is simply the half of the loss factor, and the **quality factor** *Q* which it's inverse. Formally, the loss factor is proportional to the ratio of the energy dissipation pr. cycle Δw divided by the maximum potential energy w_p, in the same cycle

$$\eta = 2D = \frac{1}{Q} = \frac{1}{2\pi}\frac{\Delta w}{w_p}. \qquad \textit{(Eq.1.1)}$$

A sketch showing the interpretation of the energy loss and potential energy in a stress-strain loop is depicted in the right panel of Figure 1.1. The energy loss Δw is

interpreted as the area under the load displacement curve, whereas the potential energy w_p is the area under the triangle. We may also interpret the loss factor as the imaginary part of a complex modulus, as here exemplified for the shear modulus *G'* i.e.

$$G' = G(1 + i\eta) \qquad \textit{(Eq.1.2)}$$

Here, *G* is the shear modulus of the soil. For a single degree of freedom spring dashpot system (Figure 1.1), the loss factor relates to the viscous damping constant *c* at a given angular frequency ω = 2πf (where f is the frequency) for a spring-dashpot system according to:

$$\eta = \frac{c\omega}{G} \qquad \textit{(Eq.1.3)}$$

Next, we denote the natural frequency ω_n, the critical damping constant c_{cr} and the **fraction of critical damping** ξ as:

$$\omega_n = \sqrt{\frac{k}{m}}, \quad c_{cr} = 2\sqrt{k \cdot m}, \quad \xi = \frac{c}{c_{cr}} \qquad \textit{(Eq.1.4)}$$

It may be shown that the loss factor equals twice the degree of critical damping at the natural frequency, i.e.

$$\eta = 2(\frac{\omega}{\omega_n})\xi \qquad \textit{(Eq.1.5)}$$

It is noted that the concept of **Rayleigh damping** C_R is frequently encountered in dynamic structural analysis. It consists of a mass matrix term associated with a parameter α and a stiffness matrix term associated with a parameter β. The frequency dependence of the Rayleigh damping usually makes it inconvenient for soils.

1.2 Examples of damping dependence of soil parameters from the literature

Soil damping depends on various parameters such as the cyclic strain amplitude, and is therefore an inherently non-linear property of the soil. At small loads, the cyclic strains in the ground are very low and in a range where ground materials have a nearly ideal linear elastic behaviour. However, even at these small strains the materials have a small amount of internal loss. Towards higher strains, ground materials exert an increasing hysteretic non-linear behaviour, which leads to additional hysteretic loss. The lower left panel in Figure 1.2 (Menq, 2003) plots the hysteretic damping factor versus the cyclic strain level divided into three strain level regimes. For completeness, the reduction of the normalized stiffness G/G_{max} is also depicted in the upper panels. This curve also turns out to fit reasonably well for all granular, non-cohesive and even low plasticity cohesive materials, non-degraded as well as degraded. For more plastic cohesive soils (clays), the degree of plasticity turns out to have an effect on the shear modulus and the damping factor versus the cyclic shear strain. The right panels of Figure 1.2 (Vucetic and Dobry, 1988) plots

the normalized shear modulus and damping curves for cohesive soils like clay with different plasticity indexes. The curves for I_p=0 are identical to those for non-cohesive soil materials. For plastic clays also the threshold strains and thus the cyclic behaviour regions depend on the plasticity index.

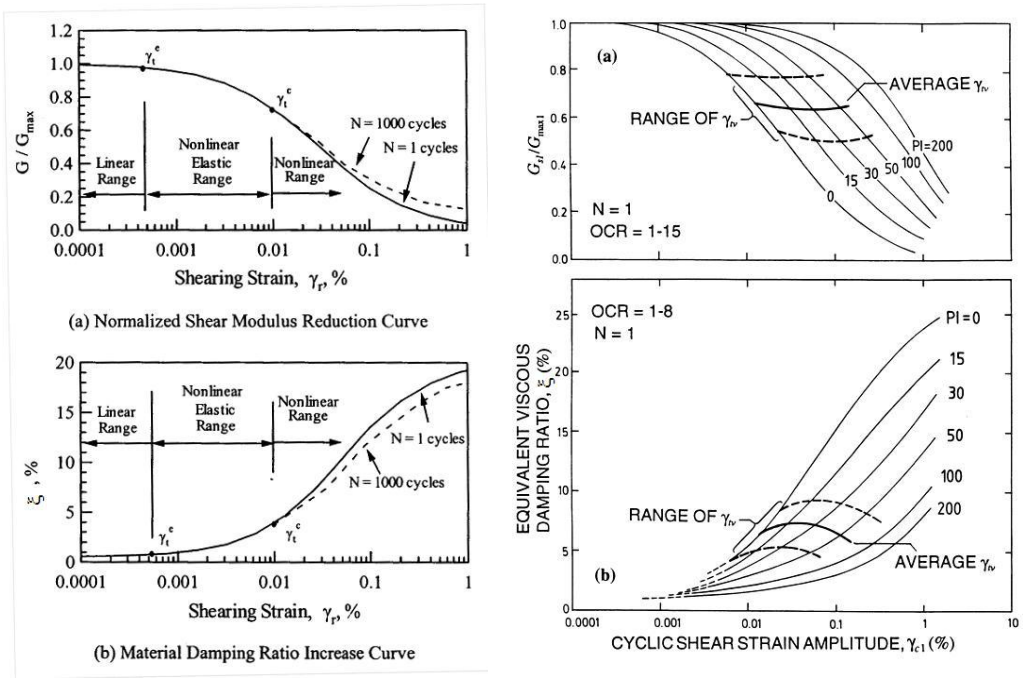

Figure 1.2 *Left panels; Typical non-linear modulus reduction and damping variation curves for cohesionless soil materials (Menq, 2003). Right panels; Typical non-linear modulus reduction and damping variation curves for undrained plastic soils - versus plasticity index (Vucetic and Dobry, 1988).*

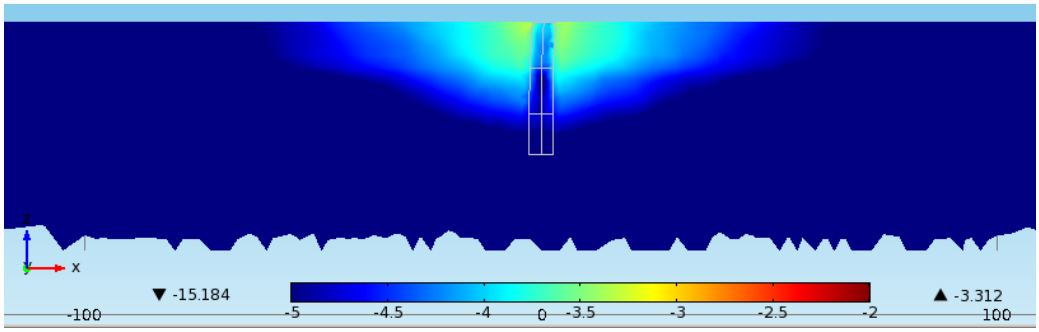

Figure 1.3 *Example of a spatial variability of the displacement field for a monopile foundation subject to cyclic loading*

1.3 Interpretation of soil damping in practical applications

OWTs are lightly damped structures often with fatigue governing the design. Therefore a thorough understanding of different damping sources, such as aerodynamic, hydrodynamic, structural, and foundation is essential for a cost

effective design. Foundation stiffness and damping depends not only of the soil properties but also foundation geometry, load intensity and frequency. As the damping is load dependent, the problem becomes non-linear and must be evaluated using realistic soil models in numerical models where the strain varies over the foundation (see Figure 1.3). The foundation nonlinearity gives a contribution to global damping in addition to tower oscillation dampers. Above a certain cut-off frequency, the tower oscillation may set up surface waves in the ground that propagate radially, which is defined as the radial foundation damping. For OWTs, the cut-off frequency is generally higher than the fundamental mode and the governing load frequencies. The radial damping does therefore not contribute much to the global dynamic response of OWTs. However, the material soil damping as well as the effect of added mass do affect the overall response, which may be utilized in OWT design. Example of an integration of a global soil damping using Finite Elements is found in Appendix C. Evaluation of sensitivity studies of the global structural response of a monopile subject to different damping factors are given in Appendix D. Based on the method outlined in Appendix D, we have calculated time histories of the mudline moment in from an extreme storm load. Figure 1.4 show that the monopile foundation damping due to such extreme loads under parked conditions differ considerably from the case of an undamped foundation.

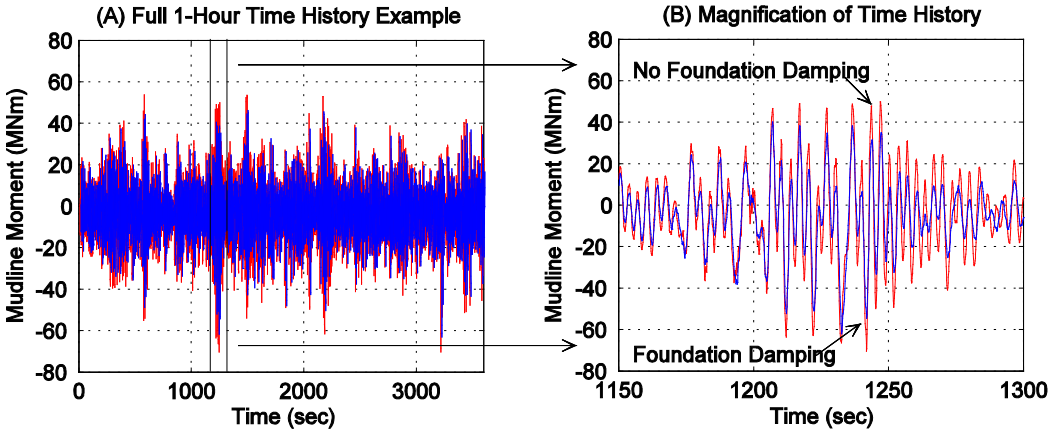

Figure 1.4 *Example of a mudline moment time history for a monopole foundation due to a stochastic storm load (from Carswell et al., manuscript in final preparation). Cases with and without foundation damping are compared.*

2 A new method for interpreting soil damping from laboratory data

Previous methodology for interpreting the damping from laboratory data does not currently take into account permanent strain accumulation. However, it is desirable to account for strain accumulation as tests combining cyclic and static loads are commonly applied. Therefore, we have developed an improved method that correct for the strain accumulation. In the present examples, all tests are stress controlled.

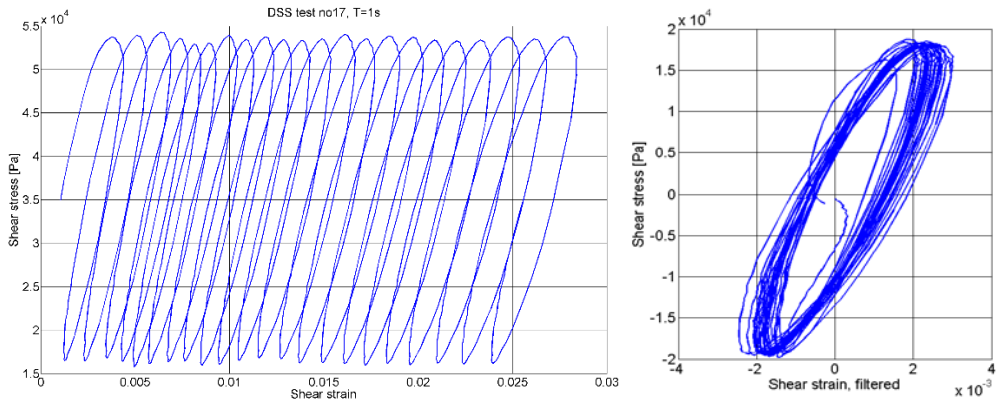

Figure 2.1 *An example of a stress-strain path for a DSS test superimposing static and cyclic stress. Left panel, cyclic behaviour showing both the cyclic and the permanent accumulated strain. Right panel, filtered stress-strain loops (the permanent stress term is removed here).*

- Each cycle is identified through a zero crossing method. This takes the stress or strain time series and finds every instance of a zero crossing, by first subtracting the mean value (an example of a cyclic stress strain curve with strain accumulation is given Figure 2.1). In this procedure, care is taken to avoid artificial crossings due to noisy data. A cycle is defined as the period between each up crossing or down crossing.
- Strain accumulation terms are filtered from the stress and strain histories. We apply a polynomial curve fit for the accumulation, and then subtract the fitted function. An example of the stress-strain relations before and after filtering is shown in Figure 2.1.
- For each individual filtered cycle, the energy loss is computed by integrating the cyclic components, $\Delta w = \oint \tau_c d\gamma_c = \int_0^T \tau_c \, (d\gamma_c/dt)\, dt$, where the subscript c accounts for the periodic (cyclic) component. The maximum potential energy may either be computed by the expression $w_p = 1/2 \cdot G \cdot \gamma_{max}^2$. Here, we use two different definitions for the shear stiffness G (see Figure 2.2 for a definition). An approximate value of $G_1 = \tau_{max}/\gamma_{max}$ which is most practically convenient to extract from lab-data, and the theoretically correct $G_2 = \tau(\gamma_{max})/\gamma_{max}$. These yield the following expressions for the potential energy, $w_{p2} = 1/2 \cdot \gamma_{max} \cdot \tau_{max}$ and $w_{p2} = 1/2 \cdot \gamma_{max} \cdot \tau(\gamma_{max})$.
- The time dependent loss and damping factors are found by inserting the expressions for the energy loss Δw and potential energy w_p in the expression above for every cycle.

The damping may also be interpreted as the phase $\varphi_{\gamma\tau}$ between the stress and strain histories. A measure of the phase may be found in the frequency domain by means of a Fast Fourier Transform (FFT). The FFT provides a more stable measure of the damping, as the effects of fluctuations from the time series in the measurements are

automatically smoothed in this method. This alternative method was implemented in the frequency domain. In this method, we extract the stress and strain time histories from each cycle. We also including tapered signals one cycle ahead and after the cycle in question using a cosine square function. In the frequency domain, the phase between the stress and strain is extracted at the load frequency to provide a direct measure of the loss factor, i.e. $\eta=\varphi_{\gamma\tau}$.

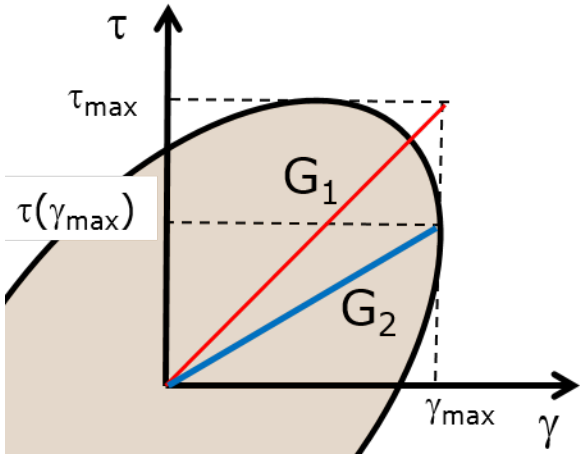

Figure 2.2 *The two different definitions of the stiffness used in the damping calculations for an ideal stress-strain cycle. G_1 is defined by the ratio of the peak stress and strain, whereas G_2 is defined using the stress value at the maximum strain. The width of the loop is exaggerated to demonstrate the difference in the definitions.*

Below we compare each of the three methods for estimating damping from the laboratory tests.

2.1 Interpretation of damping factors from laboratory measurements

In the following, we provide some examples of damping interpretation using the improved algorithm that corrects for permanent strain accumulation. A more detailed set of cyclic stress-strain curves with related damping factors are found in Appendix B.

The results are compared to an existing method that does not take this effect into account. Data examples are taken from Direct Simple Shear (DSS) tests on clay (NGI, 2008), and the damping factor *D* is interpreted from shear stress and shear strain histories obtained from the test. The tests consist of pure cyclic shear loading with pure cyclic strain (e.g. Figure 2.3), as well as superimposed static and cyclic loads resulting in both cyclic and accumulated strain (e.g. Figure 2.4 and Figure 2.5). As shown by comparing the damping values for the various methods, the old and new method provide more or less identical results when there is no strain accumulation (Figure 2.3). For small strains deviations are hardly visible. We see that by using the approximate expression for the stiffness (blue circles) a slightly

too low damping is obtained compared to the damping obtained from using the correct stiffness (blue crosses) at large strain. However, this error is by no means dramatic. Furthermore, we see that the frequency-phase method provide the lowest damping estimates, but still with small deviations from the other methods.

When the strain accumulation is introduced, the new methods result in lower damping values than the old method (Figure 2.4), meaning that an artificially high damping is reported when not correcting for the strain accumulation (displayed by the red markers). This artificial effect becomes more prominent when the strain accumulation is large, as exemplified in Figure 2.5. Here we see that the reported damping factor is twice as high as it should be when not correcting for the strain accumulation. The relative importance of the strain accumulation may also be interpreted visually, i.e. it is important when the stress-strain cycles are clearly distinguishable and far from being closed. The latter observation is found for instance by comparing the stress-strain relations and corresponding damping factors in Figure 2.4 and Figure 2.5. All the three new methods taking into account the strain accumulation provide quite coherent results. The most stable measure of these three is clearly the frequency domain method. As for the pure cyclic tests discussed above, the results using the two time-domain methods yield only small errors in the damping for using the approximate expression for the stiffness.

Figure 2.6 shows a comparison of the damping curves as a function of the maximum cyclic strain during a load cycle for clay and sand respectively. It is noted however, that the sand sample is loaded purely cyclic, whereas the clay test is unsymmetric with a stress offset. Keeping this in mind, we see that the damping is diametrically opposite at high strains. Whereas the damping increases with strain for the clay sample, the damping is decreasing as a function of the strain for the sand sample. The damping behavior for the sand sample at high strain is most likely related to the increased stiffness that occur during dilatation. This is observed for the single stress strain loops. At small cyclic strain, the stress-strain loop is more elliptic. At high strain, the stress-strain loop loses the ellipticity and have large tangential stiffnesses near the peak strain. At the same time, the area under the stress strain loop is reduced compared to the maximum potential strain energy, leading to reduced damping.

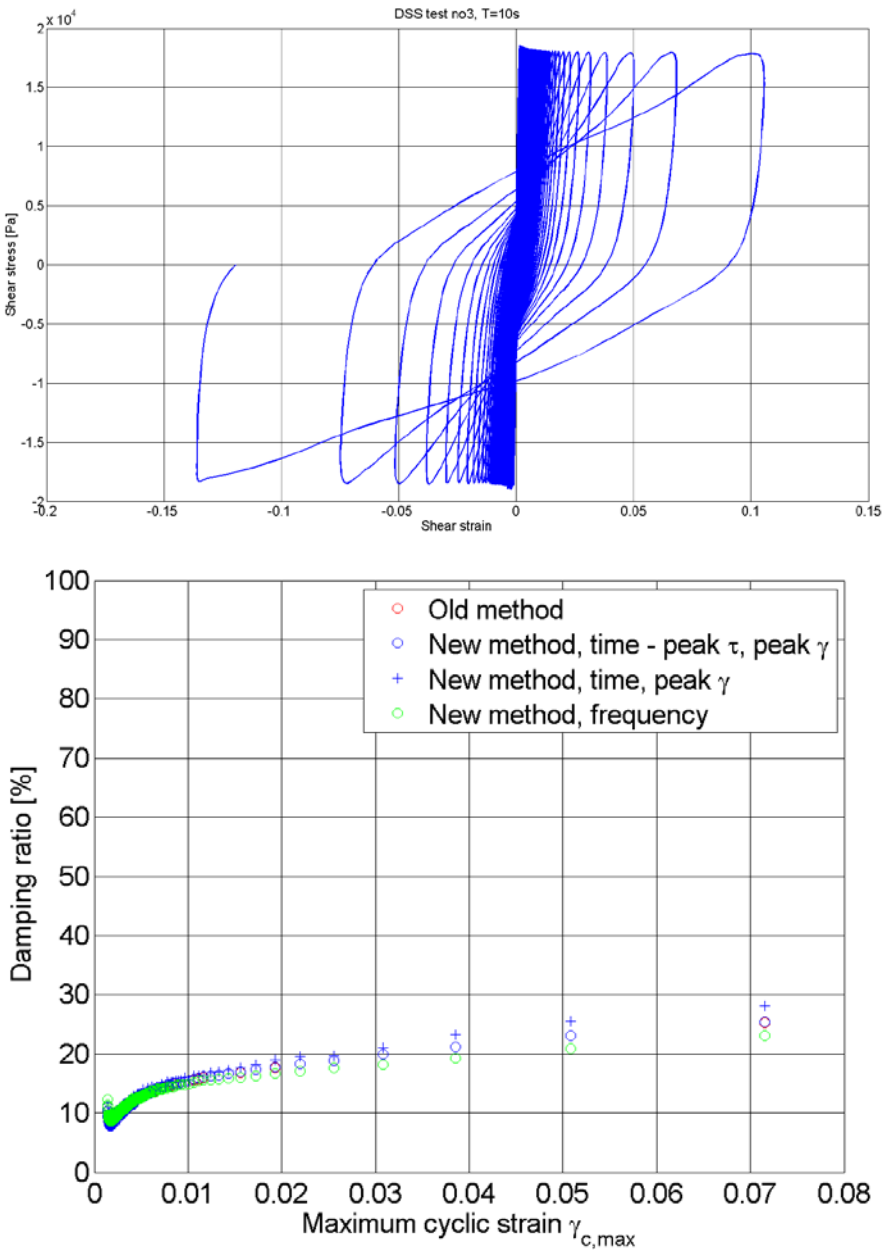

Figure 2.3 *DSS test with pure cyclic loading for a load period 10s. Upper panel, stress-strain curves for all cycles. Lower panel, damping factors as functions of the maximum cyclic strain. Red markers refer to the old method where strain accumulation is not accounted for, blue markers to the new method in the time domain (using two different stiffness definitions), and green markers correspond to the frequency domain approach.*

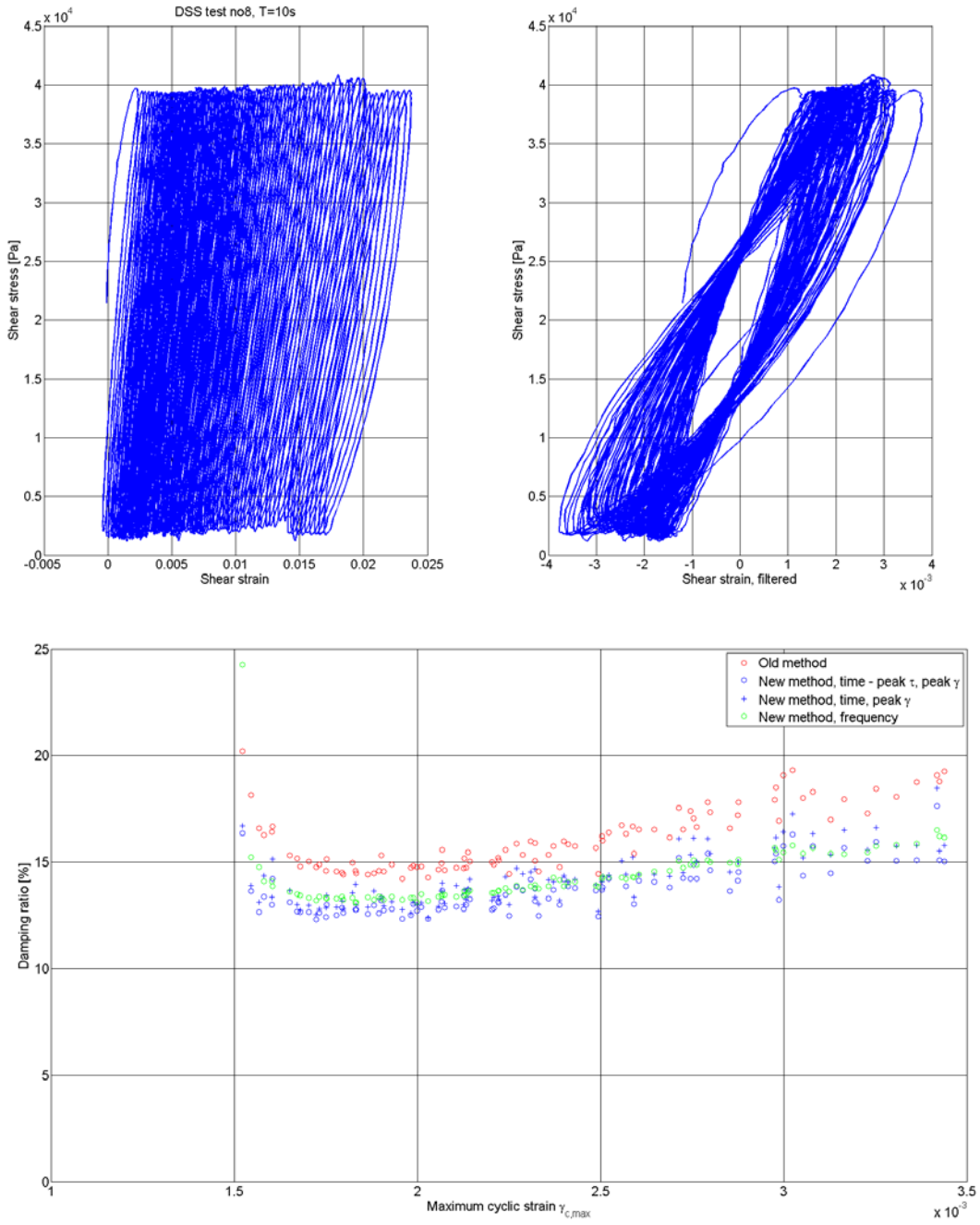

Figure 2.4 *DSS test with a constant shear stress of τ_c=20.9kPa, and a load period 10s. Upper panel, stress-strain curves for last 10 cycles. Lower panel, damping factors as functions of the maximum cyclic strain. Red markers refer to the old method where strain accumulation is not accounted for, blue markers to the new method in the time domain (using two different stiffness definitions), and green markers correspond to the frequency domain approach.*

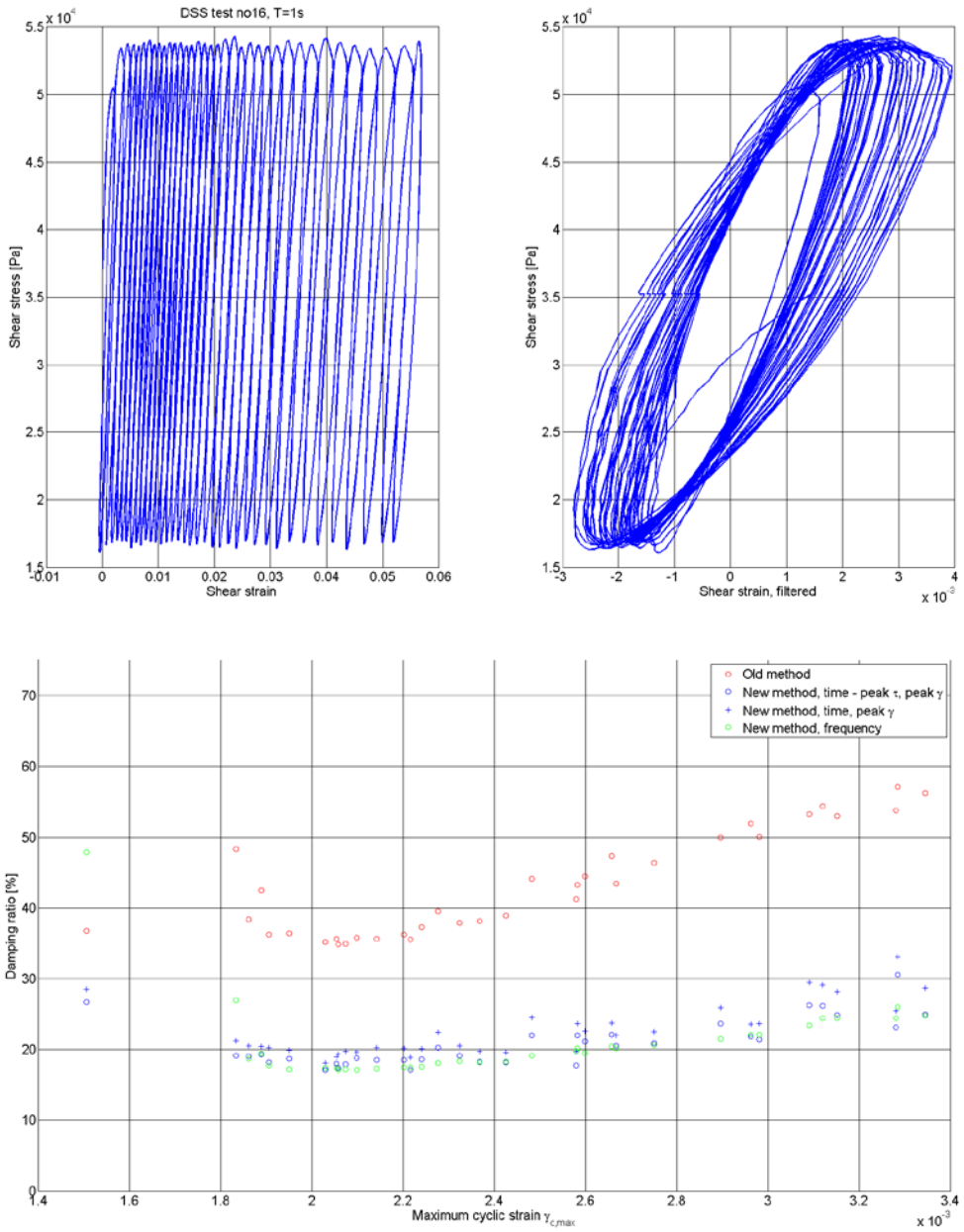

Figure 2.5 *DSS test with a constant shear stress of τ_c=35.7 kPa, and a load period 1s. Upper panel, stress-strain curves for last 10 cycles. Lower panel, damping factors as functions of the maximum cyclic strain. Red markers refer to the old method where strain accumulation is not accounted for, blue markers to the new method in the time domain (using two different stiffness definitions), and green markers correspond to the frequency domain approach.*

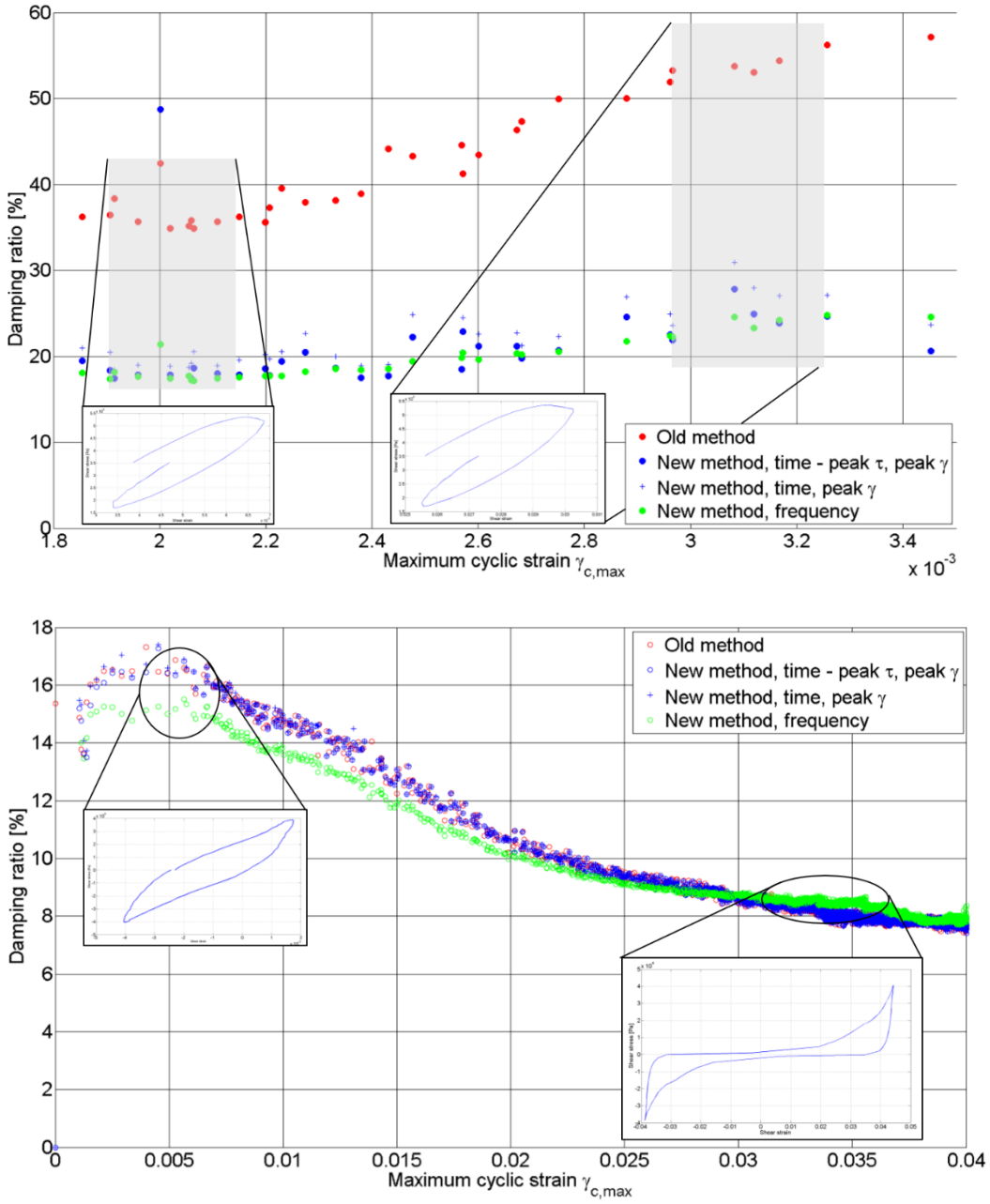

Figure 2.6 *Upper panel, damping ratios and examples of cyclic curves for a clay sample. Lower panel, damping ratios and examples of cyclic curves for a sand sample. The insets show examples of single load cycles at a given strain level.*

3 Analytical correction for strain accumulation in the damping term

In this section, we analyse the correction factors for the damping or loss factors obtained from integration of cyclic stress-strain loops due to strain accumulation. In Appendix A we derive a simple model capturing the basic physics of a soil

subject to both cyclic and permanent strain accumulation. Here, we demonstrate that despite its simplicity, the model follows the measured load cycle closely.

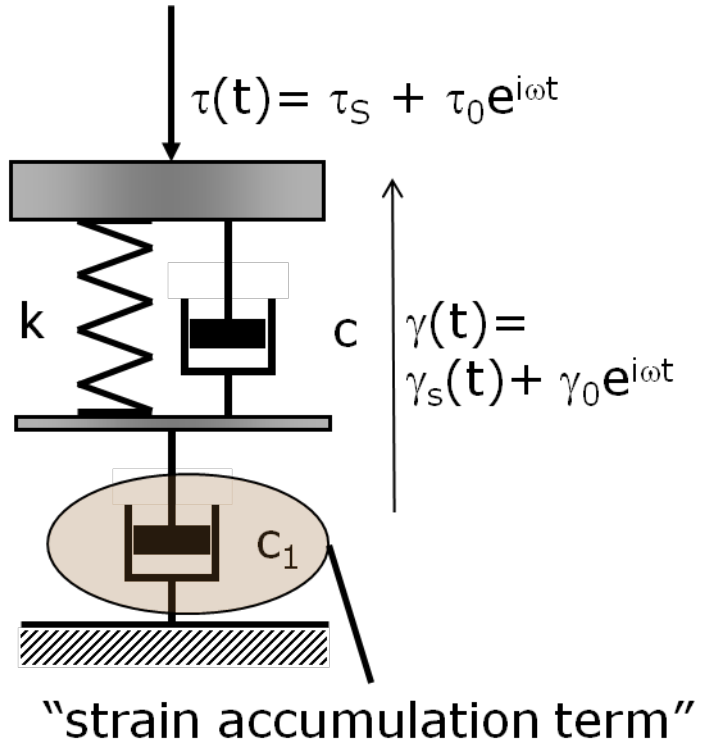

Figure 3.1 *Sketch of a single degree of a mass-spring-dashpot coupled to a single damper and system subject to periodic loading. The subscripts "s" represents static load and displacement terms.*

Figure 3.1 shows a sketch of the simple soil model, that is, a damped single degree of freedom system attached to an additional damping component. An external force composed of a static and a harmonic load component is acting on the system. This coupled spring-damper system represents a more realistic, yet simplified representation of the soil behaviour with strain accumulation obtained from laboratory measurements. The additional damping term labelled c_1 represents the permanent strain accumulation. As shown in Appendix A, we obtain the following (corrected) loss factor for this system:

$$\eta = \frac{k_{I1}^2}{1+k_{\Sigma}^2}\psi, \qquad \textit{(Eq.3.1)}$$

Where the following help factors are defined as:

$$\psi = \frac{1+k_I}{k_{I1}} + k_I, \;\; k_I = \frac{c\omega}{G}, \;\; k_{I1} = \frac{c_1\omega}{G}, k_{\Sigma} = k_{I1} + k_I \qquad \textit{(Eq.3.2)}$$

The original expression for the loss factor *without* strain accumulation reads

$$\eta = k_I = \frac{c\omega}{G} \qquad (Eq.3.3)$$

Correction due to **strain accumulation is contained in the k_{I1} term**, which **again enters the ψ and k_Σ terms**. A large value c_1 (and consequently k_{I1}) is interpreted as large resistance to strain accumulation and close to pure cyclic behavior. For large values of k_{I1} the strain accumulation becomes negligible and Equation 3.2 is retained. Comparing Equation 1.5 and 3.2, it is possible to deduce that the strain accumulation increases the loss and damping factors. I.e. the correction terms introduced (k_{I1}, ψ, and k_Σ) adds to the viscous terms. Generally, the permanent strain accumulation becomes large (and important) when c_1 and correspondingly k_{I1} are small. Correspondingly, the terms become negligible when large. As demonstrated below, the effect becomes noticeable for say $c_1/c < 1000$, and is clearly important for $c_1/c < 100$.

Figure 3.2 shows an example of a stress strain curve simulated using the simple system proposed in Figure 3.1 (details of the governing equations for strain and stress are given in Appendix A). We insert the cyclic and constant stress components $\tau_0 = 18.7$ kPa and $\tau_s = 20.8$, and find the following best fit parameters for the damping and stiffness by visual inspection; G=11.56 MPa; $c = 4.6 \cdot 10^6$; $c_1 = 250 \cdot c$, providing a loss factor of 0.27. As shown in Figure 3.2, we obtain a fairly good agreement between the model and the laboratory tests by comparing the results. An even better agreement may be obtained by fine tuning the stiffness and damping parameters more. However, the present fit is sufficient for the demonstration purpose which is the aim of the present computation.

Figure 3.3 shows two different simulations with the same load situation and stiffness as above, but for two different strain accumulation rates, i.e. $c_1/c = 250$ and $c_1/c = 50$. We see that for relatively large ratios c_1/c (small strain accumulation), the correction (relative error) due to strain accumulation is about 3% of the total damping value and almost negligible. In the case of smaller ratios c_1/c (large strain accumulation) however, the correction (relative error) due to the strain accumulation is more than a fraction of 30% of the total damping value which certainly needs to be accounted for in interpretation of laboratory measurements.

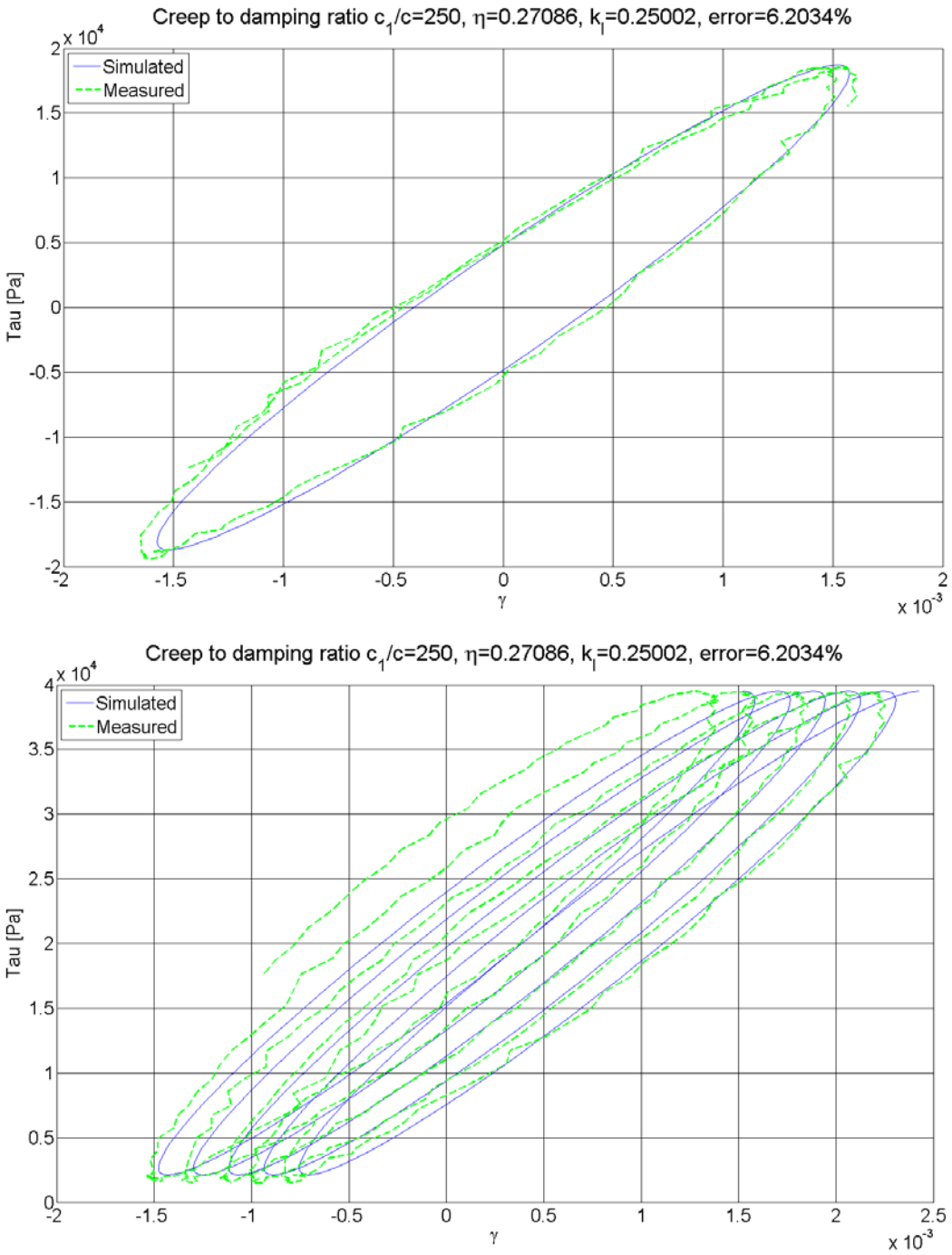

Figure 3.2 *Comparison between laboratory measurement and a simulated stress strain curve. Upper panel, single cycle with the strain accumulation is filtered out. Lower panel, five cycles with permanent strain accumulation retained. The errors given in the figure headers are relative.*

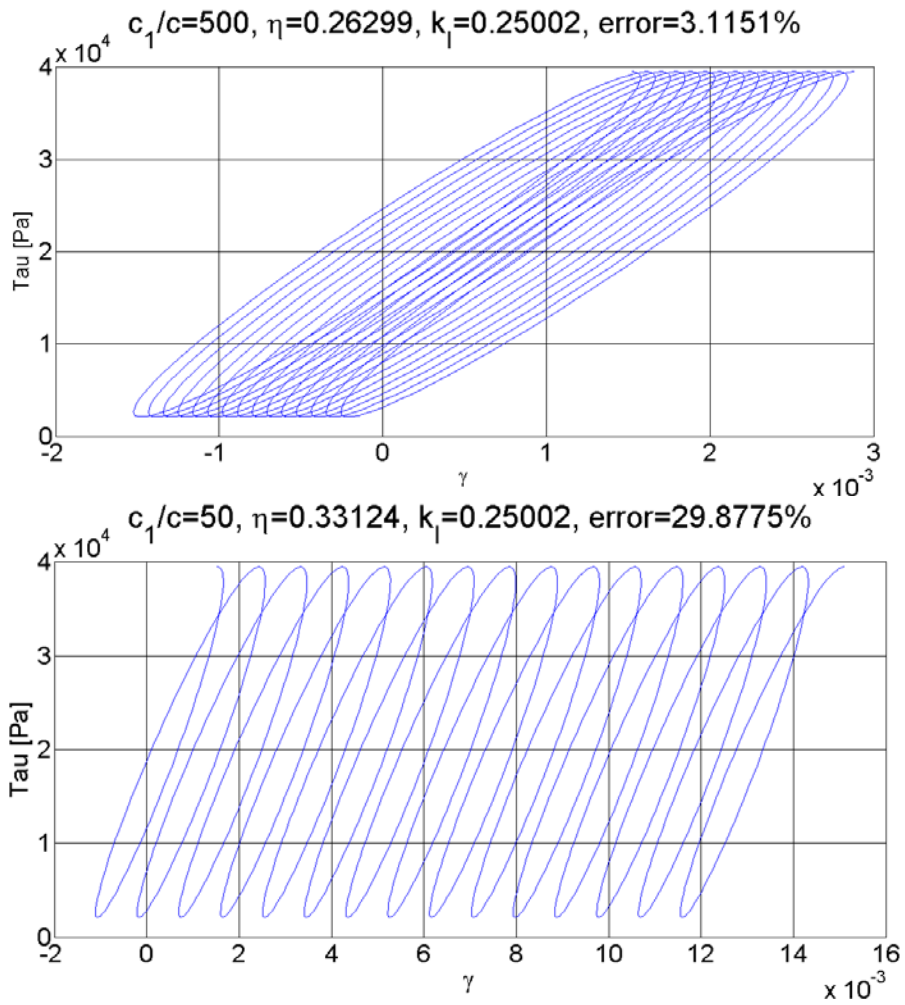

Figure 3.3 *Example of the error in damping for two synthetic stress strain loops. Upper panel, c_1/c = 500, lower panel c_1/c = 50. Both examples are may represent realistic ranges in terms of strain accumulation to cyclic strain ratios. The errors given in the figure headers are relative.*

4 Final remarks

Analyses of laboratory data have shown that the interpreted hysteretic soil damping becomes too large unless the permanent strain accumulation is filtered out. On the other hand, the strain accumulation contributes to hysteretic loss in addition to the material damping. The effect of strain accumulation should be accounted for at least for high strains. In practice, this effect becomes important when the stress-strain loops are clearly not closed in experiments with combined static and cyclic loads. A pure filtering of the strain accumulation from the strain history leads to a reduced damping. However, the strain accumulation accounts for some of the hysteretic damping, and this effect gives a counterbalance.

In this report, three different methods for processing laboratory data for estimating the damping is established, tested, and compared to a previous method that did not take into account the strain accumulation. A new method is necessary in order to provide correct damping estimates. The three new methods (two time domain methods and a frequency domain method) all provide relatively coherent results. The frequency domain method provided the most stable results, and should if feasible be implemented in new laboratory routines. The simplest alternative is to use the time domain method based on the peak-to-peak stiffness.

The current study is a first step towards a better understanding and interpretation of damping parameters for soils and focuses on basic concepts. A crucial next step would include methods for interpreting the damping correctly in models soil-structure interaction for realistic loads and structures, to clarify the importance of soil damping for windmill foundations. To this end, the examples in Appendices C and D provides a good starting point. Due to the industry's need for simple and efficient models used for large scale, it is essential that the damping formulation is kept simple.

5 References

Carswell, W., Johansson, J., Løvholt, F., Arwade, S.R., Madshus, C., and DeGroot D.J. (2014), Foundation Damping and the Dynamics of Offshore Wind Turbine Monopiles, manuscript in final preparation, to be submitted to Renewable Resources

NGI (2008), Behaviour of Quick Clay Slopes under Earthquake Loading - Results from Laboratory Testing of Quick Clay, NGI report 20071426-1. Restricted

Menq, F.Y. (2003). Dynamic properties of Sandy and Gravelly soils. Ph.D. Dissertation, The University of Texas, Austin.

Vucetic, M. and R. Dobry (1988). Degradation of marine clays under cyclic loading. Journal of Geotechnical Engineering, ASCE, Vol. 114, No 2, pp. 133-149.

Appendix A - Derivations

Contents

A1 Single degree of freedom system with damper

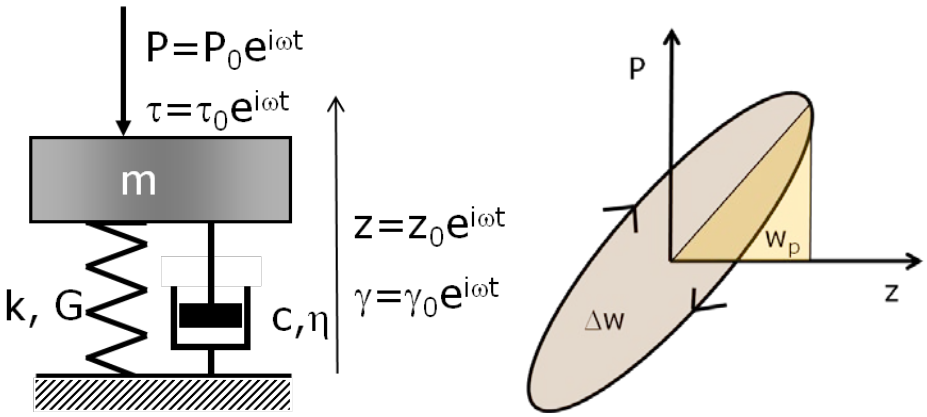

Figure A1.1 Left panel: Sketch of a single degree of freedom spring-dashpot system subject to periodic loading. Right panel: Definition sketch showing the interpretation of potential energy and energy loss in a hysteretic loop.

We consider a single degree of system with a spring and damper defined in Figure A1.1, and first investigate the massless behavior. The load and the displacements are defined as:

$$P = P_0 e^{i\omega t},\ z = z_0 e^{i\omega t},$$

Here, z the time dependent displacement, and z_0 and P_0 are complex displacement and force amplitudes respectively. For the massless system with a complex stiffness $k(1+ik_I)$, this gives the equation of motion:

$$k(1+ik_I)z = P \xrightarrow{z=z_0 e^{i\omega t}} k(1+ik_I) = P_0/z_0.$$

We next consider a spring with stiffness k [N/m] and a viscous damper with a **viscous damping constant** c [N/m/s]. A harmonic load P is also acting on the system. The equation of motion for this system is given by:

$$c\dot{z} + kz = P \xrightarrow{z=z_0 e^{i\omega t}} k(1+i\omega c/k) = P_0/z_0.$$

We see that for this expression with a viscous damper, we get a damping term that is frequency dependent, which differs from the system with the hysteretic damping terms. We now define k_I according to

$$k_I = \frac{c\omega}{k}$$

Using this definition, the force may be written

$$P = kz_0\sqrt{1+k_I^2}\cdot e^{i(\omega t+\varphi)}$$

Here, the phase angle φ is defined as $\varphi=atan(k_I)=asin(k_I/(1+k_I^2)^{1/2})$. The latter expression is useful as it simplifies the derivations below. Formally, the loss factor η is proportional to the ratio of the energy dissipation pr. cycle Δw divided by the potential energy w_p, that is

$$\eta = 2D = \frac{1}{Q} = \frac{1}{2\pi}\frac{\Delta w}{w_p}.$$

Here, we have also defined the **damping factor** *D* which is simply the half of the loss factor, and the **quality factor** *Q* which is the inverse of the loss factor. A visual interpretation of the loss factor in a load displacement diagram is sketched in Figure A1.1. The energy loss Δw is interpreted as the area under the load displacement curve, whereas the potential energy w_p is the area under the triangle. The potential energy may be approximated as

$$w_P = \frac{z_0^2 k}{2},$$

and the energy loss by mean of the integral

$$\begin{aligned}\Delta w = \oint P dz &= \int_0^T P\dot{z}dt \\ &= \int_0^T -z_0\cdot k\cdot\sqrt{1+k_I^2}\cdot\cos(\omega t+\varphi)\cdot z_0\cdot\omega\cdot\sin(\omega t)\,dt \\ &= \pi k z_0^2\sin(\varphi)\sqrt{1+k_I^2}\end{aligned}$$

Giving

$$\eta = \sin(\varphi)\sqrt{1+k_I^2} = \frac{c\omega}{k}$$

Next, we investigate dynamic systems with a non-zero mass, and denote the natural frequency ω_n, the critical damping constant c_{cr} and the **fraction of critical damping** ξ as:

$$\omega_n = \sqrt{\frac{k}{m}},\quad c_{cr} = 2\sqrt{k\cdot m},\quad \xi = \frac{c}{c_{cr}}$$

By applying the equality between the loss factor and the viscous damping above, the derivation below show that the damping factor D equals the degree of critical damping at the natural frequency ω_n, but that they deviate otherwise:

$$D = \frac{\eta}{2} = \frac{1}{2}\frac{c\omega}{k} = \frac{c\omega}{2\cdot\sqrt{k\cdot m}\sqrt{\frac{k}{m}}} = \frac{c}{c_{cr}}\frac{\omega}{\omega_n} = \xi\frac{\omega}{\omega_n}$$

Hence, a frequency independent damping or loss factor implies that ξ is inversely proportional to the frequency. On the other hand, a purely viscous damping, keeping ξ constant, gives a damping or loss factor increasing linearly with frequency. Figure A1.2 shows a sketch of the damping factors in the respective systems.

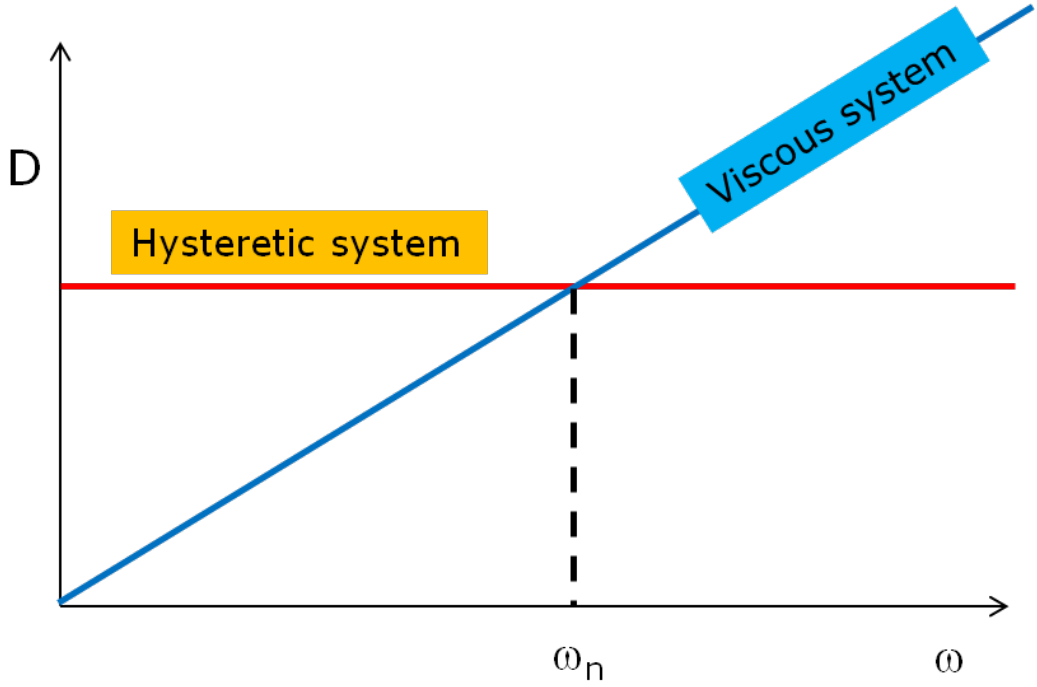

Figure A1.2 Sketch showing the damping factor for a frequency independent hysteretic and a frequency dependent viscous system as a function of the angular frequency

Based on the above definitions and using a viscous damper, we may define amplification factors for a viscous and a hysteretic system that arises from the force balance according to

$$\rho_v(\omega) = \left|\frac{z_0 k}{P_0}\right| = \left|\frac{1}{\left(1-\left(\frac{\omega}{\omega_n}\right)^2\right)+i2\left(\frac{\omega}{\omega_n}\right)\xi}\right| = \frac{1}{\sqrt{(1-(\frac{\omega}{\omega_n})^2)^2+(2\xi\frac{\omega}{\omega_n})^2}},$$

and

$$\rho_h(\omega) = \left|\frac{z_0 k}{P_0}\right| = \left|\frac{1}{\left(1-\left(\frac{\omega}{\omega_n}\right)^2\right)+i\eta}\right| = \frac{1}{\sqrt{(1-(\frac{\omega}{\omega_n})^2)^2+\eta^2}}.$$

Figure A1.3 shows the amplification factors for different values of c, and comparing the responses with a pure viscous (frequency dependent damping) and a hysteretic damper. A unitary mass and a spring stiffness k = 100 N/m was applied. ρ_v and ρ_h corresponds to a pure viscous and hysteretic damper, correspondingly.

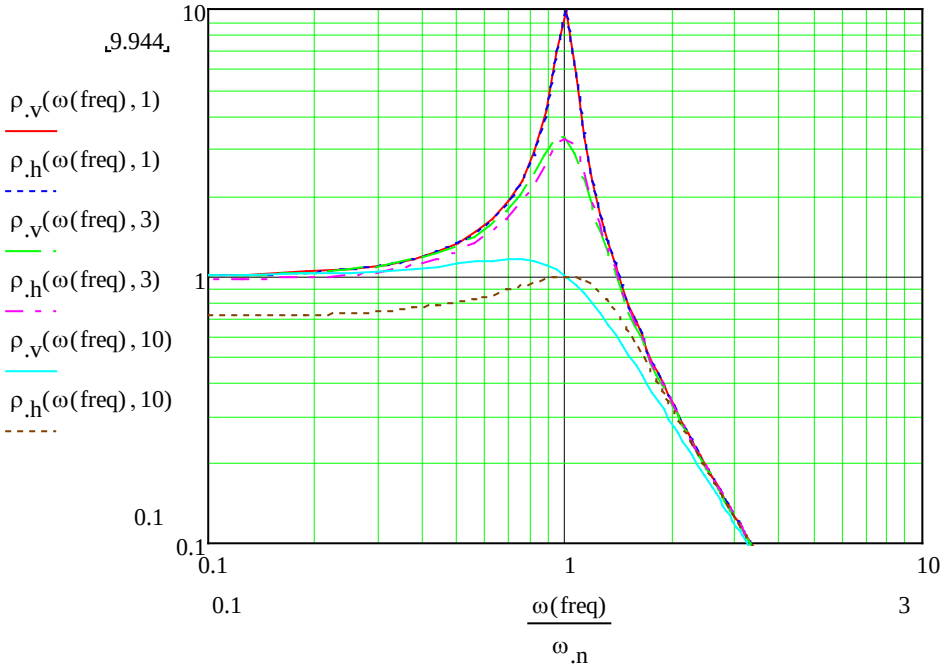

Figure A1.3 Examples of amplification factors as function of the normalized load frequency. ρ_v and ρ_h corresponds to pure viscous and hysteretic dampers, correspondingly. The values of c are 1, 3, and 10. We see that whereas the peak amplification factors all appear for the same frequency for the hysteretic damper, a frequency shift appears for the viscous damper.

A2 Damped single degree of freedom system coupled serially with an additional damper

We consider the system with two dampers and one spring defined in Figure A2.1, and first investigates the massless behavior. The system represents a case where the displacement (or strain) may accumulate. The damping constant for the new additional damper is denoted c_1, and the terms associated with c_1 are subsequently referred to as strain accumulation terms. The load acting on this system is a superposition of a constant and a harmonic load. Correspondingly,

we obtain the solution for the displacement by adding the static and harmonic displacement. We derive the following static response.

$$z_S = \frac{P_S}{c_1} t$$

The dynamic displacement may again be derived from the force balance giving

$z_0 = \frac{P_0}{k} \frac{1}{(1-\kappa)+ik_I(1-\kappa)}, \ \kappa = \frac{1+ik_I}{1+ik_\Sigma}, \quad k_{I1} = \frac{c_1\omega}{k}, k_\Sigma = k_{I1} + k_I$
(with strain accumulation)

$z_0 = \frac{P_0}{k} \frac{1}{1+ik_I} = \frac{P_0}{k} \frac{1}{1+k_I^2}(1 - ik_I)$
(without strain accumulation)

Hence, we see that the strain accumulation term represents a correction to the soil response, represented with the terms κ and k_{I1}. By transforming the equation above, we obtain alternative forms for the displacement:

$z_0 = \frac{P_0}{ikk_{I1}} \frac{1}{\kappa} = \frac{P_0}{k\cdot(1+k_I^2)}(1 - i\psi), \quad \psi = \frac{1+k_I^2}{k_{I1}} + k_I$ (with strain accumulation)

From this equation it is evident that the strain accumulation term only adds correction to the imaginary part of the displacement. Furthermore, we see that the correction is large if c_1 is small (large strain accumulation), but that it vanishes if c_1 is large (negligible strain accumulation). For computing the loss factor, it is convenient to invert the above expression to yield the force as a function of the displacement, i.e.

$$P_0 = \frac{z_0 \cdot k \cdot k_{I1}^2}{1 + k_\Sigma^2}(1 + i\psi) = \frac{z_0 \cdot k \cdot k_{I1}^2}{1 + k_\Sigma^2}\sqrt{1 + \psi^2}e^{i\varphi}$$

Here, the phase angle φ is defined as $\varphi = atan(\psi) = asin(\psi/(1+\psi^2)^{1/2})$Integrating the real part of the load and displacement yields the following result of the energy dissipation Δω:

$$\begin{aligned}\Delta w = \oint P dz &= \int_0^T P\dot{z} dt \\ &= \int_0^T \frac{-z_0^2 \cdot k \cdot k_{I1}^2 \cdot \sqrt{1+\psi^2} \cdot \cos(\omega t + \varphi) \cdot \omega \cdot \sin(\omega t)\, dt}{1 + k_\Sigma^2} \\ &= \frac{\pi k k_{I1}^2 z_0^2}{1 + k_\Sigma^2}\psi\end{aligned}$$

The estimate for the energy loss from the SDOF system above is retained, so we get the following expression for the loss factor, corrected for accumulated displacement:

$$\eta = \frac{1}{2\pi}\frac{\Delta w}{w_p} = \frac{1}{2\pi}\frac{z_0^2\pi k k_{I1}^2}{(1+k_\Sigma^2)}\frac{2\psi}{kz_0^2} = \frac{k_{I1}^2\psi}{1+k_\Sigma^2} \xrightarrow{c \ll c_1} \frac{c\omega}{k},$$

i.e., we obtain the original SDOF expression for the loss factor when c_1 is large.

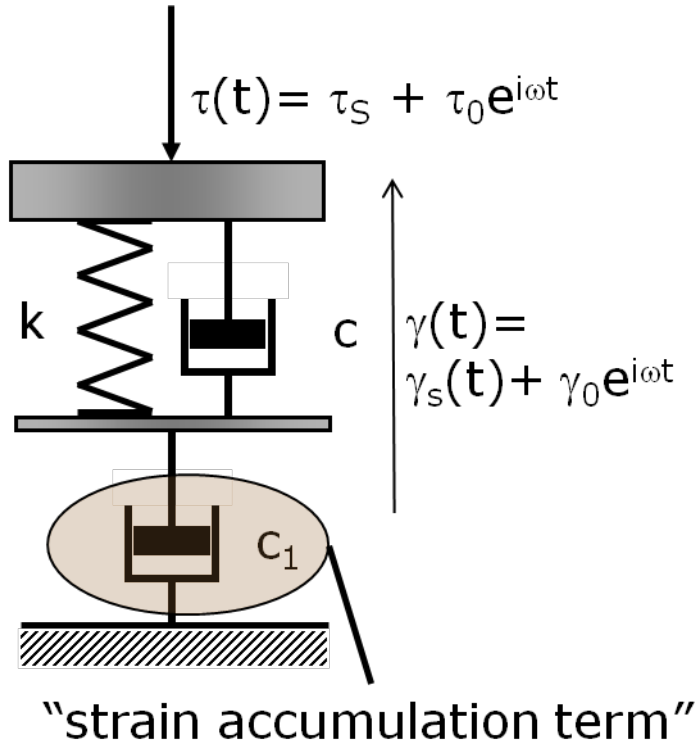

Figure A2.1 Sketch of a single degree of a mass-spring-dashpot coupled to a single viscous damper and system subject to periodic loading. The subscripts "s" represents static load and displacement terms.

Next, we consider the coupled system with a nonzero mass. The force balance for the harmonic components of the load and displacement yields the following amplification factor:

$$\rho = \left|\frac{z_0 k}{P_0}\right| = \left|\frac{1}{\left(1-\kappa-\left(\frac{\omega}{\omega_n}\right)^2\right)+i2\left(\frac{\omega}{\omega_n}\right)\cdot\xi\cdot(1-\kappa)}\right|,$$

applies to the stiffness and damping terms as for the massless system. Figure A2.2 depicts the amplification factor as a function of frequency for different

values of c_1. A unitary mass and a spring stiffness k = 100 N/m was applied, and a value of c = 4 was used. The smallest values of c_1 correspond to a system with large displacement accumulation, providing much larger amplification for the lowest frequencies. For large values of c_1 the amplification factor becomes almost identical to the SDOF system with a damper.

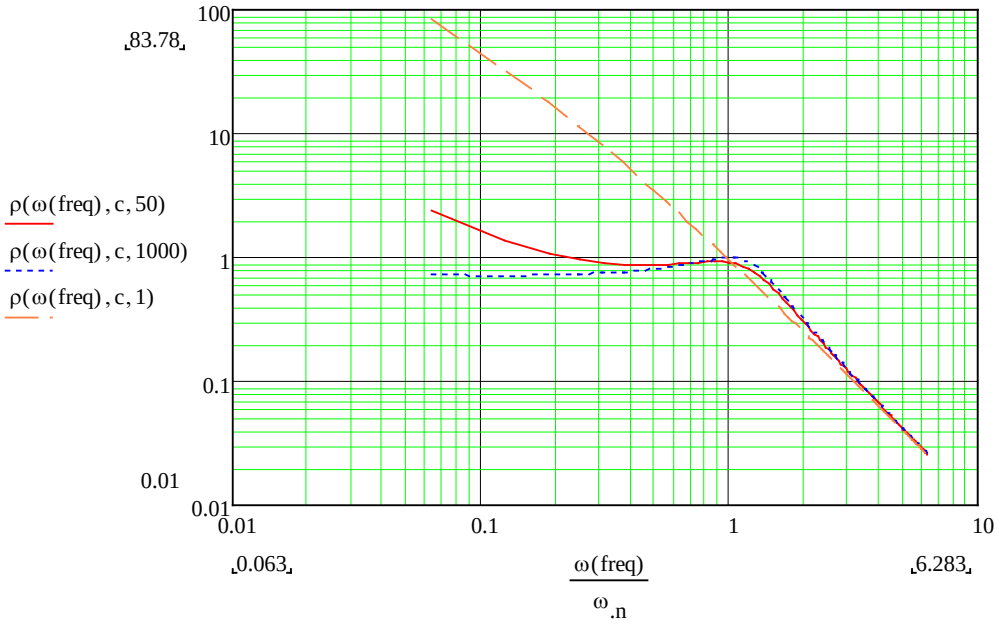

Figure A2.2 Examples of amplification factors as function of the normalized load frequency for the coupled system. The values of c_1 are 1, 50, and 1000.

Appendix B - Examples of damping curves from cyclic DSS tests

Contents

B1 A very brief description of the investigated soil samples

The present Appendix depicts outcomes of a range of cyclic DSS tests with respect to damping. Figures B2.1-B2.13 display results for clay samples, whereas Figures B2.14-B2.17 display results of tests conducted for sand.

The clay samples had a water content of about w=39%, a clay content of about 38%, unit weight of solid particles of γ_s=27.74 kN/m^3, a plasticity index of about I_p=11%, liquid and plastic limits of about w_l=31% and w_p=20%, a sensitivity of more than S_t=70, and an apparent overconsolidation ratio (OCR) due to secondary consolidation less than 1.5. The preconsolidation stress was obtained from constant rate of strain oedometer tests. Grain size distribution curves are presented in Figure B1.1. Further details of the samples are given in NGI (2008). Average shear stresses of about $0.17\cdot\sigma_{vc}$', $0.22\cdot\sigma_{vc}$' and $0.3\cdot\sigma_{vc}$' were used respectively, where σ_{vc}' denotes vertical consolidation stress.

The sand samples are clean sand with D10=0.09 mm. Test 1131 and 1104 have relative densities of 100%, σ_{vc}' = 200 kPa, and Overconsolidation Ratio (OCR)=1. Test 1199 has a relative density of 80%, σ_{vc}' = 200 kPa, and OCR=4. Test 1150 has a relative density of 100%, σ_{vc}' = 40 kPa, and OCR=1.

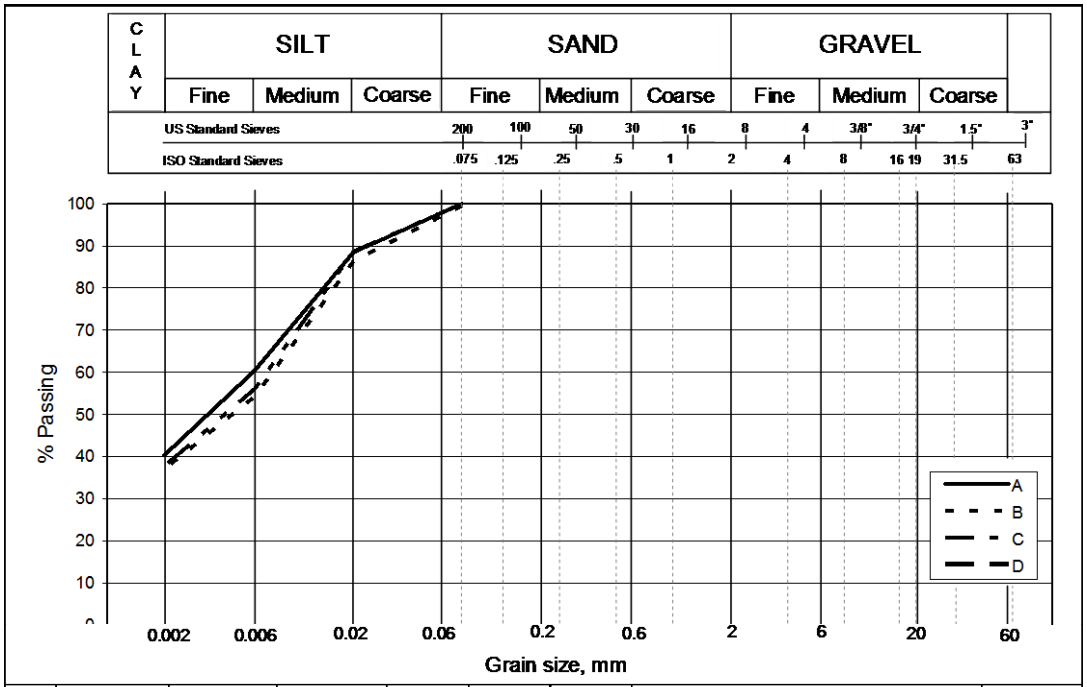

Curve	Boring No.	Sample No.	Depth m	D_{10} mm	D_{60} mm	Clay cont. %	Soil Description	Method dry/wet-sieving
A	200	3-16	10.62		0.006	40.3	CLAY	Falling drop
B	200	3-17	10.67		0.007	37.0	CLAY	Falling drop
C	200	3-19	10.67		0.007	37.7	CLAY	Falling drop

Figure B1.1 Grain size distribution curves for clay samples

B2 Results

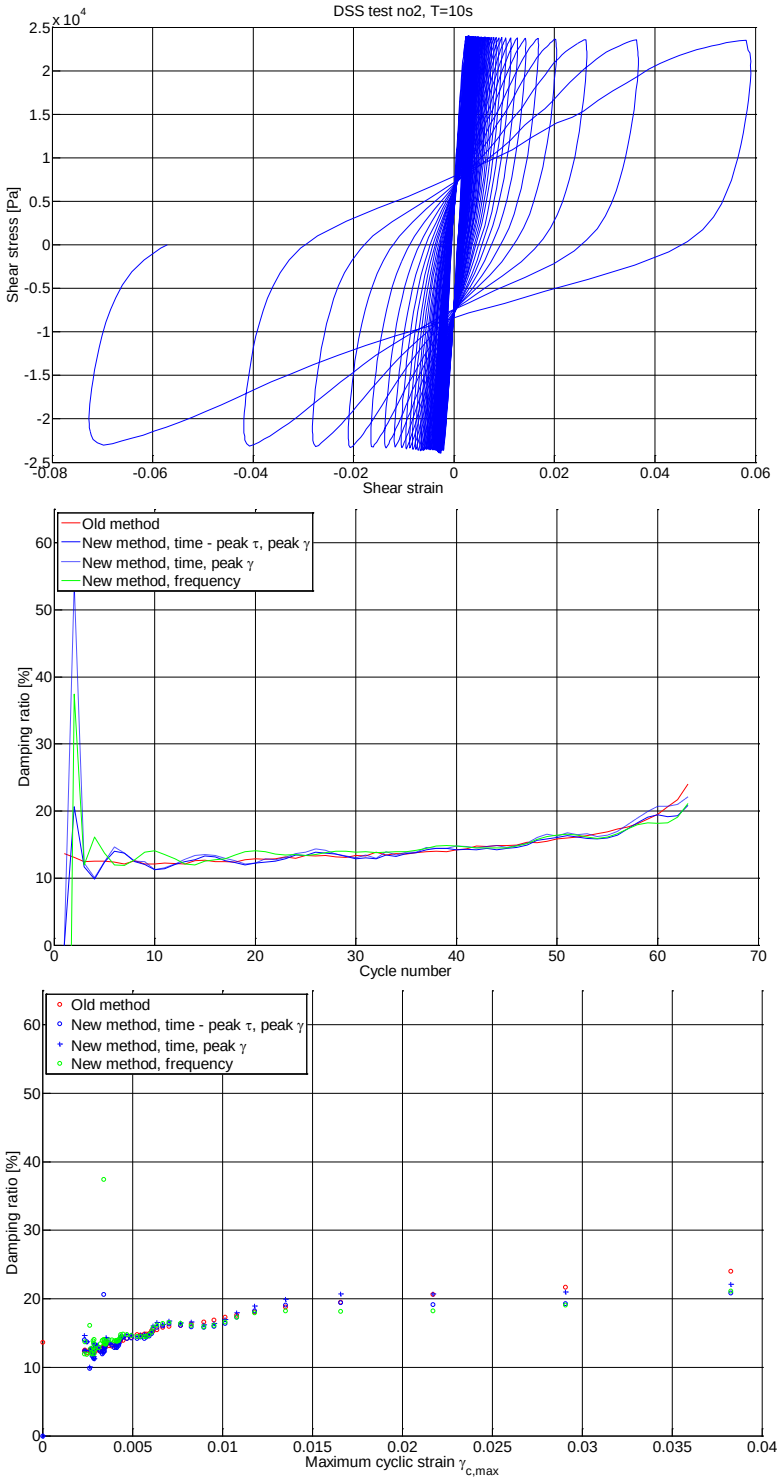

Figure B2.1 Results from cyclic DSS test for DSS2 (clay sample). Upper panel, stress-strain loop. Mid panel, the damping parameter as a function of the cycle number using three different methods. Lower panel, damping parameter as a function of the maximum cyclic strain using three different methods.

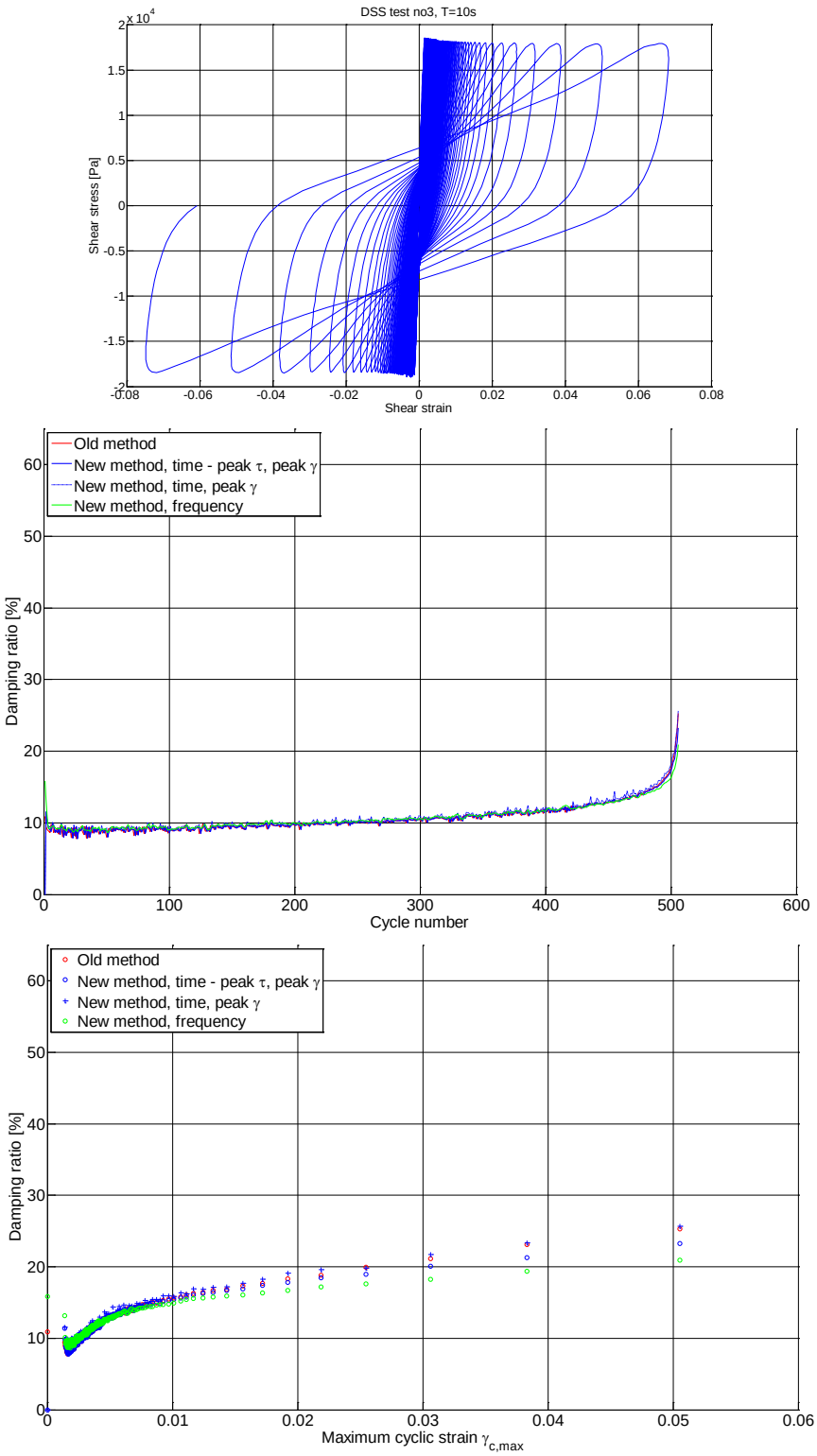

Figure B2.2 Results from cyclic DSS test for DSS3 (clay sample). Upper panel, stress-strain loop. Mid panel, the damping parameter as a function of the cycle number using three different methods. Lower panel, damping parameter as a function of the maximum cyclic strain using three different methods.

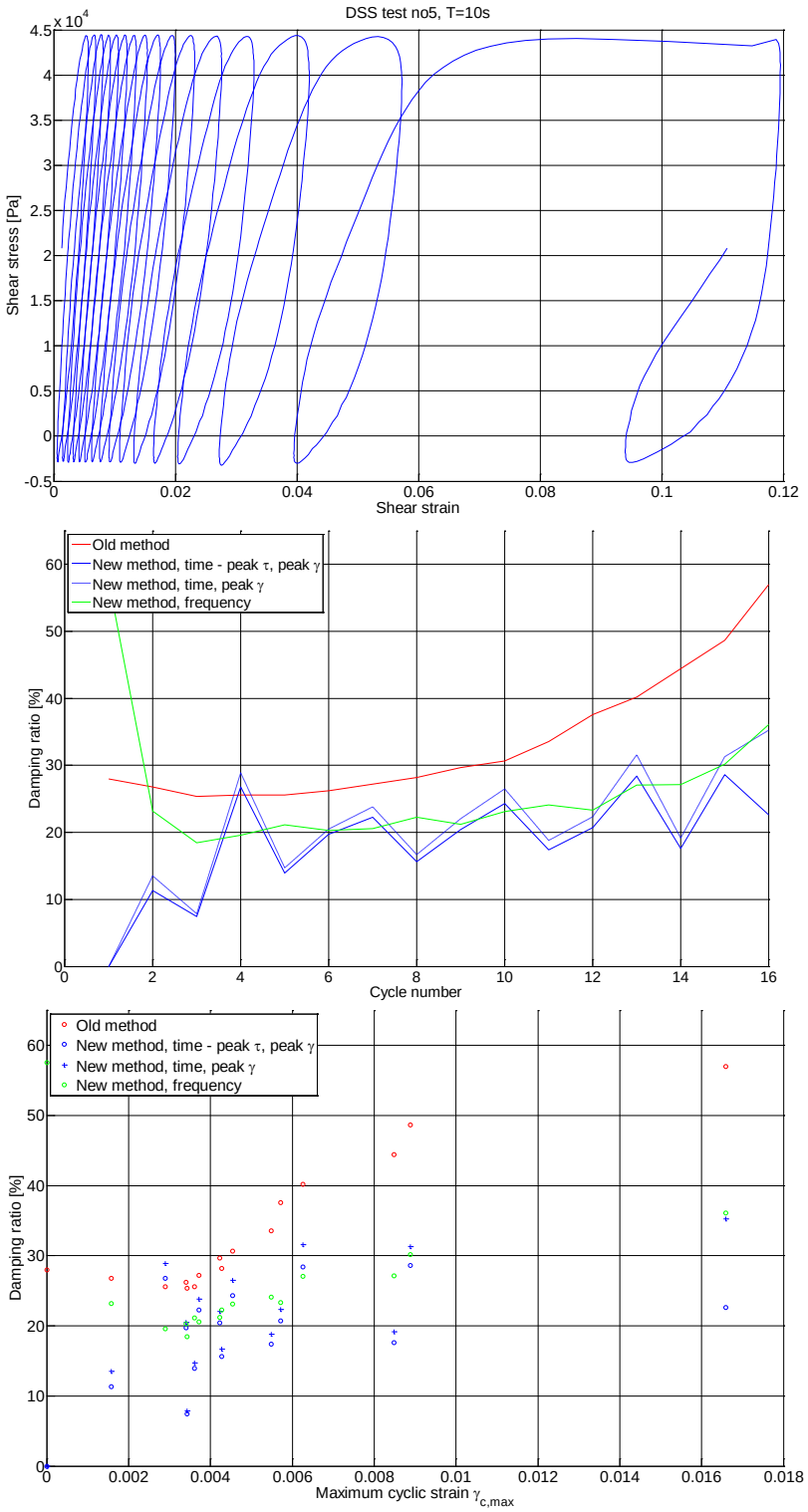

Figure B2.3 Results from cyclic DSS test for DSS5 (clay sample). Upper panel, stress-strain loop. Mid panel, the damping parameter as a function of the cycle number using three different methods. Lower panel, damping parameter as a function of the maximum cyclic strain using three different methods.

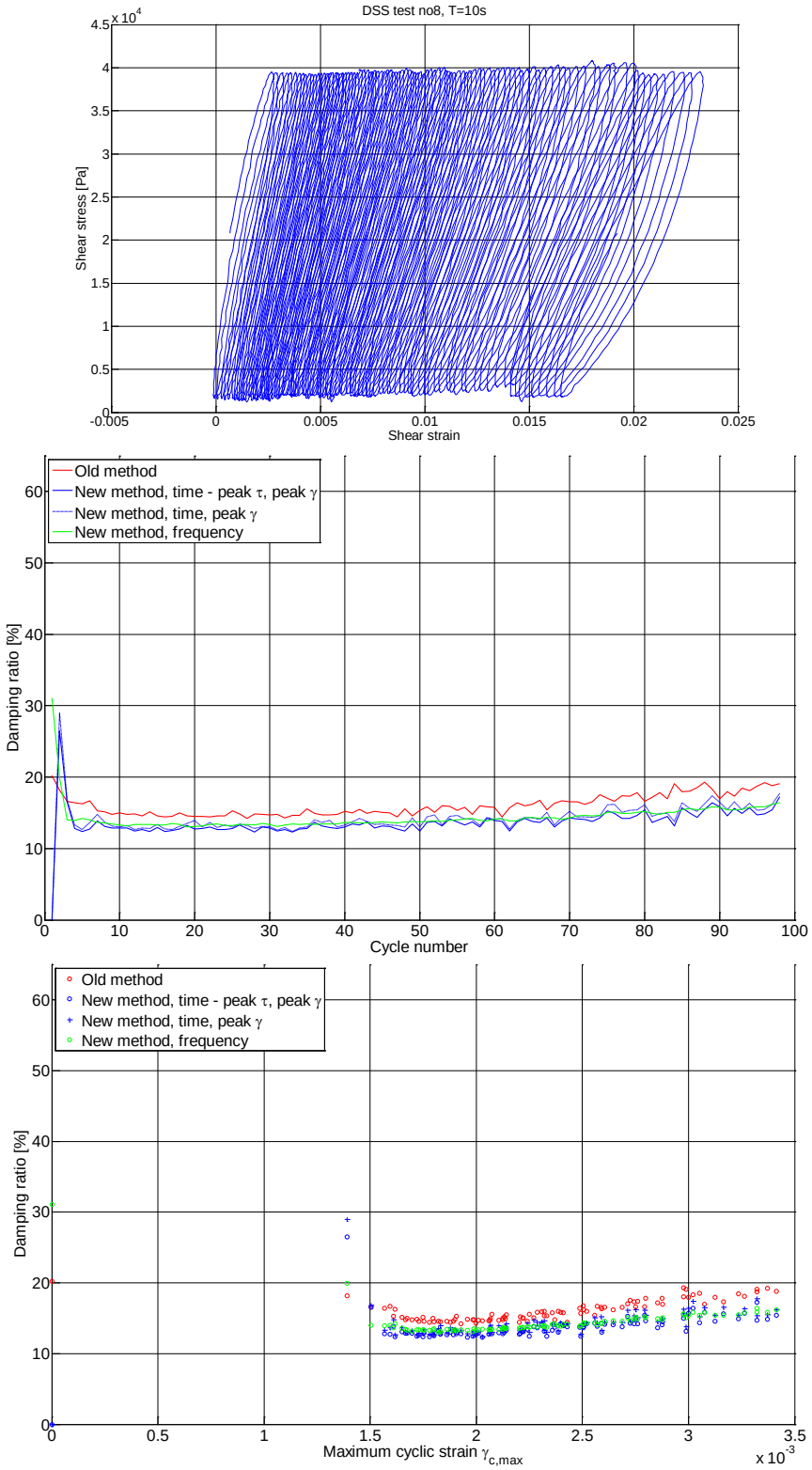

Figure B2.4 Results from cyclic DSS test for DSS8 (clay sample). Upper panel, stress-strain loop. Mid panel, the damping parameter as a function of the cycle number using three different methods. Lower panel, damping parameter as a function of the maximum cyclic strain using three different methods.

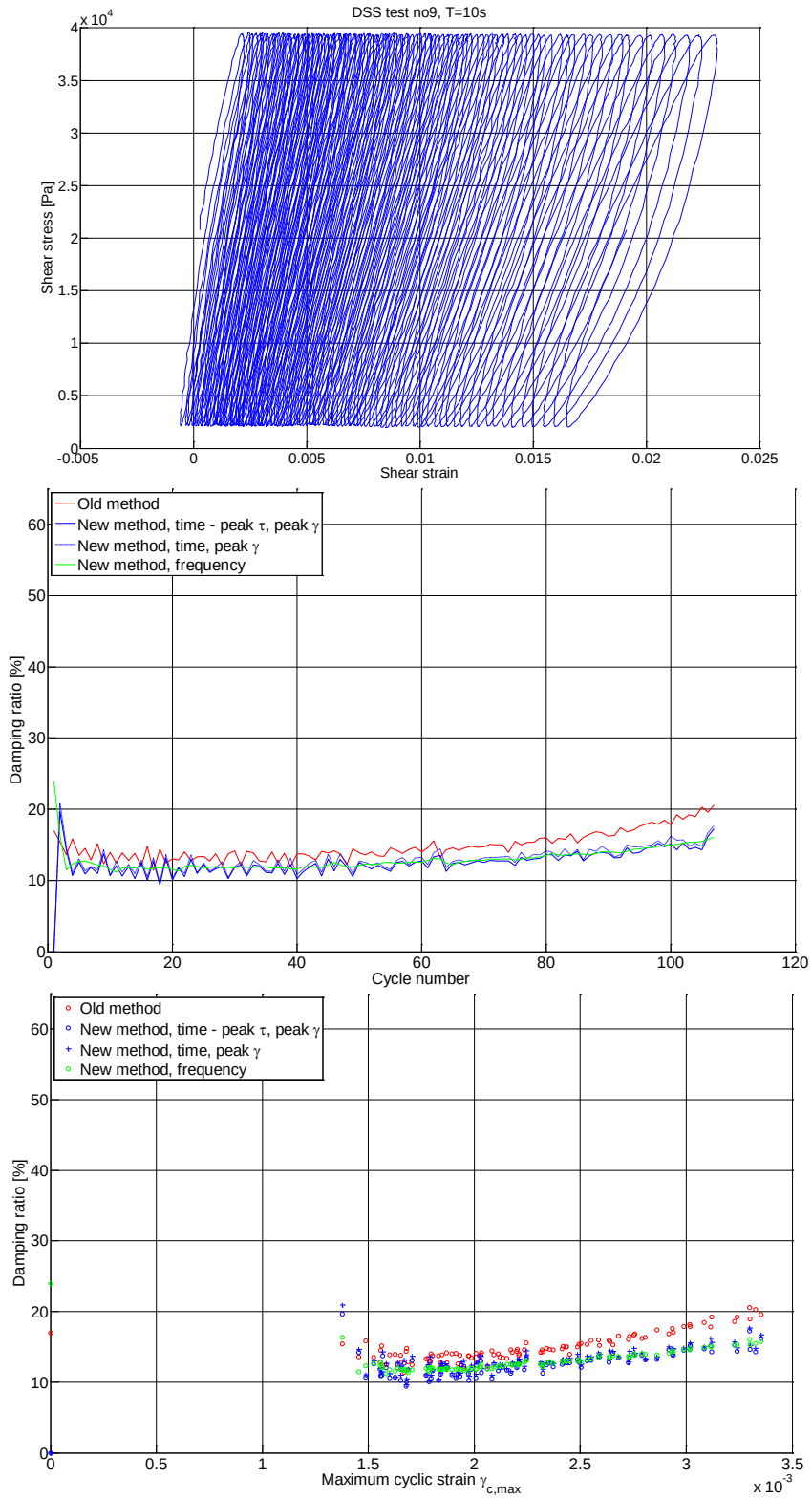

Figure B2.5 Results from cyclic DSS test for DSS9 (clay sample). Upper panel, stress-strain loop. Mid panel, the damping parameter as a function of the cycle number using three different methods. Lower panel, damping parameter as a function of the maximum cyclic strain using three different methods.

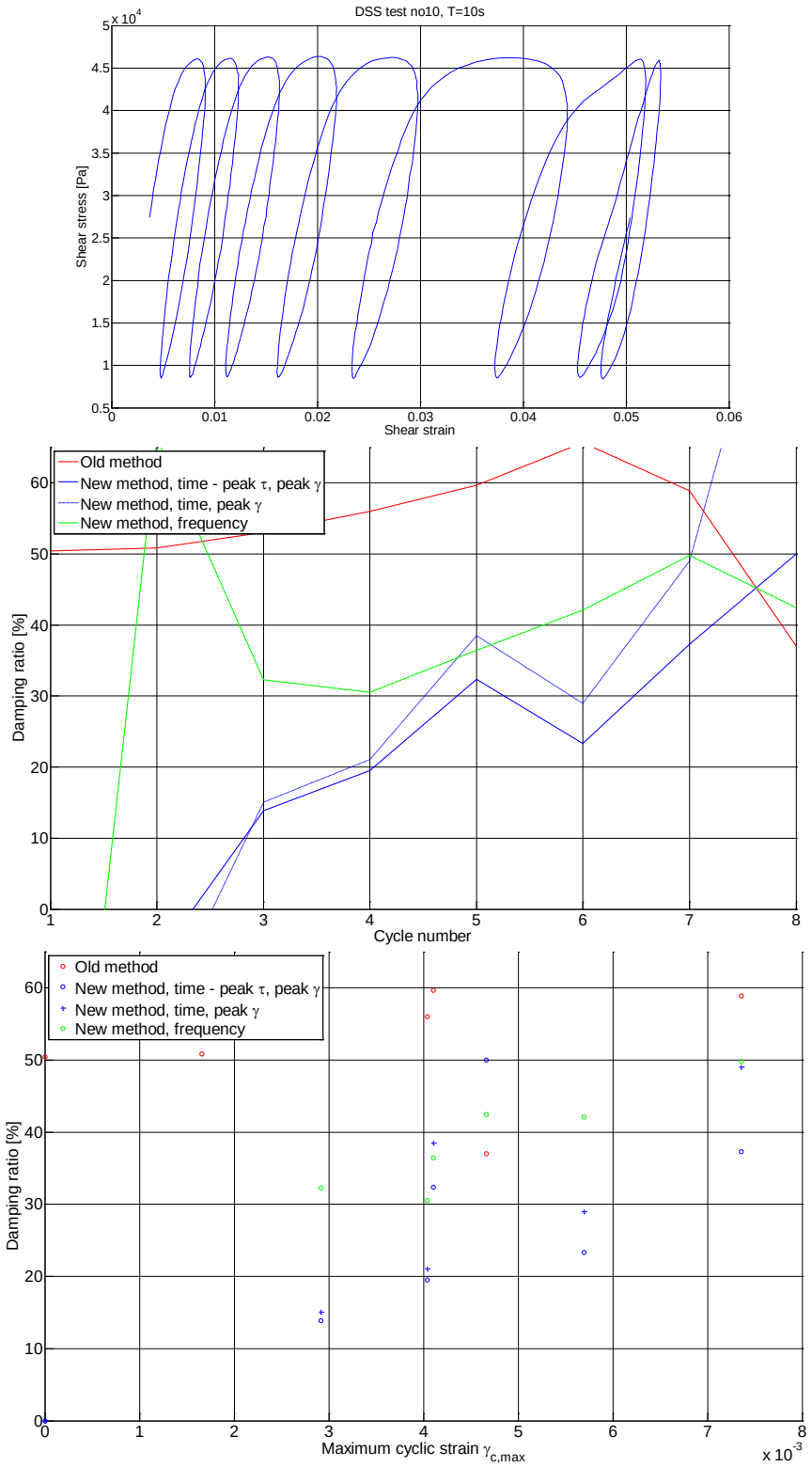

Figure B2.6 Results from cyclic DSS test for DSS10 (clay sample). Upper panel, stress-strain loop. Mid panel, the damping parameter as a function of the cycle number using three different methods. Lower panel, damping parameter as a function of the maximum cyclic strain using three different methods.

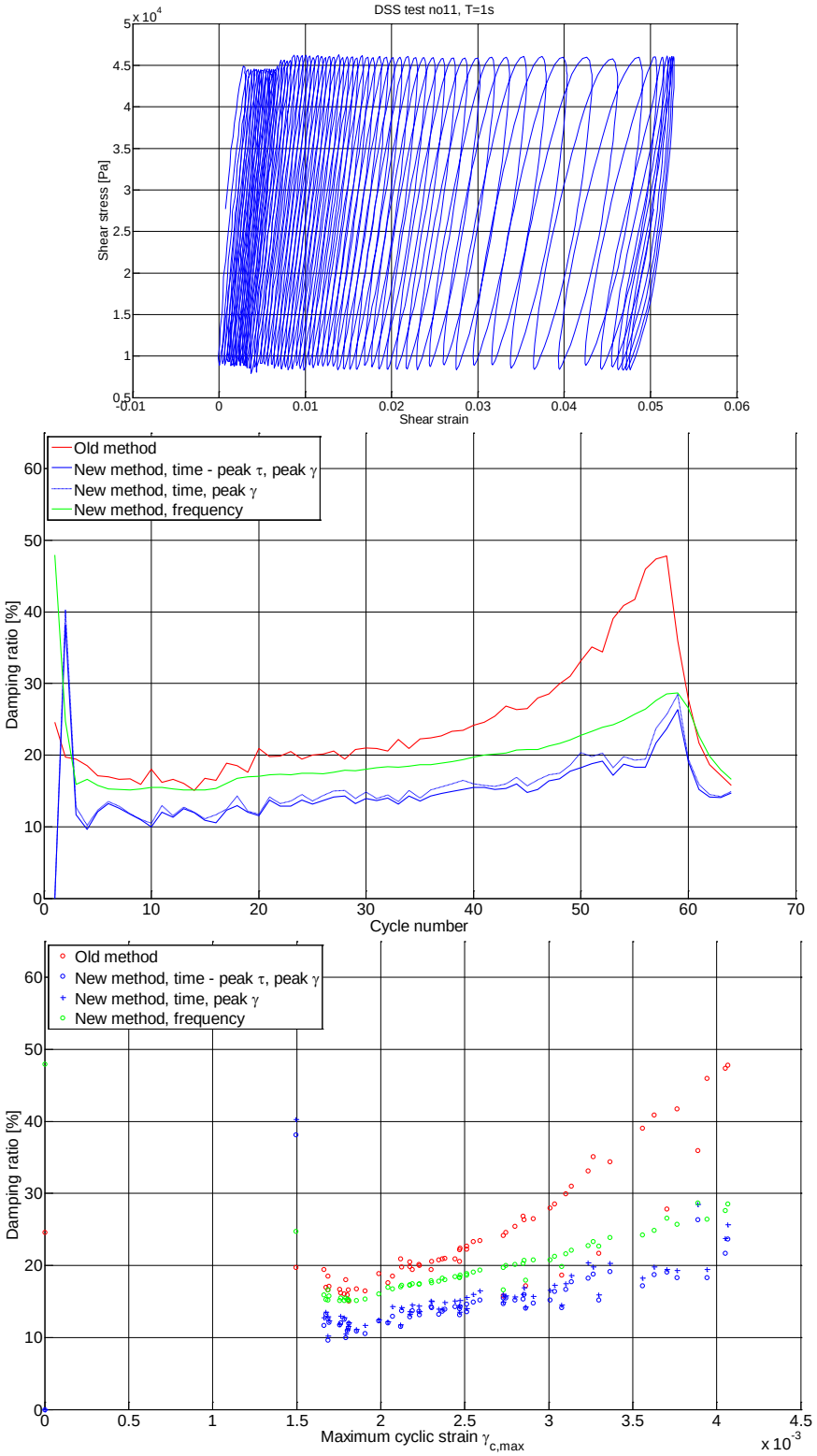

Figure B2.7 Results from cyclic DSS test for DSS11 (clay sample). Upper panel, stress-strain loop. Mid panel, the damping parameter as a function of the cycle number using three different methods. Lower panel, damping parameter as a function of the maximum cyclic strain using three different methods.

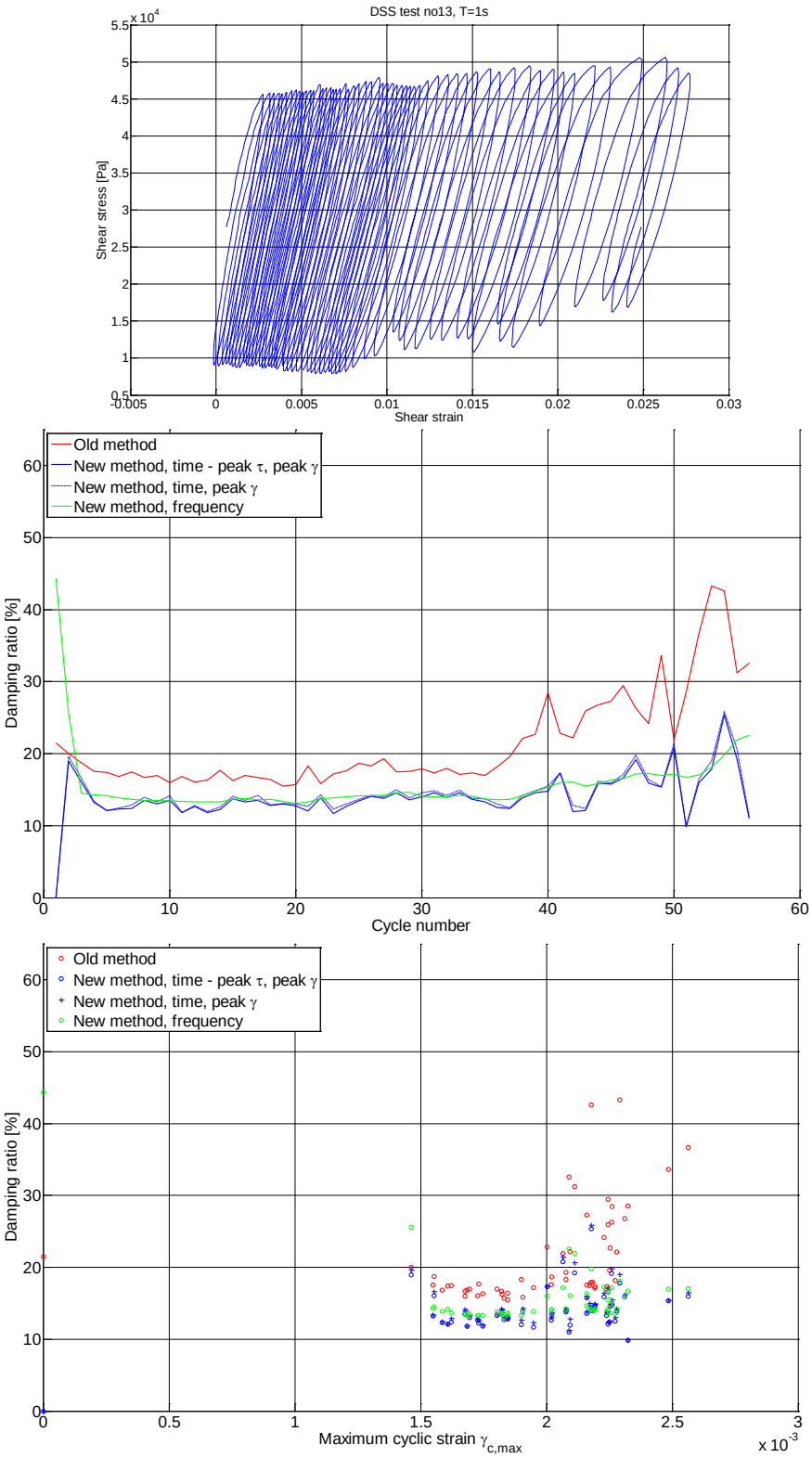

Figure 2.8 *Results from cyclic DSS test for DSS13 (clay sample). Upper panel, stress-strain loop. Mid panel, the damping parameter as a function of the cycle number using three different methods. Lower panel, damping parameter as a function of the maximum cyclic strain using three different methods.*

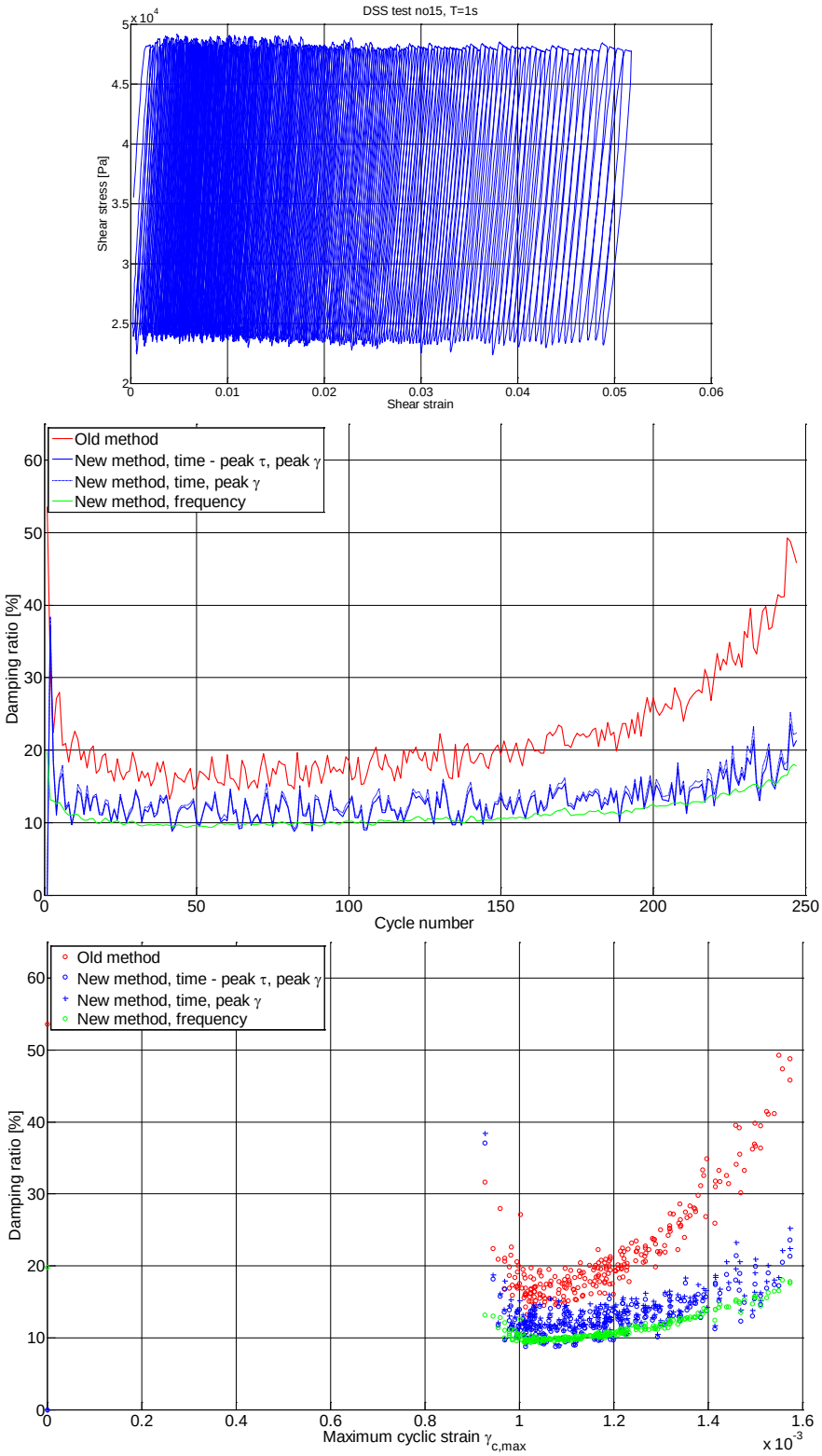

Figure 2.9 *Results from cyclic DSS test for DSS15 (clay sample). Upper panel, stress-strain loop. Mid panel, the damping parameter as a function of the cycle number using three different methods. Lower panel, damping parameter as a function of the maximum cyclic strain using three different methods.*

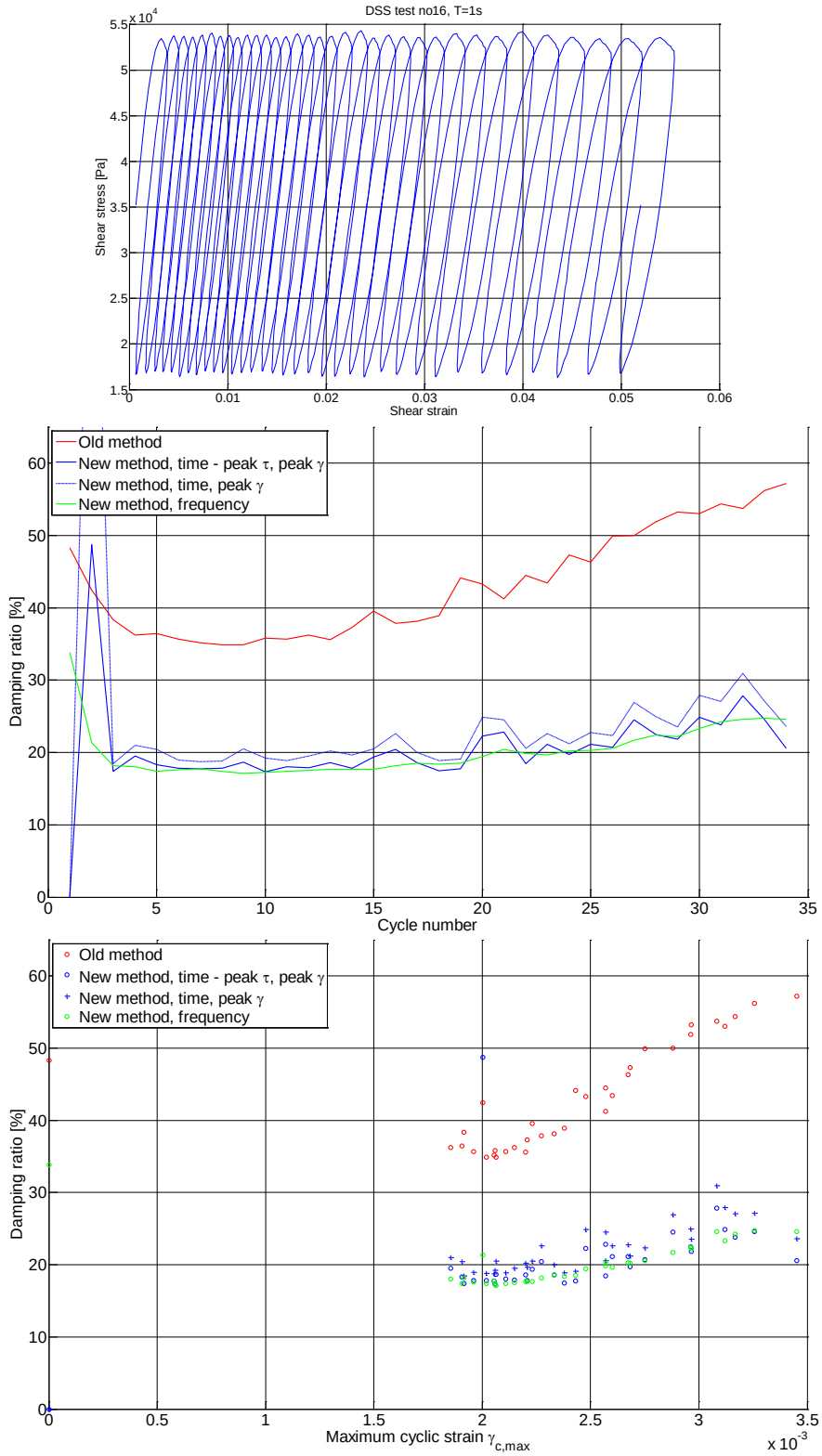

Figure B2.10 Results from cyclic DSS test for DSS16 (clay sample). Upper panel, stress-strain loop. Mid panel, the damping parameter as a function of the cycle number using three different methods. Lower panel, damping parameter as a function of the maximum cyclic strain using three different methods.

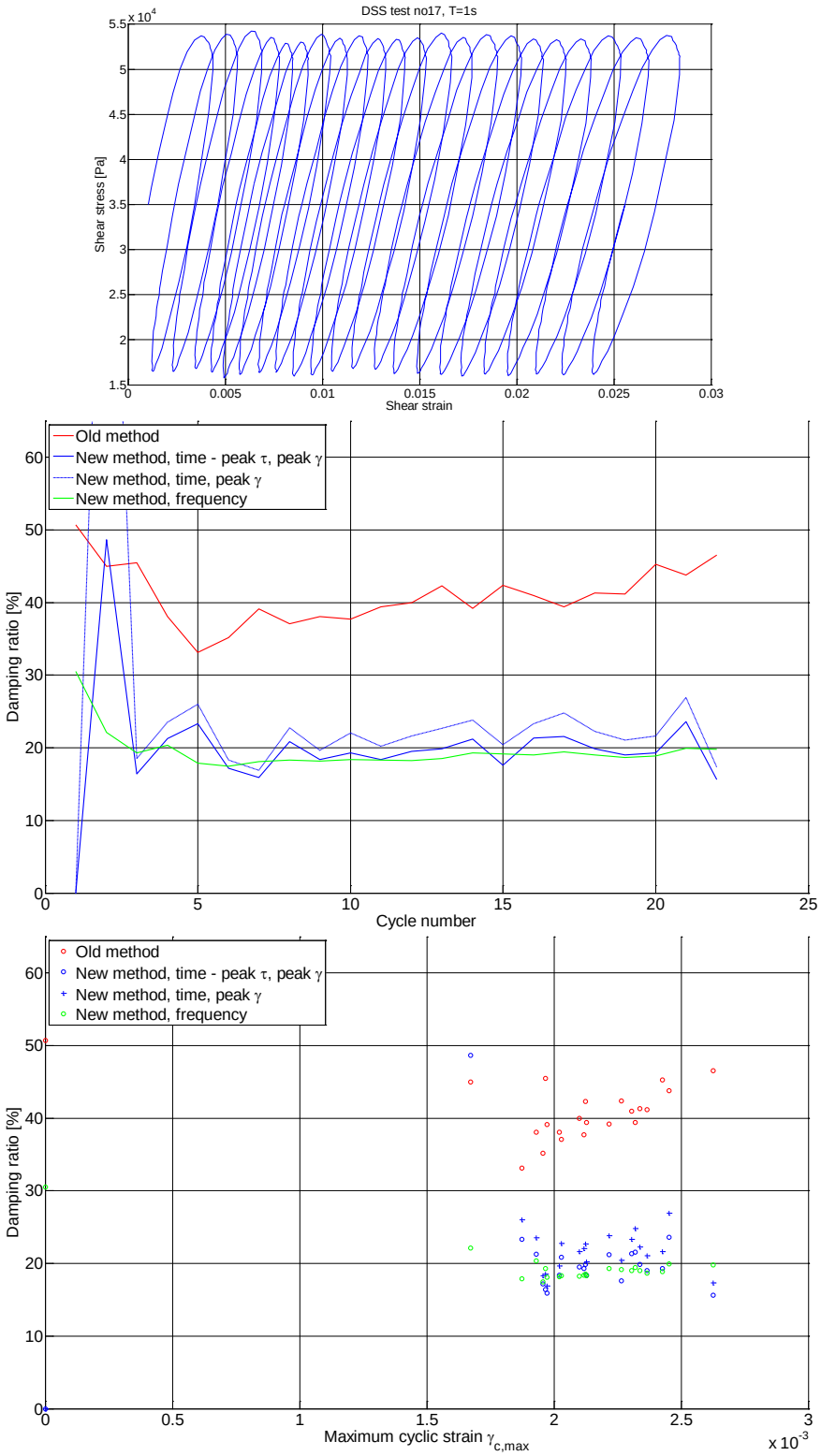

Figure B2.11 Results from cyclic DSS test for DSS17 (clay sample). Upper panel, stress-strain loop. Mid panel, the damping parameter as a function of the cycle number using three different methods. Lower panel, damping parameter as a function of the maximum cyclic strain using three different methods.

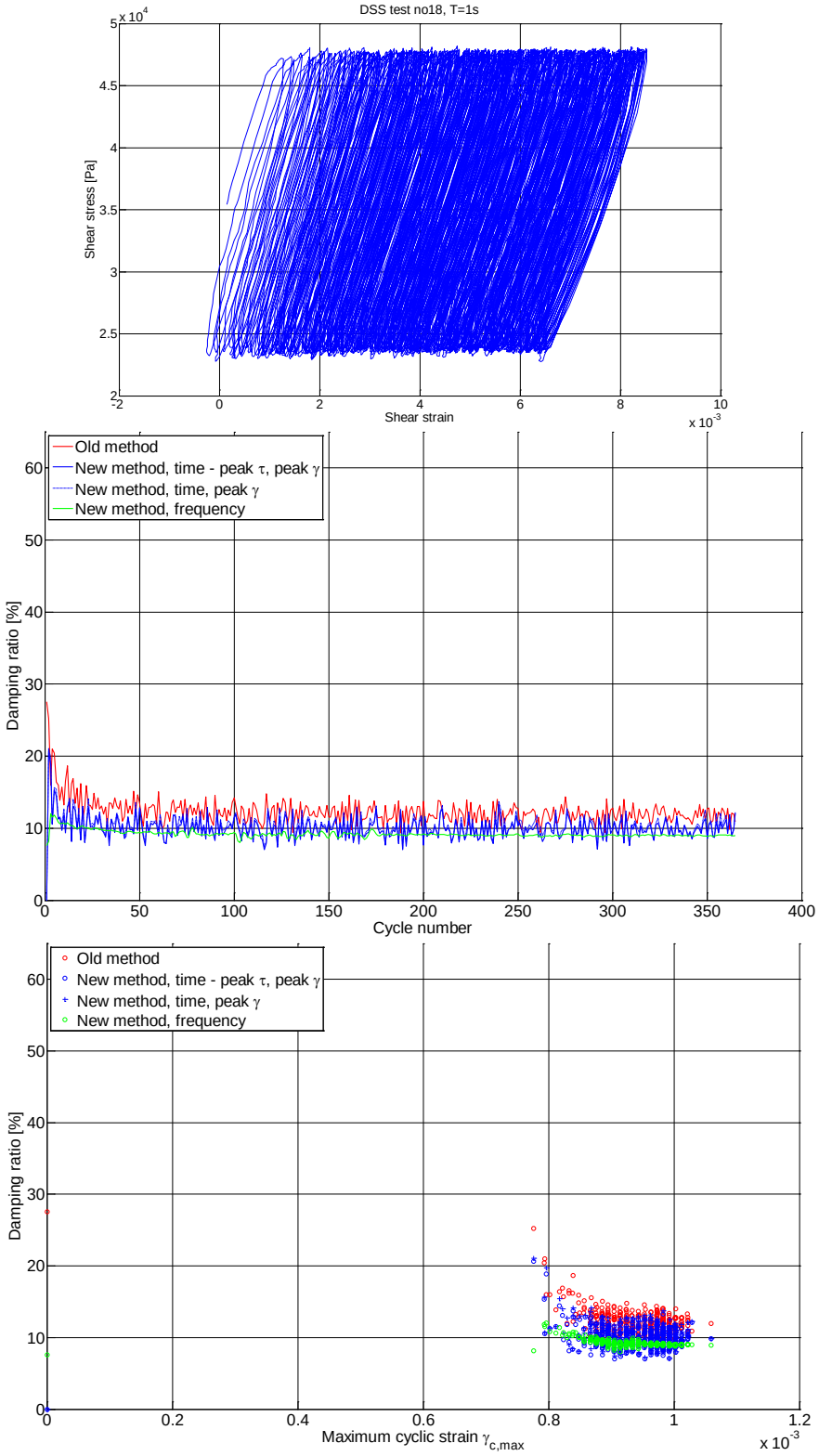

Figure B2.12 Results from cyclic DSS test for DSS18 (clay sample). Upper panel, stress-strain loop. Mid panel, the damping parameter as a function of the cycle number using three different methods. Lower panel, damping parameter as a function of the maximum cyclic strain using three different method.

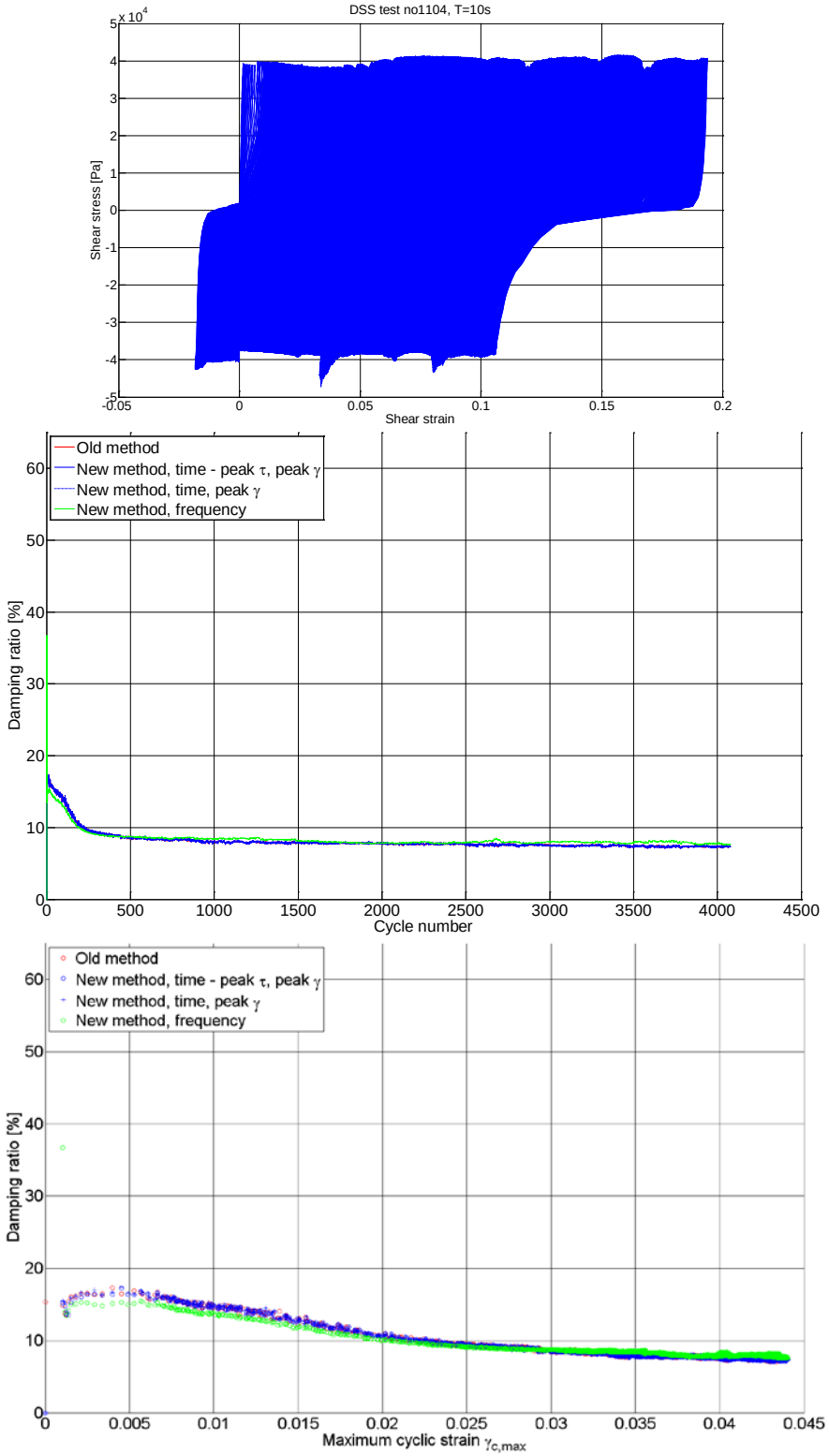

Figure B2.13 Results from cyclic DSS test for DSS1104 (sand sample). Upper panel, stress-strain loop. Mid panel, the damping parameter as a function of the cycle number using three different methods. Lower panel, damping parameter as a function of the maximum cyclic strain using three different methods.

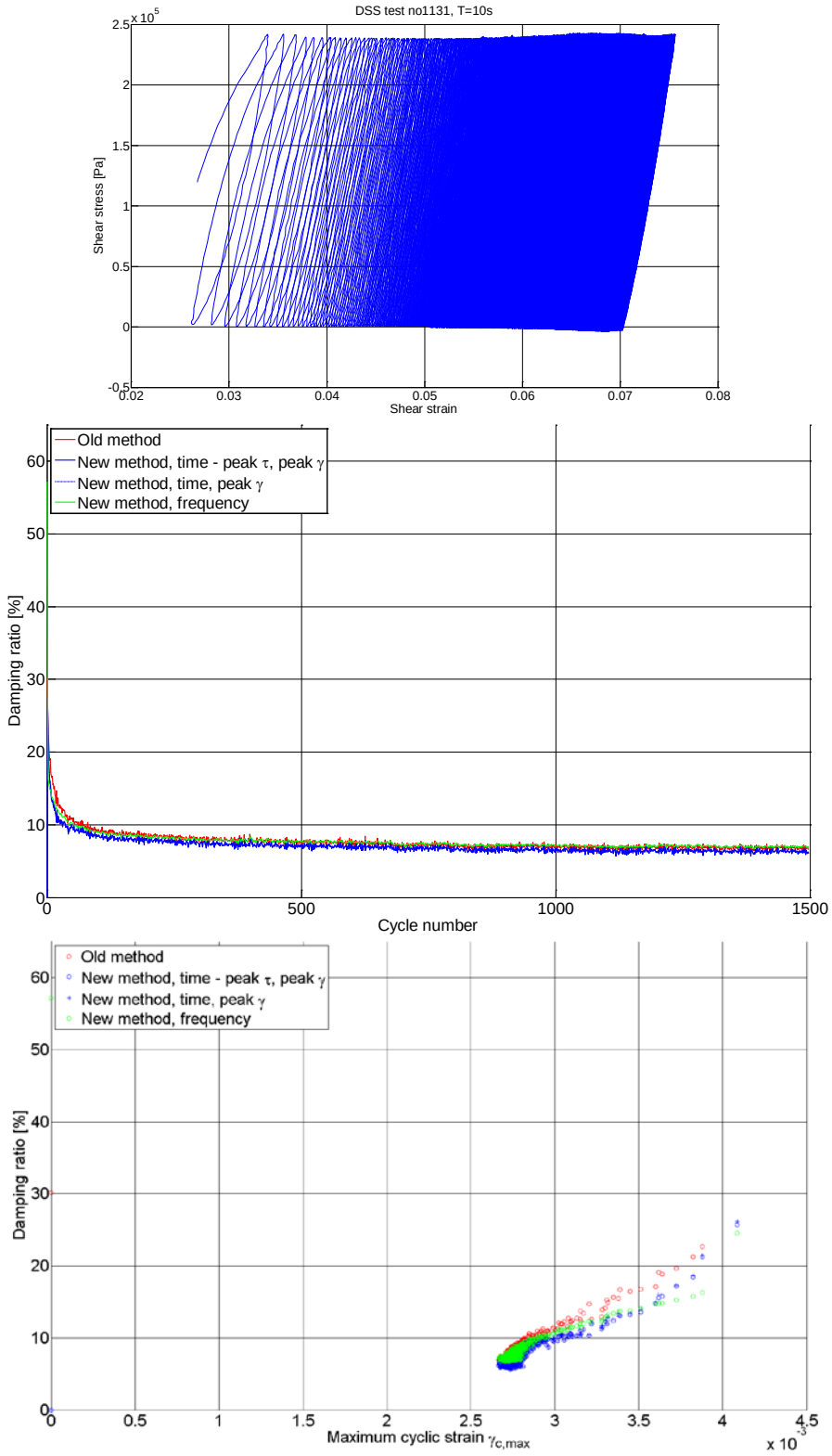

Figure B2.14 Results from cyclic DSS test for DSS1131 (sand sample). Upper panel, stress-strain loop. Mid panel, the damping parameter as a function of the cycle number using three different methods. Lower panel, damping parameter as a function of the maximum cyclic strain using three different methods.

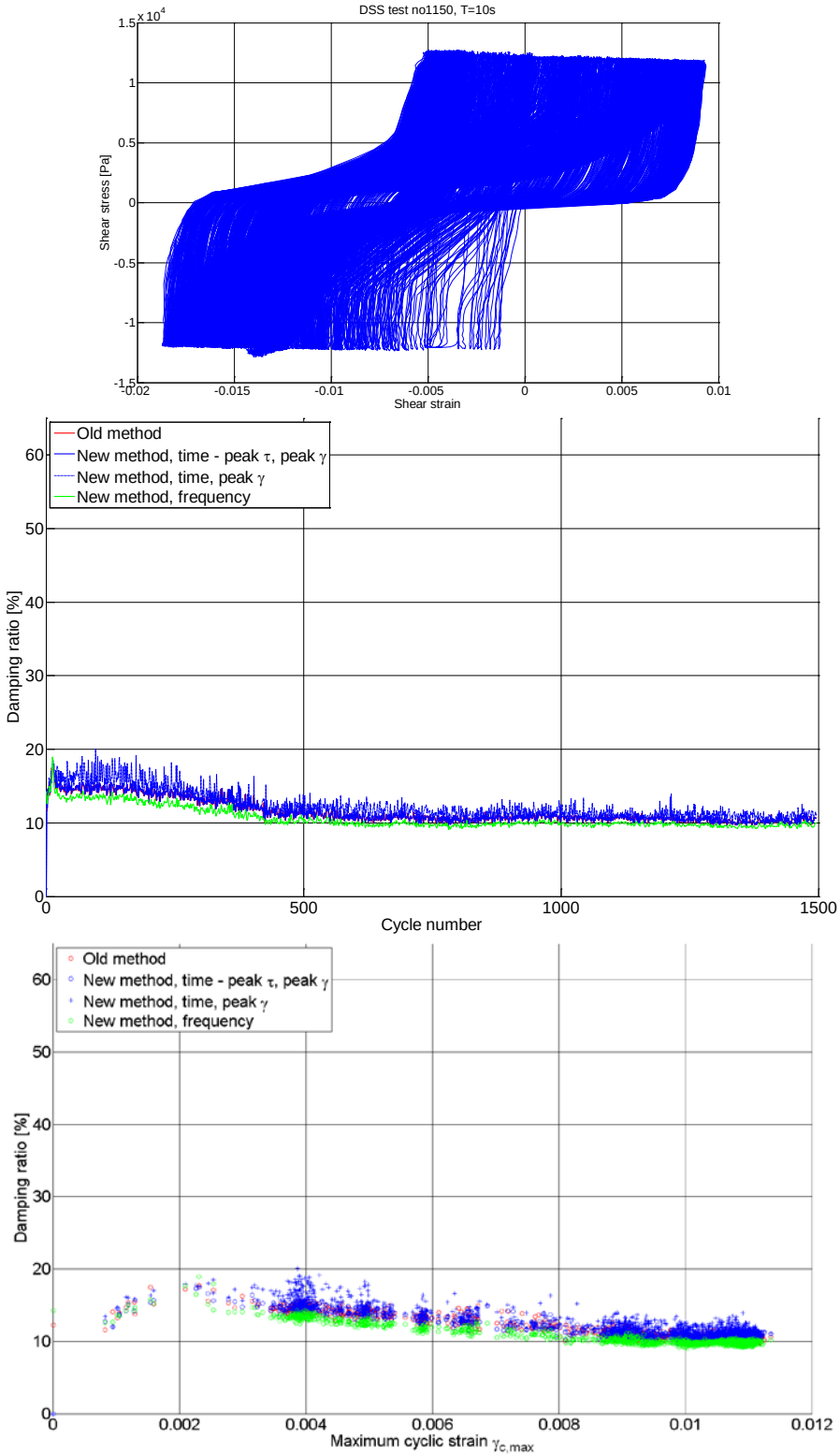

Figure B2.15 Results from cyclic DSS test for DSS1150 (sand sample). Upper panel, stress-strain loop. Mid panel, the damping parameter as a function of the cycle number using three different methods. Lower panel, damping parameter as a function of the maximum cyclic strain using three different methods.

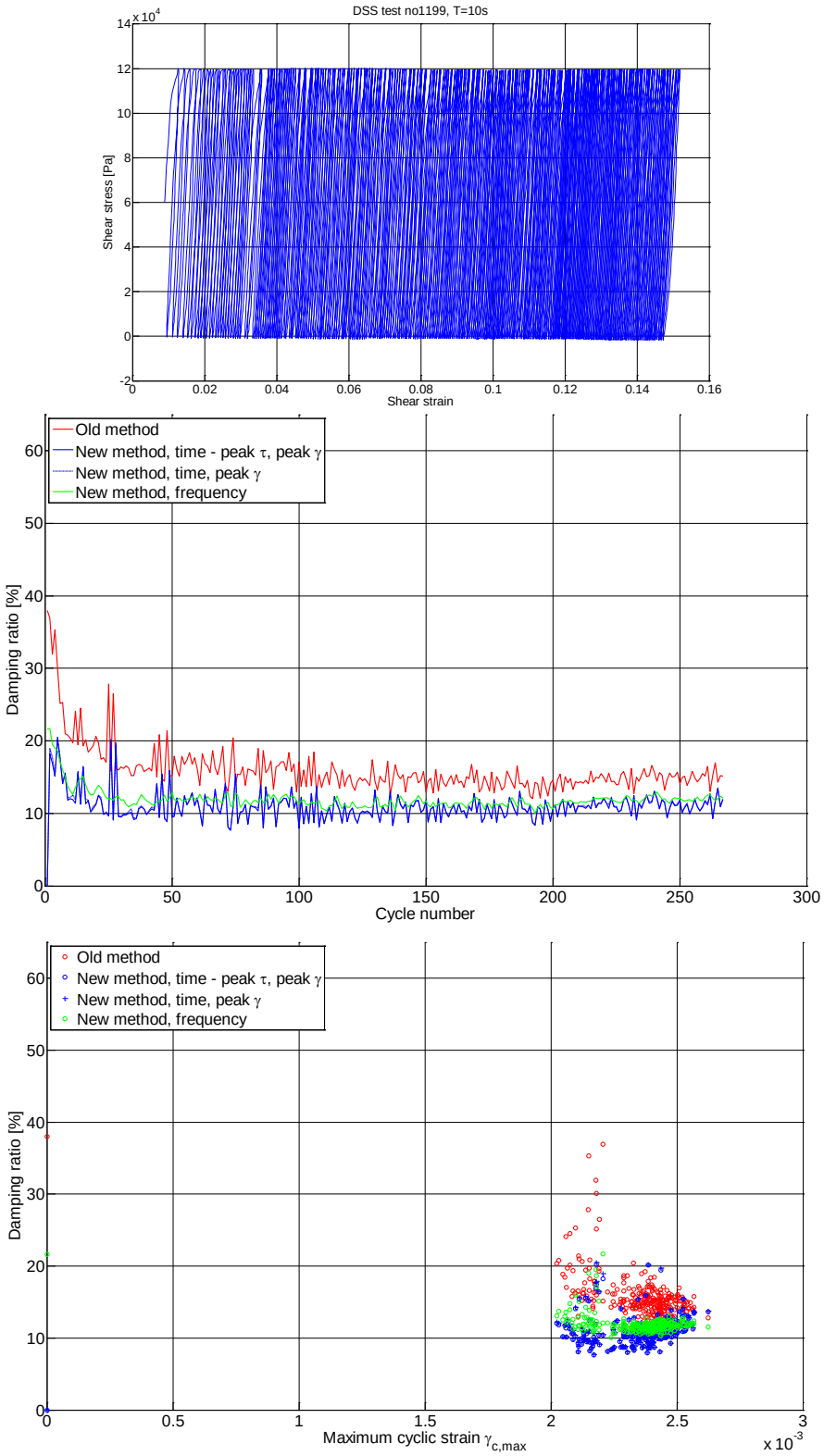

Figure B2.16 Results from cyclic DSS test for DSS1199 (sand sample). Upper panel, stress-strain loop. Mid panel, the damping parameter as a function of the cycle number using three different methods. Lower panel, damping parameter as a function of the maximum cyclic strain using three different methods.

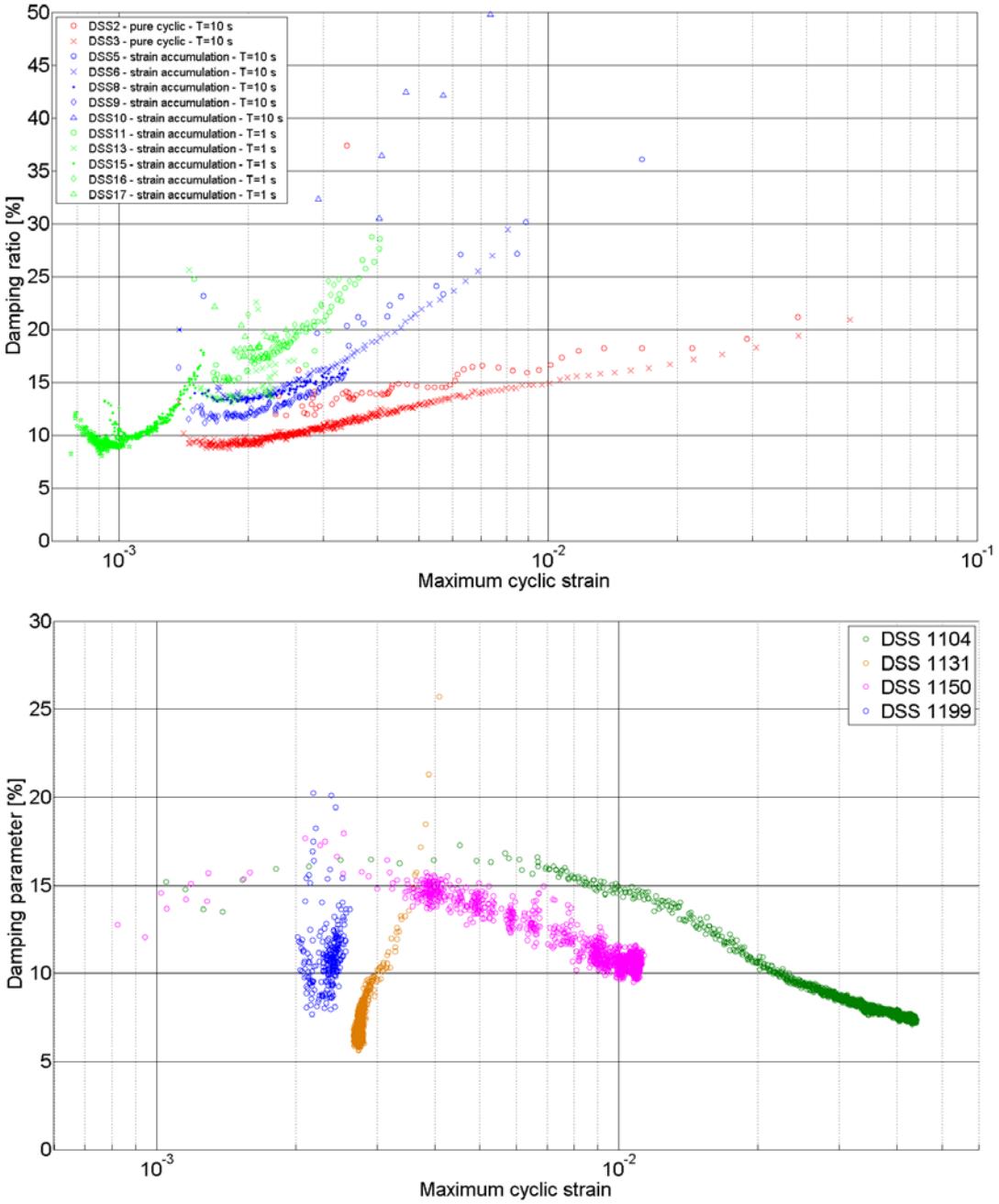

Figure B2.17 The damping parameter as a function of the maximum cyclic strain. Upper panel, all the clay tests compiled using the frequency phase method. Lower panel, all the sand tests compiled using the integral method and the secant stiffness at maximum shear stress.

Appendix C - A procedure for obtaining Global Foundation stiffness and damping

Contents

C1 Introduction

A procedure for obtaining Global foundation stiffness and damping values with help of an FE analysis has been developed. Horizontal and rotational load displacement curves and damping values for a mono-pile have been established intended to be used for an integrated structural analysis of an 5MW NREL offshore wind turbine. A typical monopile foundation and soil profile from a wind farm in the North Sea was used.

C2 Methodology

Mudline loads to be applied to the foundation were computed with the software FAST /7/ with a fixed base turbine model. In an NGI in house nonlinear finite element code the loads from FAST were applied to model of the mono-pile and surrounding soil.

Available information on the structural components of the mono-pile were used to establish a simplified foundation model. Information in references /1/, such as initial stiffness and strength parameters, were used to establish necessary input parameters for the FE-analysis of the foundation and soil.

To establish foundation stiffness and damping values to be used in a structural dynamic analysis, consistent stress-strain and damping-strain curves, covering a large range of shear strain from 1e-4% to 10%, has been established for the different soil layers, based on the geotechnical information in /1/ together with so called modulus reduction and damping curves from reference /3/.

The stress-strain and damping-strain curves are used in the FE-analysis to compute load displacement curves for the foundation. The applied loads and computed foundation displacements and rotations are used to establish uncoupled horizontal and rotational spring stiffness values and corresponding damping values.

C2.1 Description of the NGI foundation FE-tool (Infidel)

The in-house FE-software, Infidel is used in the analysis. It is a non-linear, 3-D Finite Element program and it is primarily intended for soil-structure interaction analysis during design of offshore structures. Incompressible or near-incompressible soils can be modelled. The soil volume in the computational model may extend to infinity in all horizontal directions. Special skirt and shell elements allow a simplified modelling of structure flexibility.

It is a static analysis tool with non-linear stress-strain constitutive models for the soil. In addition it uses curves for damping factor-strain to compute hysteretic energy loss as described in the next section.

C2.1.1 Damping computations

The NGI in-house code Infidel software computes a global hysteretic damping ratio for the system analysed. This is accomplished by means of numerical integration of the hysteresis energy (area of loop) over the entire soil volume.

The damping factor, D, in a soil element is defined as

$$D = \frac{A_L}{4\pi A_T}$$

Here A_T is the strain energy at maximum strain during a cycle. A_L is the area of the hysteresis loop, i.e. it represents the energy absorbed by the sample in the course of one load cycle.

Infidel computes a corresponding global foundation damping factor, D_{found}, as

$$D_{found} = \frac{E_h}{4\pi E_s}$$

Where E_h, is the hysteretic energy summed up for all elements and E_s is the elastic strain energy summed up for all elements.

C2.1.2 Modelling assumptions

For the purpose of the FE-analysis of the loads below, the mono-pile foundation was modelled with solid elements with an equivalent Youngs modulus as to give the same bending stiffness as the monopile. The poisson's ratio of the steel in the mono pile was kept at 0.3.

For large ratio between cross section dimension and the active pile length, shear deformations need to be accounted for. This has not been considered in the performed analysis and the resulting bending stiffness of the equivalent pile may be higher than the bending stiffness of the prototype mono-pile.

The pile was assumed to be in full contact with the soil, effects of gapping due to non-linear compression of the soil on the side of the pile and/or erosion has not been considered.

The foundation loads computed with FAST was applied to the Infidel model over 20 steps with 2 iterations per step. The loads were increased proportionally assuming that the mudline horizontal load and moment are in phase.

C3 Wind and wave loads on 5MW NREL wind turbine

Loads used to establish foundation stiffness and damping were computed with FAST /8/. The FAST software has a built-in model of the 5MW NREL wind turbine.

The horizontal force and moment load at the mudline were established for environmental conditions corresponding to 18 m/s turbulent winds, a significant wave height of 5 m, and peak spectral wave period of 12.4 seconds.

Time histories of mudline moment and horizontal load are shown in Figure C3.1 and Figure C3.2 and their Fourier spectra are shown in Figure C3.3 and Figure C3.4.

The time histories indicated that the mudline moment is dominated by the wind loading, resulting in a mudline moment, M, approximately proportional to the horizontal load, H. Multiplying the average horizontal force with the height of the OWT (90 m) results in a value similar to the average moment.

The dominant frequency of the loading is used both in computing soil material damping wich is an in the Infidel analysis, and also for establishing viscous dashpot coefficients representing the foundation hysteretic energy loss.

The foundation analysis below were based on a maximum mudline shear force of 2210 kN and an overturning moment of 88680 kNm taken from the time histories.

Vertical loading has not been considered in this study.

In the load computations with FAST the bottom of the OWT is clamped, i.e. the foundation stiffness is infinite. Preliminary results not presented within here indicate that using foundation with realistic stiffness in FAST may increase the loads and also reduce the dominant loading frequency.

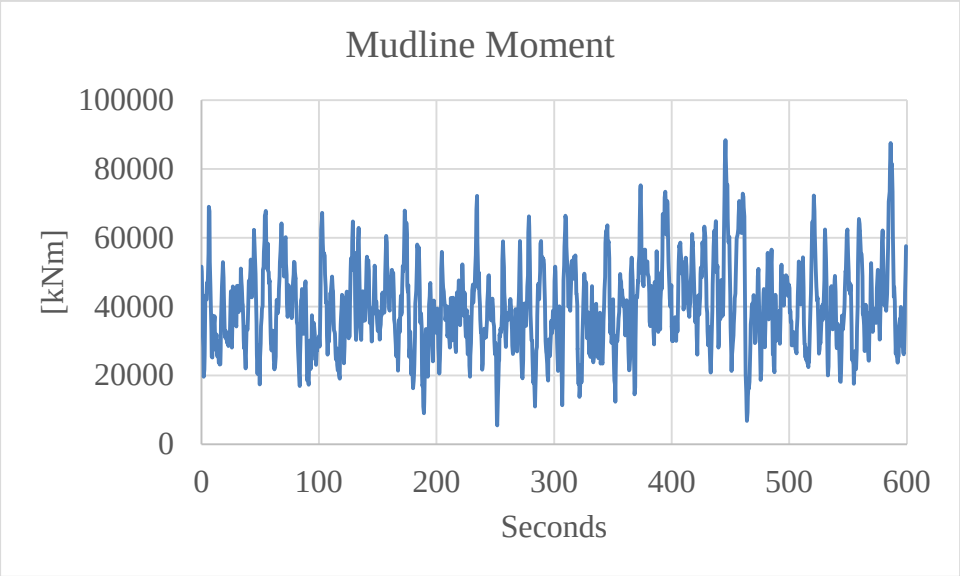

Figure C3.1 Mudline moment time history

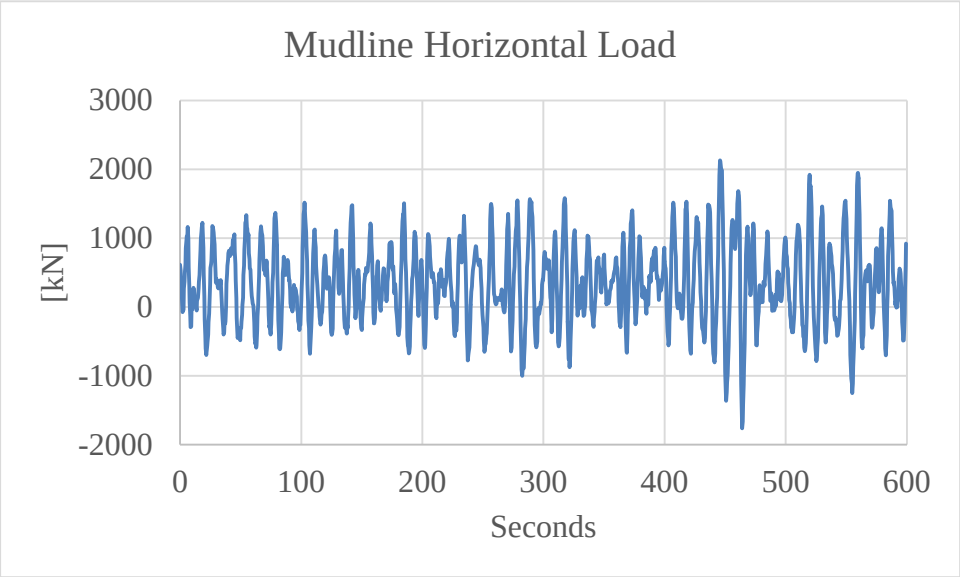

Figure C3.2 Horizontal load time history

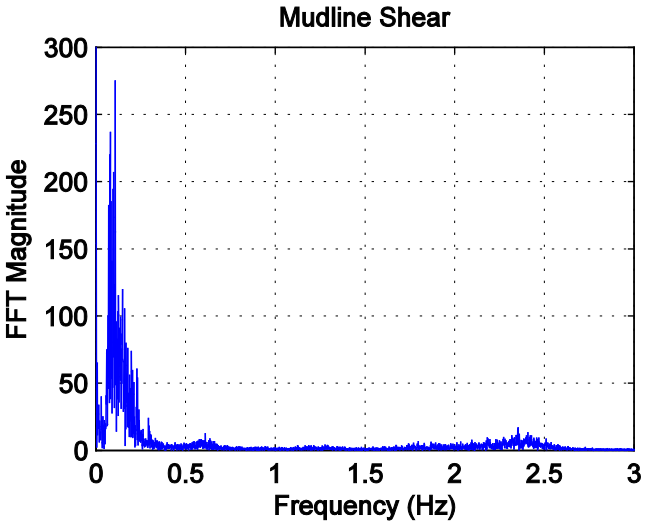

Figure C3.3 Mudline shear spectra

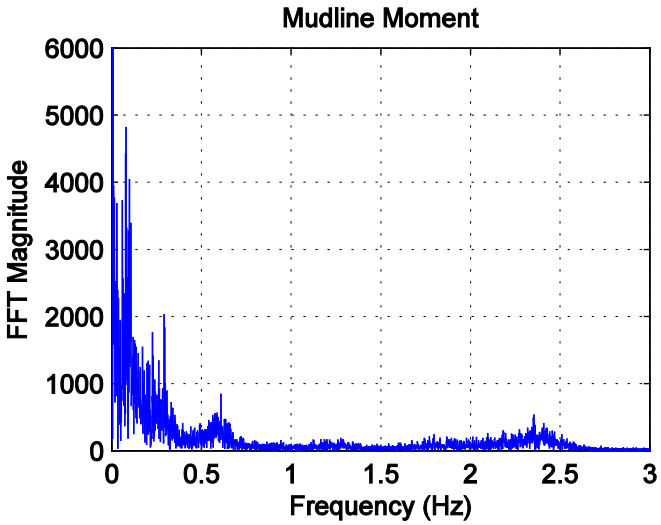

Figure C3.4 Mudline moment spectra

C4 Geometry and material parameters

A monopile with 5.2 m diameter have been used to develop a procedure for establishing stiffness and damping curves for foundation.

Finite element analysis to establish load displacement curves were performed with a geometry, described in detail /1/. The input geometries to the Infidel software is shown in Figure C4.1 and input parameters given in Table C4.1.

A 32 m long pile is embedded in 48m deep soil deposit divided in 3 soil units described in section C4.1.

To the right of the mesh shown in Figure C4.1 the model has infinite elements to account for infinite extent of the soil.

	Information for preparing					Each ring and layer is diveded in 2, resulting in 4 elements in each cell below																										
	Infidel input file for Sheringham Shole monopile																															
Element number	Layer Number in first column	Layer thickness	material	depth below mudline top of layer		Ring Coordinates																										
						1	2	3	4	5	6	7	8	9	10	11	12	13	14	15	16	17	18	19	20	21	22	23	24	25	26	27	28
					Ring number	1		2		3		4		5		6		7		8		9		10		11		12		13		14	
					Ring thickness	1		1		0.6		1		1		1		2		2		2		2		2		3		3		3	
		0			Outer Radius of ring	1.00		2.00		2.60		3.60		4.60		5.60		7.60		9.60		11.60		13.60		15.60		18.60		21.60		24.60	
1					Element number in top row	1	38	75	112	149	186	223	260	297	334	371	408	445	482	519	556	593	630	667	704	741	778	815	852	889	926	963	1000		
2	1	2	3001	0		2	39	76	113	150	187	224	261	298	335	372	409	446	483	520	557	594	631	668	705	742	779	816	853	890	927	964	1001		
3						3	40	77	114	151	188	225	262	299	336	373	410	447	484	521	558	595	632	669	706	743	780	817	854	891	928	965	1002		
4	2	2	3001	2		4	41	78	115	152	189	226	263	300	337	374	411	448	485	522	559	596	633	670	707	744	781	818	855	892	929	966	1003		
5						5	42	79	116	153	190	227	264	301	338	375	412	449	486	523	560	597	634	671	708	745	782	819	856	893	930	967	1004		
6	3	2	3001	4		6	43	80	117	154	191	228	265	302	339	376	413	450	487	524	561	598	635	672	709	746	783	820	857	894	931	968	1005		
7						7	44	81	118	155	192	229	266	303	340	377	414	451	488	525	562	599	636	673	710	747	784	821	858	895	932	969	1006		
8	4	2	3001	6		8	45	82	119	156	193	230	267	304	341	378	415	452	489	526	563	600	637	674	711	748	785	822	859	896	933	970	1007		
9						9	46	83	120	157	194	231	268	305	342	379	416	453	490	527	564	601	638	675	712	749	786	823	860	897	934	971	1008		
10	5	2	3001	8		10	47	84	121	158	195	232	269	306	343	380	417	454	491	528	565	602	639	676	713	750	787	824	861	898	935	972	1009		
11						11	48	85	122	159	196	233	270	307	344	381	418	455	492	529	566	603	640	677	714	751	788	825	862	899	936	973	1010		
12	6	4	3001	10		12	49	86	123	160	197	234	271	308	345	382	419	456	493	530	567	604	641	678	715	752	789	826	863	900	937	974	1011		
13						13	50	87	124	161	198	235	272	309	346	383	420	457	494	531	568	605	642	679	716	753	790	827	864	901	938	975	1012		
14	7	4	3002	14		14	51	88	125	162	199	236	273	310	347	384	421	458	495	532	569	606	643	680	717	754	791	828	865	902	939	976	1013		
15						15	52	89	126	163	200	237	274	311	348	385	422	459	496	533	570	607	644	681	718	755	792	829	866	903	940	977	1014		
16	8	4	3002	18		16	53	90	127	164	201	238	275	312	349	386	423	460	497	534	571	608	645	682	719	756	793	830	867	904	941	978	1015		
17						17	54	91	128	165	202	239	276	313	350	387	424	461	498	535	572	609	646	683	720	757	794	831	868	905	942	979	1016		
18	9	2	3002	22		18	55	92	129	166	203	240	277	314	351	388	425	462	499	536	573	610	647	684	721	758	795	832	869	906	943	980	1017		
19						19	56	93	130	167	204	241	278	315	352	389	426	463	500	537	574	611	648	685	722	759	796	833	870	907	944	981	1018		
20	10	2	3003	24		20	57	94	131	168	205	242	279	316	353	390	427	464	501	538	575	612	649	686	723	760	797	834	871	908	945	982	1019		
21						21	58	95	132	169	206	243	280	317	354	391	428	465	502	539	576	613	650	687	724	761	798	835	872	909	946	983	1020		
22	11	2	3003	26		22	59	96	133	170	207	244	281	318	355	392	429	466	503	540	577	614	651	688	725	762	799	836	873	910	947	984	1021		
23						23	60	97	134	171	208	245	282	319	356	393	430	467	504	541	578	615	652	689	726	763	800	837	874	911	948	985	1022		
24	12	2	3003	28		24	61	98	135	172	209	246	283	320	357	394	431	468	505	542	579	616	653	690	727	764	801	838	875	912	949	986	1023		
25						25	62	99	136	173	210	247	284	321	358	395	432	469	506	543	580	617	654	691	728	765	802	839	876	913	950	987	1024		
26	13	2	3003	30		26	63	100	137	174	211	248	285	322	359	396	433	470	507	544	581	618	655	692	729	766	803	840	877	914	951	988	1025		
27						27	64	101	138	175	212	249	286	323	360	397	434	471	508	545	582	619	656	693	730	767	804	841	878	915	952	989	1026		
28	14	2	3003	32		28	65	102	139	176	213	250	287	324	361	398	435	472	509	546	583	620	657	694	731	768	805	842	879	916	953	990	1027		
29						29	66	103	140	177	214	251	288	325	362	399	436	473	510	547	584	621	658	695	732	769	806	843	880	917	954	991	1028		
30	15	2	3003	34		30	67	104	141	178	215	252	289	326	363	400	437	474	511	548	585	622	659	696	733	770	807	844	881	918	955	992	1029		
31						31	68	105	142	179	216	253	290	327	364	401	438	475	512	549	586	623	660	697	734	771	808	845	882	919	956	993	1030		
32	16	2	3003	36		32	69	106	143	180	217	254	291	328	365	402	439	476	513	550	587	624	661	698	735	772	809	846	883	920	957	994	1031		
33						33	70	107	144	181	218	255	292	329	366	403	440	477	514	551	588	625	662	699	736	773	810	847	884	921	958	995	1032		
34	17	4	3003	38		34	71	108	145	182	219	256	293	330	367	404	441	478	515	552	589	626	663	700	737	774	811	848	885	922	959	996	1033		
35						35	72	109	146	183	220	257	294	331	368	405	442	479	516	553	590	627	664	701	738	775	812	849	886	923	960	997	1034		
36	18	6	3003	42		36	73	110	147	184	221	258	295	332	369	406	443	480	517	554	591	628	665	702	739	776	813	850	887	924	961	998	1035		
37						37	74	111	148	185	222	259	296	333	370	407	444	481	518	555	592	629	666	703	740	777	814	851	888	925	962	999	1036		

Figure C4.1 Input of geometry to Infidel of 32 m long 5.2 m diameter pile

Table C4.1 Monopile parameters

Diameter (D)	5.2 m
Thickness	0.07 m
Embedment Depth	32 m
Young's Modulus	210 GPa

C4.1 Soil profile and input parameters

The soil profile is described in /1/. Below is given the idealized profile used in the analysis.

Input parameters were based on a specific North Sea offshore site. The input parameters for analysis are shown Table C4.2.

The initial shear modulus, G_{max}, is necessary as input for establishing stress-strain curves. The initial shear moduli were computed from shear wave velocities, shown in Figure C4.2. The Poisson's ratios were determined from the shear wave and pressure wave velocities. Undrained shear strengths, plasticity indices, and over consolidation ratios were taken from the specific North Sea offshore site.

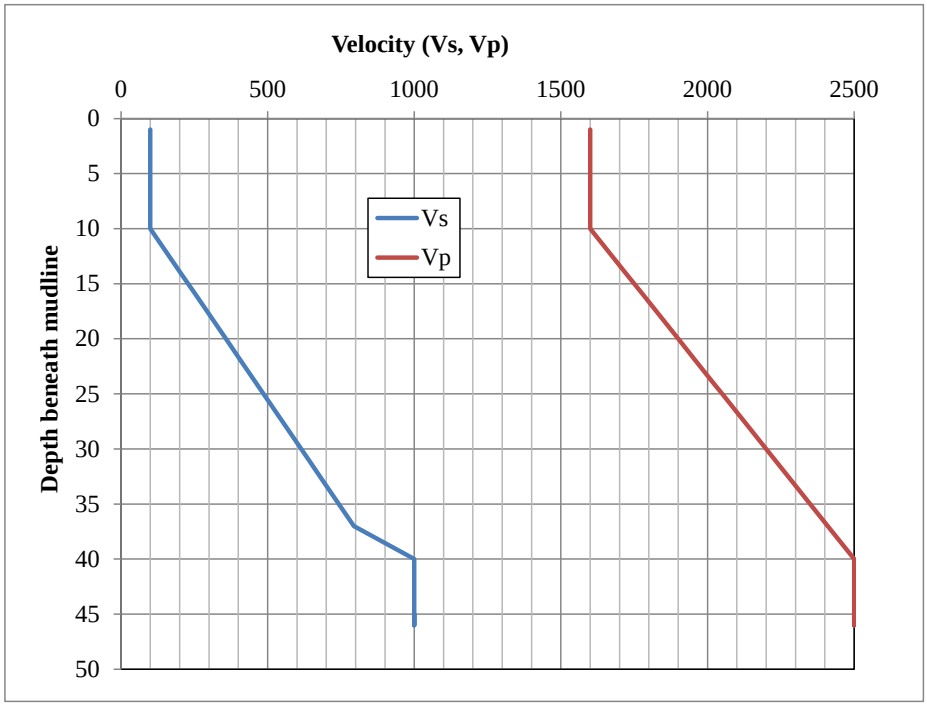

Figure C4.2 Shear and pressure wave velocity profiles used in analysis

Table C4.2 Input-profile for mono-pile for infidel

Layer	Material	Material number	Thickness [m]	Undrained strength [kPa]	Gmax [MPa]	Plasticity Index	OCR	Poisson's ratio
1	Clay	3001	14	33	20	20	10	.498
2	Clay	3002	10	125	100	20	10	.490
3	Clay	3003	24	500	600	20	10	.470

C4.2 Clay stiffness, stress and damping vs. shear strain

Based on the established soil profile given in Table C4.2 and a loading frequency of 0.3 Hz, curves for shear modulus reduction and damping versus shear strain were established based on equations given in /3/. The modulus reduction and damping curves are slightly pressure dependent. At 0.03% shear strain for a confining pressure varying from 30 kPa to 300 kPa, the variation in modulus reduction is of the order of 20%. Since this variation is small compared to the variation in shear modulus and strength of the materials, the same modulus reduction curves (see Figure C4.3) were used for the three different materials in the model. At 0.1% shear strain for a confining pressure varying from 30 kPa to 300 kPa, the damping ratio varies from 8% to 12%. For simplicity the same damping curve (shown in Figure C4.4) were used for the three different materials. The resulting stress-strain curves are shown in Figure C4.5.

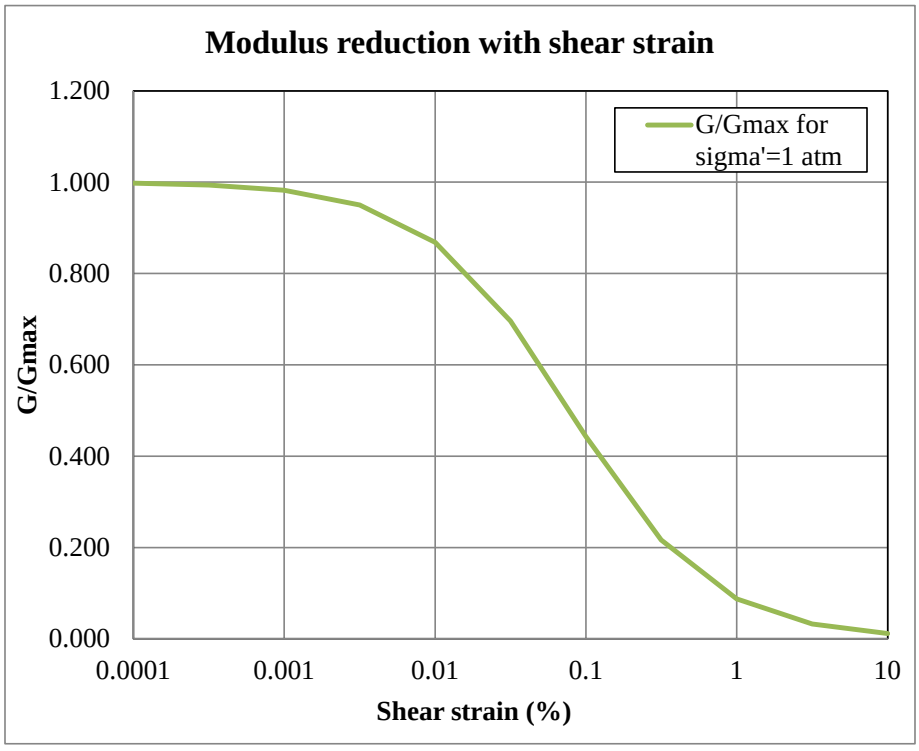

Figure C4.3 Modulus reduction curves for all materials

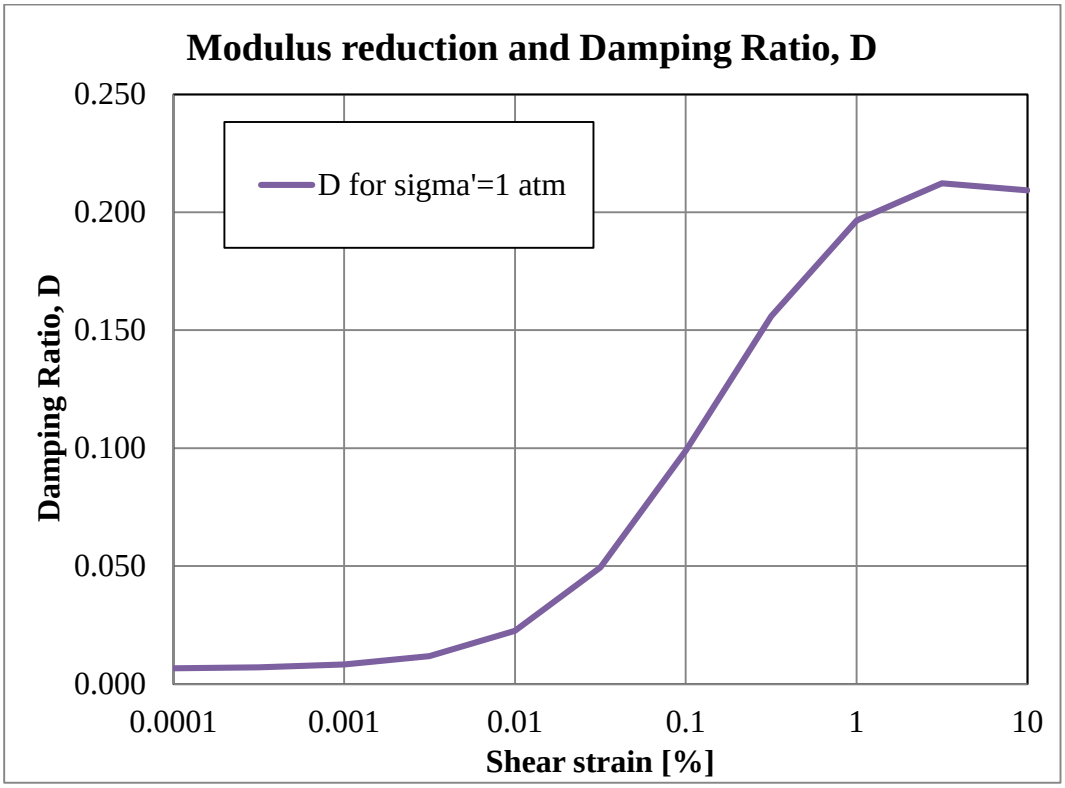

Figure C4.4 Damping vs. shear strain for used for all material layers

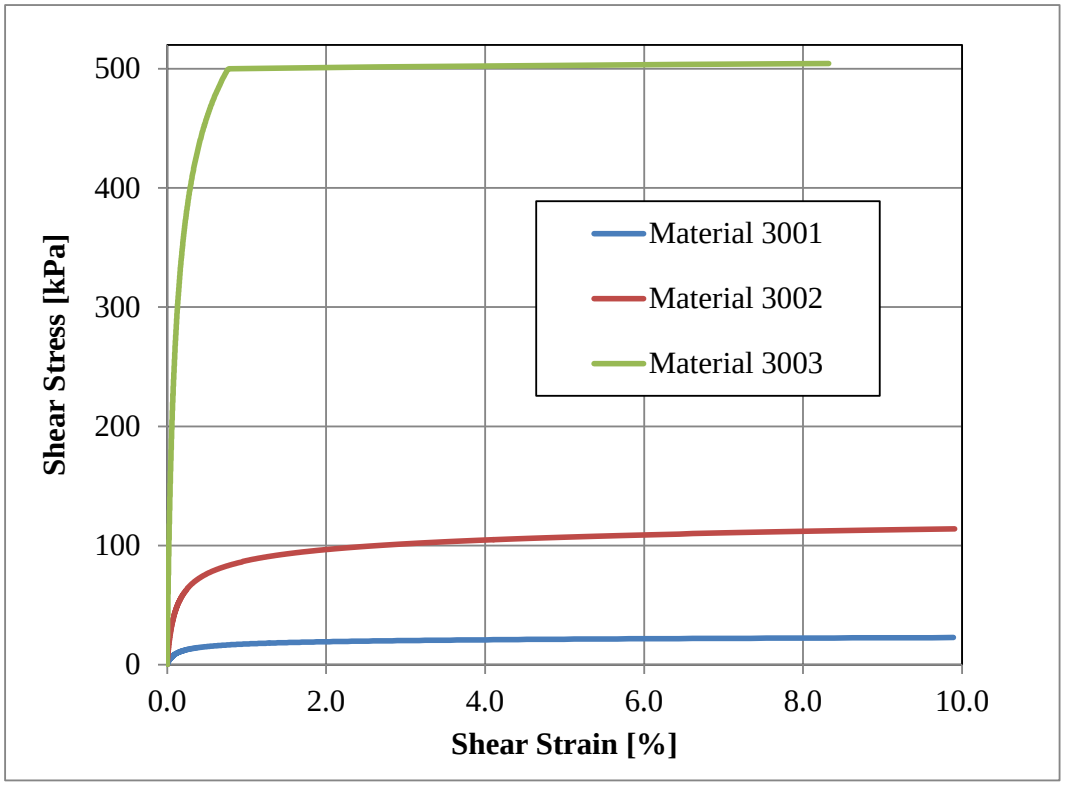

Figure C4.5 Shear stress vs. shear strain for all materials

C5 Infidel Analysis Results

Stiffness and damping for the monopile foundation results from the Infidel analysis are presented below.

Figure C5.1 shows a distribution of shear stress mobilization , i.e. ratio between maximum shear stress and shear strength, at maximum load level.

Figure C5.2 and Figure C5.3 show mudline moment and horizontal loads versus computed mudline horizontal cyclic displacement.

The computed damping factor (defined in section C2.1.1) increases with displacement as seen Figure C5.4. The increase is reduces as displacement increases and reaches 4% at a displacement of 2.6 cm which is about 0.5% of the diameter of the monopile.

The damping do not increase as quickly with displacement as the moment and horizontal load. This is due to the increase in elastic energy is larger than the increase in hysteretic energy as can be seen in Figure C5.5.

Figure C5.6 shows the horizontal and vertical cyclic displacement along a vertical section in the soil directly to the right of the monopile.

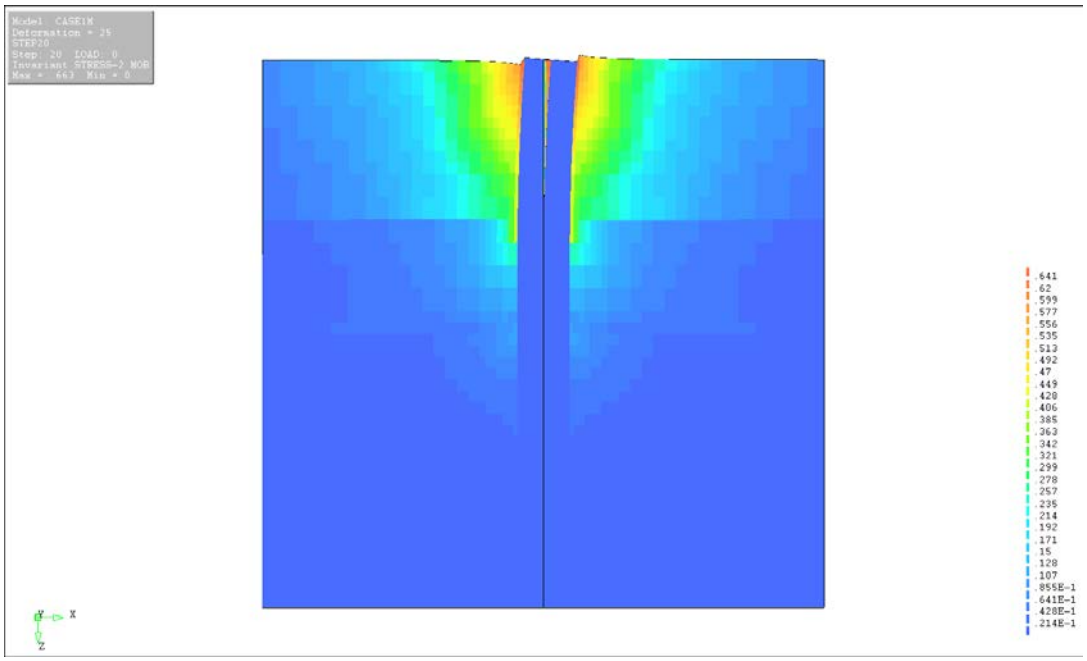

Figure C5.1 Distribution of shear stress mobilization , i.e. ratio between maximum shear stress and shear strength

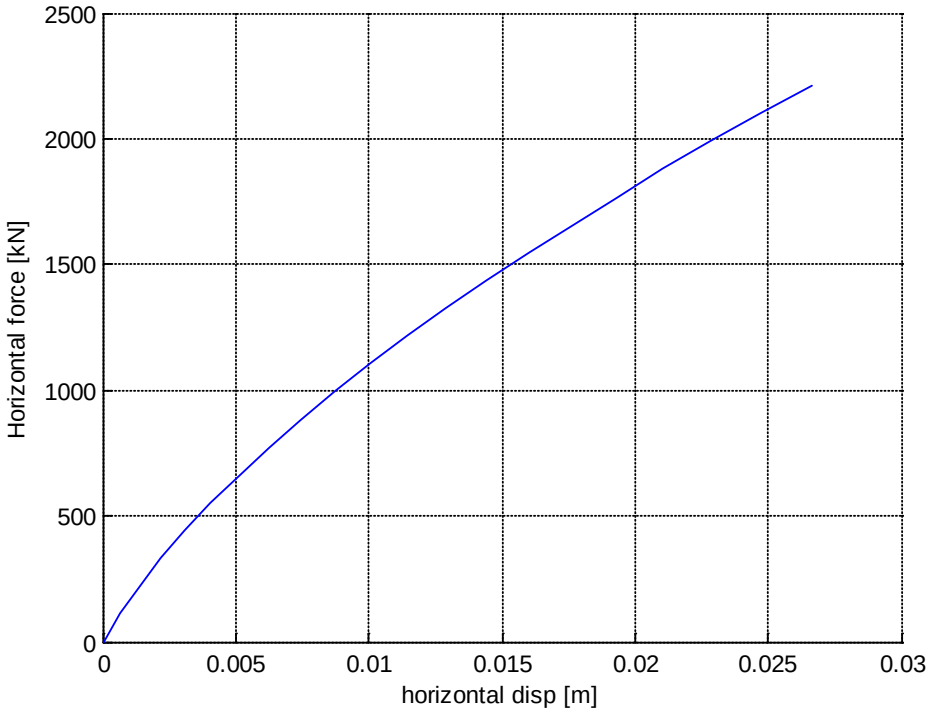

Figure C5.2 Mudline horizontal cyclic load versus horizontal cyclic displacement amplitude

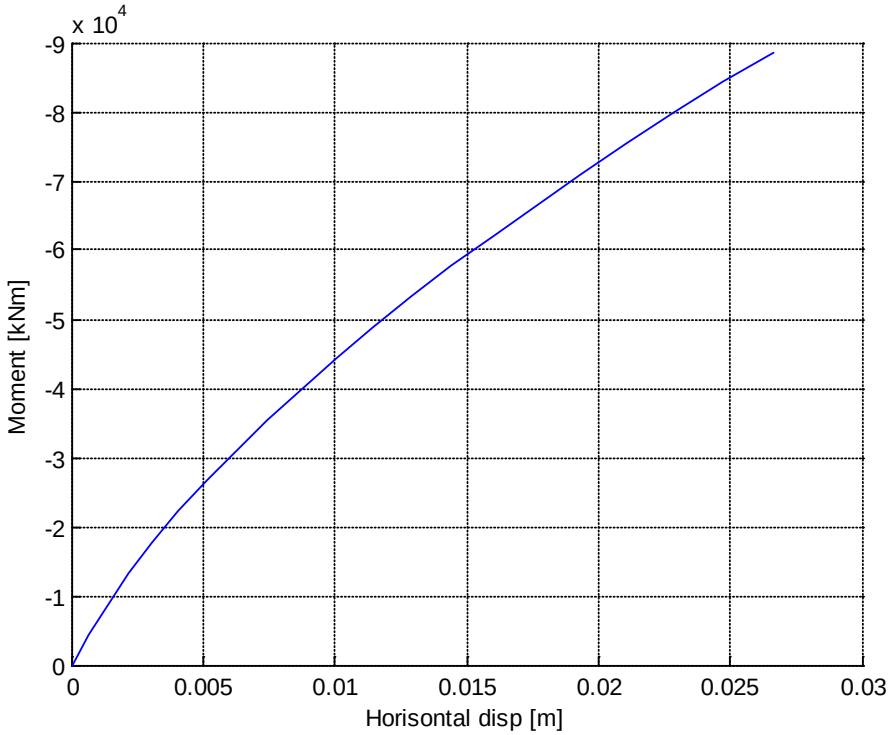

Figure C5.3 Mudline cyclic moment versus horizontal cyclic displacement amplitude

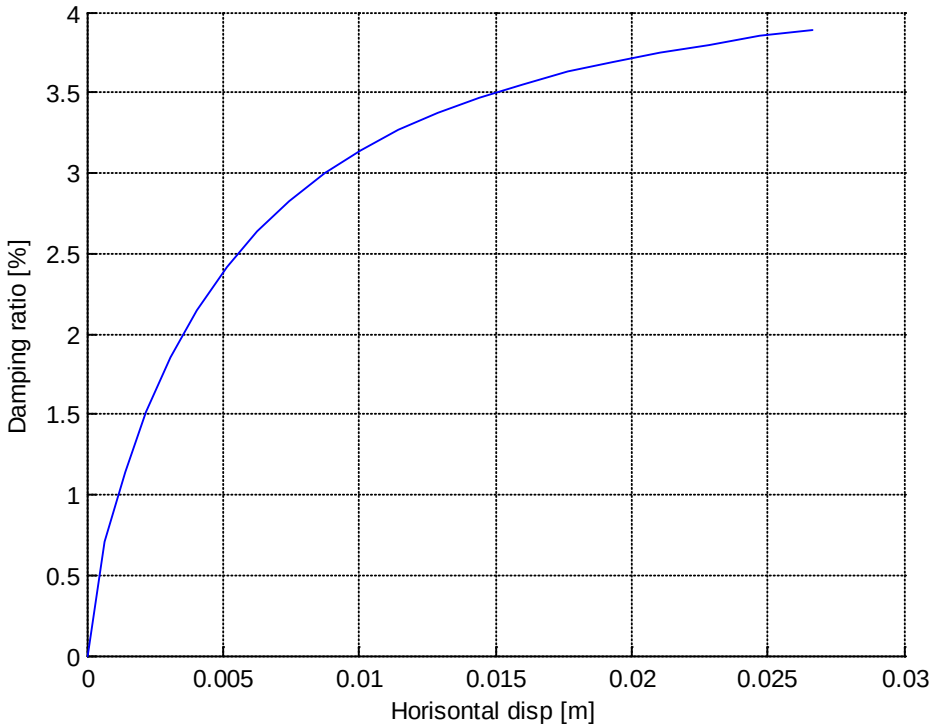

Figure C5.4 Foundation hysteretic damping ratio versus horizontal cyclic displacement amplitude

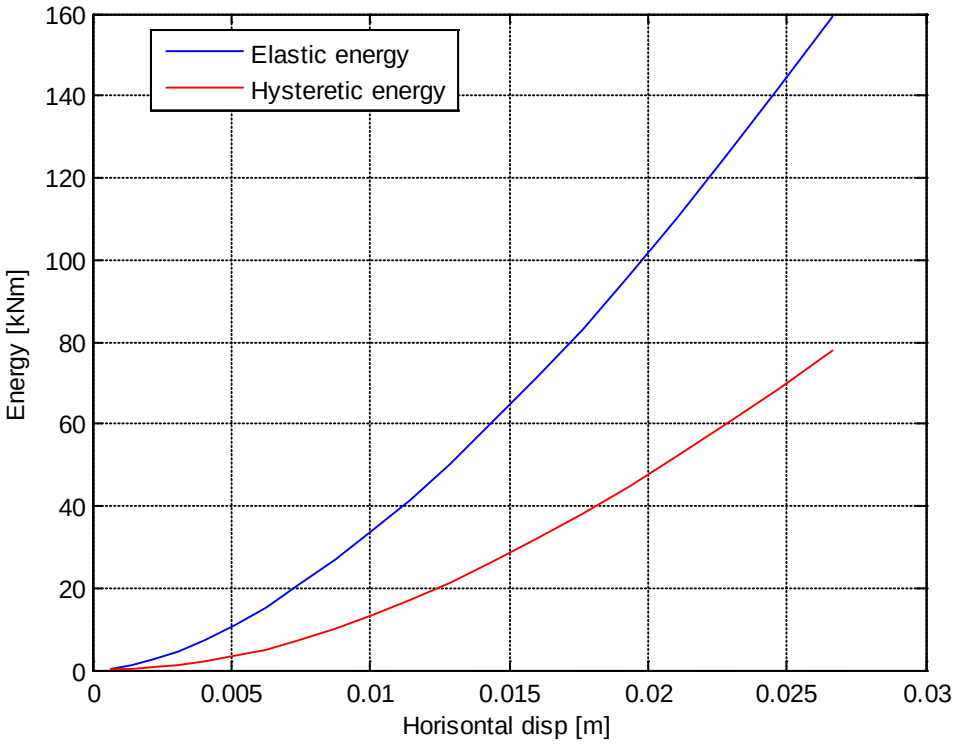

Figure C5.5 Elastic and Hysteretic energy versus cyclic displacement amplitude

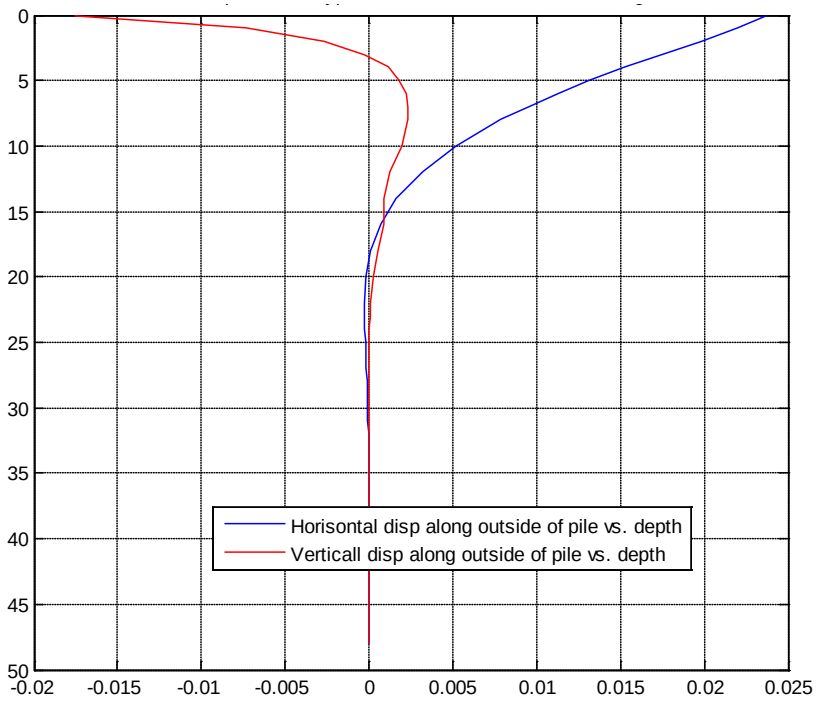

Figure C5.6 Horizontal axis showing horizontal and vertical displacements in soil just outside of pile. Vertical axis the depth beneath mudline. Positive displacement values means displacement downward and to the right. Units in meters.

C6 Computation of 2x2 stiffness matrix

Establishing a 2x2 stiffness matrix for coupling between horizontal and moment stiffness for a nonlinear foundation response is not strictly unique. However, an approximation has been made to establish this for comparison with rigorous elastic solutions computed with the software Piles /5/.

C6.1 Uncoupled stiffness

The global foundation stiffness in 2D can often be represented a 2 by 2 stiffness matrix at the mudline given as

$$K = \begin{bmatrix} k_{xx} & k_{x\theta} \\ k_{\theta x} & k_{\theta\theta} \end{bmatrix}$$

where k_{xx}, is the horizontal stiffness, $k_{x\theta}$, is the coupling term between horizontal translationa and rotiation, and $k_{\theta\theta}$ is the rotational stiffness around the horizontal y-axis. A right handed coordinate system with z-axis positive in the downward vertical direction is used.

For easier implementation in some structural engineering software, such a 2 by 2 stiffness matrix can also be represented by an uncoupled horizontal and rotational stiffness. The main results of the derivation is summarized below.

By defining a decoupling point for a rigid connection to the mudline with a bar of length, l, given by

$$l = \frac{k_{x\theta}}{k_{xx}},$$

the uncoupled stiffness, K' become,

$$K' = \begin{bmatrix} k'_{xx} & 0 \\ 0 & k'_{\theta\theta} \end{bmatrix}$$

where the horizontal translational stiffness is

$$k'_{xx} = k_{xx},$$

and the rotational stiffness at the decoupling point is

$$k'_{\theta\theta} = k_{\theta\theta} - k_{x\theta} l.$$

By applying a horizontal load, H, and a moment, M, to the foundation at the mudline and obtaining the corresponding displacement, u, and rotation, θ, at the mudline, the horizontal stiffness is computed as

$$k'_{xx} = k_{xx} = \frac{H}{u + l\theta}$$

and the rotational stiffness as

$$k'_{\theta\theta} = \frac{M - lH}{\theta}.$$

The decoupled horizontal and rotational stiffness, representing the foundation and soil stiffness, can be used directly as a translational and a rotational spring attached to a rigid element of length, l, connected to the superstructure.

One difficulty in using the above procedure is due to the nonlinear response the decoupling length varies with loading. An approximate procedure, while not documented here, is available.

C6.2 Dashpot values

For use in structural analysis models, equivalent viscous dashpot coefficients, c, can be established from the damping ratios shown in Figure C5.4 by using equations below.

It is assumed that moment and horizontal load is in correspondence such the total hysteretic energy loss can be modelled with a dashpot at the mudline. For a rotation at the mudline (or at the decoupling point) $\theta = \theta_0 \sin \omega t$, the energy loss in the dashpot is

$$E_d = c\omega\theta_0^2\pi$$

Where $\omega = 2\pi f$ and θ_0 is the rotation amplitude, and f is the loading frequency, which can be estimated from the Fourier spectra of the loads.

Setting the energy loss in the dashpot equal to the hysteretic energy loss, E_h, computed in the Infidel analysis gives

$$c = \frac{E_h}{2\theta_0^2\pi^2 f}$$

The resulting foundation dashpot coefficient is then dependent on the 1) load level (since hysteretic energy, E_h, varies with load level, 2) the cyclic rotation amplitude and 3) the vibration frequency. A few runs/iterations of the structural dynamic analysis may be needed to determine an appropriate dashpot value for a specific load level, rotation amplitude and frequency.

C7 Summary and recommendations

Foundation load dependent damping values were computed for wave and wind induced loads on an offshore wind turbine monopile foundation. The computed damping values are valid for the specific combination of loads (moment and horizontal) and load level used in the analysis above. Vertical loading has not been considered in this study. Using the computed stiffness and damping values outside of the give load range may not be correct. The obtained damping ratios can be converted to dashpot coefficients, c, with equations given in Section C6.2, for a horizontal dashpot at the seabed level to be included in a time history analysis. This is valid as long as moment and horizontal loading are in phase. The resulting foundation dashpot coefficient is dependent on the load level (since hysteretic energy varies with load level), the cyclic rotation amplitude and the vibration frequency.

Site specific laboratory- or in-situ determined material parameters such shear modulus and damping for the soils can reduce the uncertainties in the estimated stiffness and damping values.

It is important to gain more the understanding of how the nonlinear behaviour of foundation response affects the overall response of the structure. Further studies with simple models accounting for soil nonlinearity is recommended. It is important to find out whether mudline rotational stiffness and damping are more important than horizontal stiffness and damping for controlling the overall behaviour of the structure. The coupling between moment and horizontal stiffness are likely an important parameter.

A number of parameters affecting the computed (mono-pile) global foundation stiffness and damping. A sensitivity study can improve the understanding influence of parameters such as load-levels, frequency of loading, variations in the material stiffness and damping curves with depth, element-size in the soil in and around the foundation, installation effects, cyclic degradation due to multiple load cycles, and erosion (scour) at mudline.

C8 References

/1/ NGI Report, 20110186-00-1-R, Soil Structure Interaction for OWT monopile foundation, December 2011.

/2/ Andersen, K.H.;Lunne, T.;Kvalstad, T.J.;Forsberg, C.F., Deep water geotechnical engineering. Ingenieria geotéchnica en aguas profundas. Reunión Nacional de Mecánica de Suelos, 24. Aguascalientes, Mexico 2008. Proceedings, Vol. Especial, pp.209-265. Also publ. in: Norwegian Geotechnical Insitute, Oslo. Publication 208. Aguascalientes; 2008.

/3/ Darendeli M. B., Development of a new family of normalized modulus reduction and material damping curves, Ph.D. Dissertation, The University of Texas at Austin, August, 2001.

/4/ Wystan Carswell, Personal Communicaition, Dropbox\Soil Damping\08a_Infidel Model_WC.docx, 2013

/5/ Kaynia A.M., 1982, Dynamic Stiffness and response of Pile Groups, Research Report R82-03, Dept. of Civil Eng., M.I.T.

/6/ Gazetas, George, Foundation Vibrations, Ch. 15, Foundation Engineering Handbook, 2nd ed. , Ed Hsai Yang Fang, 1990

/7/ NWTC Computer-Aided Engineering Tools (FAST by Jason Jonkman, Ph.D.). http://wind.nrel.gov/designcodes/simulators/fast/. Last modified 28-October-2013; accessed 16-January-2014.

/8/ Wystan Carswell, Personal Communication, Ph.D. candidate at the University of Massachusetts, 2013/14.

Appendix D - Soil Structure Interaction for OWT monopile foundations

UNIVERSITY OF MASSACHUSETTS AMHERST

Soil Damping Impacts for Offshore Wind Towers

Soil Structure Interaction for OWT monopile foundations

Wystan Carswell

Ph.D. Candidate
Civil & Environmental Engineering
University of Massachusetts Amherst

25 October 2013

This work was in collaboration with Jörgen Johansson, Finn Løvholt at NGI as well as Sanjay Arwade and Don DeGroot at UMass Amherst.

Contents

1 Introduction

The purpose of this study was to determine the effects of soil damping on offshore wind turbines (OWTs) support structures. Due to the tight financial margins of most offshore wind projects, state-of-the-art research trends toward large (e.g. 5-10MW) offshore wind turbines (OWTs). Fatigue is often a design driver for these large OWTs, necessitating a thorough examination of damping sources: aerodynamic, hydrodynamic, structural, and soil. Of these sources, soil damping has been least considered by researchers with respect to OWTs.

Two-dimensional structural models of the NREL 5MW Reference Turbine and SWT-3.6-107 offshore wind turbines were created in ADINA using Euler-Bernoulli beam elements and a concentrated tower top mass to represent the rotor-nacelle assembly. In order to mitigate computational expense, a linear, reduced-order foundation model was used to represent monopile foundations. Springs and dashpots were used to represent soil-pile stiffness and damping.

Using free vibration analysis, it was determined here that soil damping can contribute 0.4-0.7% to global structural damping (an updated model, Carswell et al., submitted, indicates as much as 1.5%). Stochastic time history analysis demonstrated a reduction in some frequency content.

2 Literature

Several researchers have back-calculated soil damping contributions for OWTs using instrumented "rotor-stop" free vibration data [1, 2]. In these cases, a structural model of the OWT was produced to match natural frequency and the identified sources of damping (structural, hydrodynamic, aerodynamic) were added to the model, and the remaining amount of global damping (ξ) was assumed to be from soil. Tarp-Johansen et al. (2009) used a three-dimensional finite element model to determine soil strain levels and corresponding amounts of damping [3]. The results of these studies can be seen in Table 1.

Table 1 Offshore Wind Turbine Damping Contributions

	Damgaard et al. (2012)	**Versteijlen et al. (2011)**	**Tarp-Johansen et al. (2009)**
ξ_{steel}	0.19%		0.19%
ξ_{hydro}	0.12%	1.5%	0.23%
ξ_{aero}	0.062%		0.08-0.23%
ξ_{soil}	0.58%	1.5%	0.49-0.62%

3 Description of ADINA Structural Model

ADINA [4] is a commercially available finite element program which was used in this study for structural analysis. The two-dimensional structural models were comprised of beam elements, with the eneral properties of the NREL 5MW Reference Tower [5] and the SWT-3.6-107 [6, 2] in Table 2.

Table 2. Offshore Wind Turbine Structural Models

Property	**NREL 5MW**	**SWT-3.6-107**
Rating	5 MW	3.6MW

Cut-in, Rated, Cut-out Wind Speed	3 m/s, 11.4 m/s, 25 m/s	3-5 m/s, 13-14 m/s, 25 m/s
Hub Height	90 m	81.75 m
Rotor Diameter	126 m	107 m
Tower Base Diameter, Wall Thickness	6 m, 0.035 m	5 m, 0.030 m
Tower Top Diameter, Wall Thickness	3.87 m, 0.025 m	3.12 m, 0.021 m
Nacelle & Rotor Mass	350 t	142 t
Tower Mass	347.460 t	92.5 t
Mean Sea Level	20 m	20 m
Pile Diameter, Wall Thickness	6 m, 0.070 m	5.2 m, 0.065 m
Pile Embedment Depth	38.9 m	29.25 m
Soil Type	Medium dense to dense sand	Stiff to hard clay
Steel Modulus (E)	210 GPa	
Density of Steel (ρ)	8500 kg/m^3	

The NREL 5MW tower tapers linearly from mean sea level (MSL) to tower top, with a constant substructure diameter and thickness (6 m and 0.07 m). The SWT-3.6-107 (SWT) tower was informed by an example tower specification from Siemens [2] and the substructure was specified according to the monopile foundation model information for Sheringham Shoal (2011-0186).

4 Reduced-Order Foundation Model

Reduced-order foundation models for OWTs are often used to mitigate computation cost in time history analysis. The mudline stiffness matrix K_{mud} is the simplest of these reduced-order models, with

$$K_{mud} = \begin{bmatrix} k_{xx} & k_{xm} \\ k_{mx} & k_{mm} \end{bmatrix}$$

where the subscript x refers to the horizontal translation and the m refers to the rotational degree of freedom (torsion was neglected).

It was not possible to define a mudline stiffness matrix at a node in ADINA, so an equivalent pile model derived by Kristoffer Skau was used to produce K_{mud} (Figure 1).

Figure 1 Equivalent Foundation Model

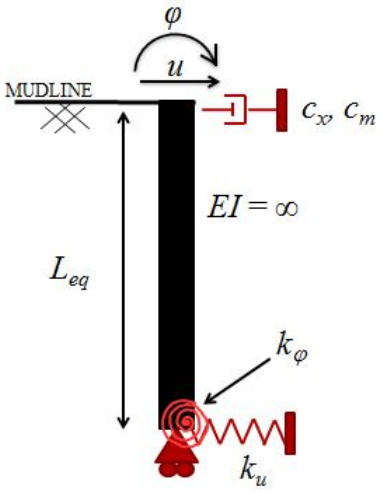

The equivalent pile model is defined by an equivalent rigid length

$$L_{eq} = -\frac{k_{xm}}{k_{xx}} \quad (1)$$

And is supported by a translation and rotation spring, where translation spring stiffness $k_u = k_{xx}$ and rotation spring stiffness

$$k_\varphi = k_{mm} - k_{xm}L_{eq} \quad (2)$$

Material soil damping was modeled using mudline dashpots c_x and c_m in the translation and rotation degrees of freedom (DOFs), respectively. Radiation damping is typically considered negligible for load frequencies below 1 Hz; a Fast Fourier Transform (FFT) of the mudline moment time history from the aeroelastic code FAST [7] indicates that the majority of the loading for the NREL 5MW (and most OWTs) is below 1 Hz (Figure 2).

Figure 2 Fourier Transform of NREL 5MW Mudline Moment under Wind and Wave Loading in Operating Conditions (18 m/s wind, 5 m wave, 7.2 wave period)

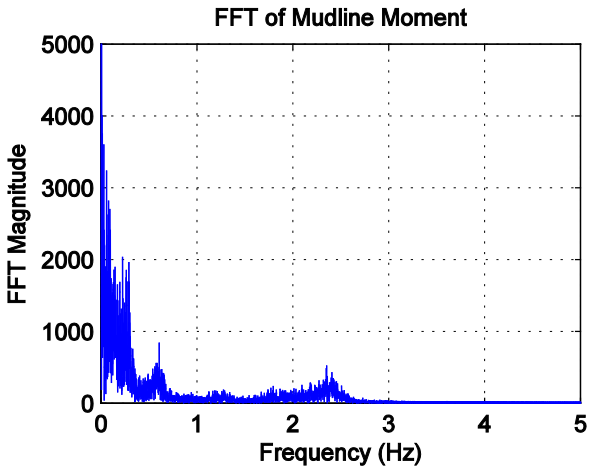

4.1 Mudline Stiffness Matrix from Piles

K_{mud} for the SWT was taken from the Sheringham Shoal results of the NGI elastodynamic in-house program Piles, which computes stiffness and damping of piles based on discrete Green functions [8].

The dashpot damping value c is defined by the complex dynamic mudline stiffness K^* for the pile,

$$K^* = K_{mud}(1 + i\omega C) \quad \textbf{(3)}$$

where i is imaginary, ω is the loading frequency in rad/sec, and C is the viscous damping matrix

$$C = \begin{bmatrix} c_{xx} & c_{xm} \\ c_{mx} & c_{mm} \end{bmatrix} \quad \textbf{(4)}$$

4.2 Mudline Stiffness Matrix from P-y Method in Sand

K_{mud} for the NREL 5MW was determined using a Winkler-type distributed spring foundation in medium dense to dense sand (Table 3, [9]). The soil springs were defined using the API *p-y* method [10].

Table 3 Distributed Spring Model Input

Symbol	Property	Value
γ'	Submerged Unit Weight	10 kN/m^3
D_R	Relative Density	0.55
k	Initial Modulus of Subgrade Reaction	20,800 kN/m^3
φ'	Friction Angle	40°
b	Pile Diameter	6 m
d	Pile Depth	38.9 m
t	Wall Thickness	0.07 m

K_{mud} can be calculated using the inverse of the mudline flexibility matrix f_{mud} which was found from the displacement matrix created by applying unit loads to the pile head at the mudline (

Table 4).

Table 4 Distributed Spring Flexibility Test Results

Horizontal Force (N)	Moment (Nm)	Translation, u (m)	Rotation, φ (rad)
1	0	1.449e-009	-1.077e-010
0	1	-1.077e-010	1.300e-011

Mudline dashpot values were assumed to be proportional to stiffness, so the ratio between K_{mud} and C found in the Piles method was used to determine dashpot values (i.e., $C = \%K_{mud}$).

4.3 Added Hydrodynamic Mass

Added hydrodynamic mass was incorporated in the OWT substructures as a way to represent hydrodynamic interaction effects. A simplified method for calculating added hydrodynamic mass for cylindrical towers was derived per Goyal & Chopra (1989) where

$$m_t = m_{str} + m_o + m_i \tag{5}$$

where m_t is the total mass, m_{str} is the mass contributed directly by the structural cross-section, m_o is the added mass from the water surrounding the substructure, and m_i is the mass from the water inside the substructure. These latter two masses are further defined by:

$$m_o(z) = \rho_w \pi r_o^2 \left[\frac{16 H_o}{\pi^2 r_o} \sum_{j=1}^{\infty} \frac{(-1)^{j-1}}{(2j-1)^2} E_j \cos\left(\alpha_j \frac{z}{H_o}\right) \right] \tag{6}$$

where z is the distance above the mudline, H_o is the depth of the water surrounding the substructure (MSL), ρ_w is the mass density of water, r_o is the outside of radius of the tower,

$$\alpha_j = \frac{(2j-1)\pi}{2} \tag{7}$$

and E_j is a function of $\alpha_j r_o / H_o$ where

$$E_j = \frac{K_1\left(\alpha_j \frac{r_o}{H_o}\right)}{K_0\left(\alpha_j \frac{r_o}{H_o}\right) + K_2\left(\alpha_j \frac{r_o}{H_o}\right)} \tag{8}$$

where K_n is the modified Bessel function of order n of the second kind. Similarly, for the added hydrodynamic mass inside the substructure,

$$m_i(z) = \rho_w \pi r_i^2 \left[\frac{16 H_i}{\pi^2 r_i} \sum_{j=1}^{\infty} \frac{(-1)^{j-1}}{(2j-1)^2} D_j \cos\left(\alpha_j \frac{z}{H_i}\right) \right] \tag{9}$$

H_i is the depth of the surrounding water (sea water level), r_i is the outside of radius of the tower, and D_j is a function of $\alpha_j r_i / H_i$ where

$$D_j = \frac{I_1\left(\alpha_j \frac{r_i}{H_i}\right)}{I_0\left(\alpha_j \frac{r_i}{H_i}\right) + I_2\left(\alpha_j \frac{r_i}{H_i}\right)} \tag{10}$$

Where I_n is the modified Bessel function of order n of the first kind.

The equations given for m_o and m_i assume a uniform circular cylinder and were obtained from an analytical solution of the Laplace equation.

Added hydrodynamic mass per substructure element was calculated at the mean elevation of each element measured from the mudline, then divided by substructure cross-sectional area and included in the definition of material density for substructure elements (which were unique per element to take into account the change in added hydrodynamic mass with depth).

4.4 Rayleigh Damping

Structural damping is often assumed to be in the range of 1-2%. Rayleigh structural damping of 1.00% was assumed in this case to align with the general 1.0% damping assumption made in FAST. Rayleigh structural damping is defined by the terms α and β as

$$\xi_{rayl} = \frac{\alpha}{2\omega_n} + \frac{\beta\omega_n}{2} \quad \textbf{(11)}$$

where ξ_{rayl} is the global damping ratio due to Rayleigh structural damping, ω_n is the natural frequency in rad/s, and α and β are selected to provide the desired level of global damping for the first and second modes of vibration.

The tower and substructure of the OWT were assumed to have the same ξ_{rayl}; however, the substructure would likely have a slightly higher damping ratio assuming a grouted transition piece.

For small amounts of damping, it is permissible to model each source separately and sum the resulting values to determine total global damping. For a fatigue analysis, all sources of damping would need to be quantified; however, the goal of this study was to determine the impact of soil damping in particular on OWT behavior, so aerodynamic and hydrodynamic damping were neglected.

5 Methods of Analysis

In order to assess the effects of soil damping on OWTs, the approach was as follows:

- Quantify the portion of global damping attributed to soil using the decay of a free vibration analysis
- Determine the decrease in maximum mudline moment from stochastic time history analysis

Quantifying the global damping attributed to soil allows for the for comparison to other sources of damping, while the stochastic time history analysis gives an indication of potential savings due to soil damping.

5.1 Free Vibration Analysis

The free vibration analysis of the OWTs was conducted in ADINA. The tower top of the OWT was slowly displaced 0.1 m over the course of 10 seconds (more than two structural periods), held at 0.1 m for 5 seconds to reduce transient vibration, then released to allow the OWT to vibrate freely (Figure 3).

Figure 3 Example Free Vibration Analysis

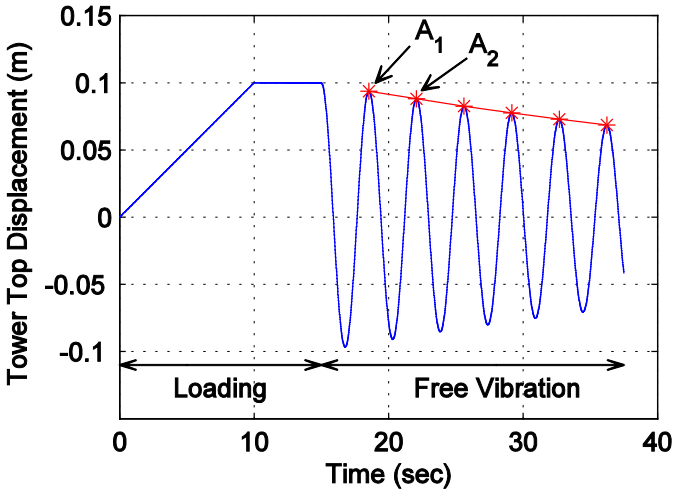

The log decrement method was used to determine the global damping ratio, where the log decrement δ is calculated by

$$\delta = \frac{1}{n}\ln\left(\frac{A_1}{A_2}\right) \tag{12}$$

where A_1 and A_2 are two successive amplitudes n periods apart. A log fit using least squares regression was used for multiple successive amplitudes in order to best estimate δ. From δ, the global damping ratio (ξ) can then be estimated by

$$\xi = \frac{1}{\sqrt{1 + (2\pi/\delta)^2}} \tag{13}$$

5.2 Stochastic Time History Analysis

A preliminary stochastic time history analysis in ADINA was performed using only wind loads. A tower top time history of 120 seconds of 55 m/s winds was generated for the NREL 5MW reference turbine using FAST (10 m/s above cut-out wind speed). The tower top shear and moment history due to 55 m/s winds was then applied to the tower top node of the SWT model in ADINA, despite the fact that the same wind speed would generate different loads on the smaller SWT. Wave loads were not included in the stochastic ADINA analysis.

The objective of the stochastic time history analysis was to identify either

- Maximum mudline moment reduction (corresponding generally to lower design moments)
- Damping of higher frequency loading

6 Results

The results of the free vibration analysis for the NREL 5MW and SWT vary by a factor of 2 (Table 5).

Table 5 Free Vibration Analysis Results

	Offshore Wind Turbine Model	
	NREL 5MW	**SWT**
k_{xx} (GN/m)	1.798	2.346
k_{mm} (GNm/rad)	200.4	154.5
c_{xx} (MN-s/m)	29.88	38.99
c_{mm} (MNm-s/rad)	931.6	718.3
Eigenfrequency (f_1)	0.2499 Hz	0.2826 Hz
Frequency from Time History (f_1)	0.2500 Hz	0.2826 Hz
ξ_{soil}	0.73%	0.41%

The NREL 5MW dashpot values c_{xx} and c_{mm} were selected as a proportion of K_{mud}, which was determined by the initial stiffness of *p-y* curves. If K_{mud} had been calculated more accurately (such as the method which was used for the SWT), the NREL 5MW would likely be less stiff and have lower dashpot damping values.

7 Conclusions and Recommendations

Free vibration analysis yielded a range of ξ_{soil} = 0.41-0.73%, which is approximately in the range of results from literature [1, 3, 11]. It should be noted that the value of ξ_{soil} is very sensitive to analysis assumptions and further research is required to identify the sources of sensitivity (e.g., length of displacement loading time, length of displacement hold to reduce transience, reduced-order foundation model choice, dashpot values, etc.). In non-operating OWT conditions, this amount of damping may be significant when compared to the small amounts of aero- and hydrodynamic damping available when the OWT is parked.

Stochastic time history analysis could be much improved by appropriate wind loading (the NREL 5MW wind loads were used for the smaller SWT), the inclusion of wave loading, and consideration of multiple load cases. The stochastic analysis performed indicated that the magnitude of the frequency content around the natural period of the structure was reduced, but no further conclusions could be made in terms of OWT fatigue life. A more sophisticated assessment of soil damping impact could be performed using FAST, in which the mudline stiffness and damping matrix (6x6) can be input directly into the program (though a recompile is necessary once these changes are made). Various load cases could be examined in FAST, and the net effect of soil damping under stochastic conditions could be better determined.

To make definitive comments on the importance of soil damping, a full fatigue analysis would be necessary in order to assess whether soil damping makes a significant impact on the fatigue life of the OWT; however, the results of this study indicate that soil damping may have meaningful contribution to OWT design.

8 References

[1] M. Damgaard, J. K. Andersen, L. B. Ibsen and L. V. Andersen, "Natural Frequency and Damping Estimation of an Offshore Wind Turbine Structure," in *International Offshore and Polar Engineering Conference*, Rhodes, Greece, 2012.

[2] W. G. Versteijlen, Interviewee, *Personal Communication*. August 2013.

[3] N. J. Tarp-Johansen, A. C. Meyers, L. Andersen, E. D. Christensen, C. Mørch, B. Kallesøe and S. Frandsen, "Comparing Sources of Damping of Cross-Wind Motion," in *European Offshore Wind 2009: Conference & Exhibition: 14-16 September*, Stockholm, Sweden, 2009.

[4] ADINA, ADINA R&D, Inc., 2012.

[5] J. Jonkman, S. Butterfield, W. Musial and G. Scott, "Definition of a 5-MW Reference Wind Turbine for Offshore System Development," National Renewable Energy Laboratory, Golden, CO, 2009.

[6] Siemens, "Wind Turbine SWT-3.6-107," 2011. [Online]. Available: http://www.energy.siemens.com/us/en/renewable-energy/wind-power/platforms/g4-platform/wind-turbine-swt-3-6-107.htm. [Accessed 1 October 2013].

[7] *FAST*, National Renewable Energy Laboratory, 2013.

[8] A. M. Kania and E. Kausel, "Dynamic behaviour of pile groups," in *Proceedings of the 2nd International Conference on Numerical Methods in Offshore Piling*, University of Texas at Austin, 1982.

[9] K. Lesny, S. G. Paikowsky and A. Gurbuz, "Scale Effects in Lateral Load Response of Large Diameter Monopiles," in *Geo-Denver*, Denver, CO, 2007.

[10] API, "Recommended Practice for Planning, Designing, and Constructing Fixed Offshore Platforms - Working Stress Design," American Petroleum Institute, Washington, D.C., 2005.

[11] W. G. Versteijlen, A. Metrikine, J. S. Hoving, E. H. Smidt and W. E. De Vries, "Estimation of the vibration decrement of an offshore wind turbine support structure caused by its interaction with soil," in *EWEA Offshore Conference*, Amsterdam, the Netherlands, 2011.

[12] J.-S. Chiou and C.-H. Chen, "Exact equivalent model for a laterally-loaded linear pile-soil system," *Soils and Foundations,* vol. 47, no. 6, pp. 1053-1061, December 2007.

[13] A. Goyal and A. K. Chopra, "Simplified evaluation of added hydrodynamic mass for intake towers," *Journal of Engineering Mechanics,* vol. 115, pp. 1393-1412, 1989.

[14] W. Musial and B. Ram, "Large-Scale Offshore Wind Power in the United States: Assessment of Opportunities and Barriers," NREL, Golden, CO, 2010.

Kontroll- og referanseside/
Review and reference page

Dokumentinformasjon/*Document information*		
Dokumenttittel/*Document title* Estimation of hysteretic soil damping from laboratory measurements including strain accumulation		**Dokument nr/*Document No.*** 20110087-01-R
Dokumenttype/*Type of document* ☒ **Rapport/*Report*** ☐ **Teknisk notat/*Technical Note***	**Distribusjon/*Distribution*** ☐ **Fri/*Unlimited*** ☒ **Begrenset/*Limited*** ☐ **Ingen/*None***	**Dato/*Date*** 12 May 2014 **Rev.nr./*Rev.No.*** 0
Oppdragsgiver/*Client* Norges forskningsråd.		
Emneord/*Keywords*		

Stedfesting/*Geographical information*	
Land, fylke/*Country, County*	**Havområde/*Offshore area***
Kommune/*Municipality*	**Feltnavn/*Field name***
Sted/*Location*	**Sted/*Location***
Kartblad/*Map*	**Felt, blokknr./*Field, Block No.***
UTM-koordinater/*UTM-coordinates*	

Dokumentkontroll/*Document control*

Kvalitetssikring i henhold til/*Quality assurance according to* NS-EN ISO9001

Rev./ *Rev.*	**Revisjonsgrunnlag/*Reason for revision***	**Egen-kontroll/ *Self review* av/*by:***		**Sidemanns-kontroll/ *Colleague review* av/*by:***		**Uavhengig kontroll/ *Independent review* av/*by*:**		**Tverrfaglig kontroll/ *Inter-disciplinary review* av/*by:***	
0	Original document	FLo		CM					

Dokument godkjent for utsendelse/ *Document approved for release*	**Dato/*Date***	**Sign. Prosjektleder/*Project Manager***
	12.05.2014	Finn Løvholt

NGI (Norges Geotekniske Institutt) er et internasjonalt ledende senter for forskning og rådgivning innen geofagene. Vi utvikler optimale løsninger for samfunnet, og tilbyr ekspertise om jord, berg og snø og deres påvirkning på miljøet, konstruksjoner og anlegg.

Vi arbeider i følgende markeder: olje,gass og energi, bygg, anlegg og samferdsel, naturskade og miljøteknologi. NGI er en privat stiftelse med kontor og laboratorier i Oslo, avdelingskontor i Trondheim og datterselskap i Houston, Texas, USA.

NGI ble utnevnt til "Senter for fremragende forskning" (SFF) i 2002 og leder "International Centre for Geohazards" (ICG).

www.ngi.no

NGI (Norwegian Geotechnical Institute) is a leading international centre for research and consulting in the geosciences. NGI develops optimum solutions for society, and offers expertise on the behaviour of soil, rock and snow and their interaction with the natural and built environment.

NGI works within the oil, gas and energy, building and construction, transportation, natural hazards and environment sectors. NGI is a private foundation with office and laboratory in Oslo, branch office in Trondheim and daughter company in Houston, Texas, USA.

NGI was awarded Centre of Excellence status in 2002 and leads the International Centre for Geohazards (ICG).

www.ngi.no

Hovedkontor/Main office:
PO Box 3930 Ullevål Stadion
NO-0806 Oslo
Norway

Besøksadresse/Street address:
Sognsveien 72, NO-0855 Oslo

Avd Trondheim/Trondheim office:
PO Box 1230 Pirsenteret
NO-7462 Trondheim
Norway

Besøksadresse/Street address:
Pirsenteret, Havnegata 9, NO-7010 Trondheim

T: (+47) 22 02 30 00
F: (+47) 22 23 04 48

ngi@ngi.no
www.ngi.no

Kontonr 5096 05 01281/IBAN NO26 5096 0501 281
Org. nr/Company No.: 958 254 318 MVA

BSI EN ISO 9001
Sertifisert av/Certified by BSI, Reg. No. FS 32989